Innovative Silicon Tracker Detector: CMS Outer Tracker Upgrade and MUonE Application

Matteo Magherini

10 Apr, 2024

Università degli Studi di Perugia

Dipartimento di Fisica e Geologia

Documentation

Innovative Silicon Tracker Detector: CMS Outer Tracker Upgrade and MUonE Application

Matteo Magherini

Supervisor Alessandro Rossi

10 Apr, 2024

Matteo Magherini
Innovative Silicon Tracker Detector: CMS Outer Tracker Upgrade and MUonE Application
10 Apr, 2024
Supervisor: Alessandro Rossi

Università degli Studi di Perugia
Dipartimento di Fisica e Geologia

Abstract

In the coming decades, the Large Hadron Collider (LHC) will increase its luminosity by an order of magnitude, and the experiments sitting on it will have to face challenging conditions. To cope with the great amount of collision, the Compact Muon Solenoid (CMS) experiment plans a major upgrade: one of the purposes of this upgrade is the use of tracking data for the level one trigger. To achieve this goal, the tracker will be completely renewed, using a new silicon detector read out by an all-FPGA architecture.

The new silicon modules for the CMS Outer Tracker (OT) are also planned for use in the proposal of the MUonE experiment, whose aim is to measure the elastic scattering angle between electrons and muons to measure directly the hadronic contributions to the void polarisation for muons, the greatest uncertainty related to g-2 experiment results.

This thesis presents an overview of the whole process of new silicon detector build-up, from assembly to the results of joint test beams from MUonE and CMS experiments, to prove that the final data acquisition chain for this module works.

The initial chapters, specifically Sec. 1 and Sec. 2, will outline the planned upgrades for CMS and its tracker, providing a solid theoretical background. Following this, Sec. 3 will detail the assembly process for the Outer Tracker (OT) modules, highlighting the years of meticulous development and effort that have gone into refining this procedure.

Sec. 4 will focus on the Data Acquisition (DAQ) system used for module readout. It will cover the achievements of the test system's capabilities and offer a glimpse into the expected full DAQ system for the final setup. This section aims to spotlight the differences between the test and final systems, identifying what currently exists and what needs to be adapted for the final implementation.

In Sec. 5, readers will find an essential theoretical introduction to the MUonE experiment. Then, Sec. 6 will present the outcomes from the initial MUonE test

run. This includes module characterization and the analysis of a physical process, confirming the efficiency of the entire DAQ chain.

Contents

1 CMS Phase-2 Upgrade

To achieve the desired advancements in physics measurements, the Large Hadron Collider (LHC) [1] will undergo significant improvements in the coming years. These enhancements aim to achieve an instantaneous luminosity approximately seven times higher than the current levels. In preparation for the expected increase in particle flux, with the potential of producing up to 200 concurrent events in each bunch crossing, the Compact Muon Solenoid (CMS) detector [2] will undergo significant upgrades. These upgrades are crucial for enhancing radiation tolerance and improving particle reconstruction capabilities under high luminosity conditions. A pivotal aspect of this upgrade is the integration of tracking information into the Level 1 (L1) trigger.

This chapter will detail the motivations and objectives behind the high Luminosity LHC (HL-LHC) upgrade, followed by a discussion of the CMS Phase-2 upgrade associated with the HL-LHC enhancements, outlining the anticipated changes in various detector components planned in the forthcoming years.

1.1 The High Luminosity LHC upgrade

The LHC started operations in 2009. Able to provide collision between protons, lead ions, and protons and lead ions (pp, PbPb, and pPb collisions), it's the world's largest and most powerful particle accelerator. The collision started at a center-of-mass energy ($\sqrt{s}$) of 7 TeV for pp runs during the first year and reached a peak $\sqrt{s} = 13.6$ TeV during 2022 and 2023. The collision rate for pp collisions increased steadily during the years. As it's possible to see in Fig. 1.1, starting as $2.1 \times 10^{32} cm^{-2} s^{-1}$ in 2010 and peaking at 2×10^{34} cm^{-2}s^{-1} in 2022 and 2023, exceeding the nominal design value for LHC of 1×10^{34} cm^{-2}s^{-1}. The improvement in the instant luminosity is reflected in the one of the delivered integrated luminosity to the experiment, as visible in Fig. 1.2, enabling CMS to record a total of 245 fb^{-1} since 2009 with an overall efficiency of 92.5%.

The excellent performances of LHC made it possible for the main experiments (ATLAS, ALICE, CMS, and LHCb) to achieve relevant physics results: from the discovery of the Higgs Boson in 2012 by ATLAS and CMS [4] [5], to the measurements of branching

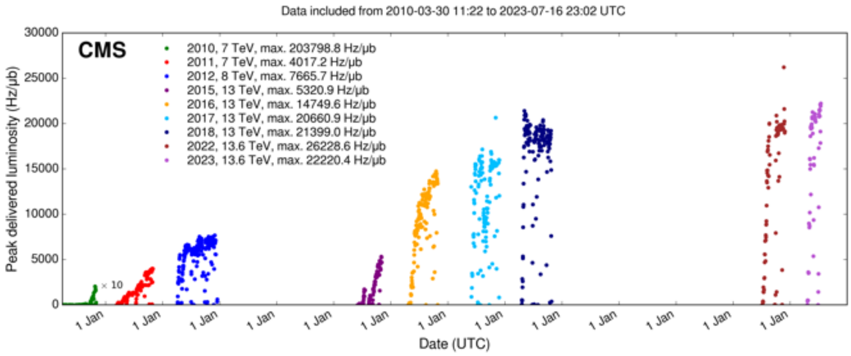

Fig. 1.1: Instant luminosity delivered by LHC as measured by CMS during the whole running period of LHC [3].

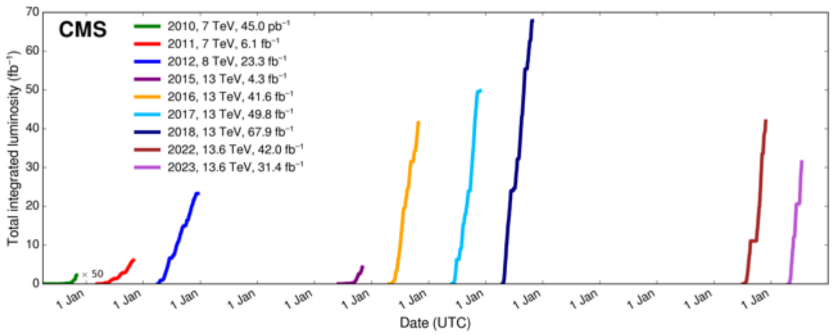

Fig. 1.2: Total integrated luminosity delivered by LHC as measured by CMS for the whole running period of LHC [3].

ratios of neutral B_S^0 and B^0 mesons to two muons by the joint effort of CMS and LHCb [6] and independently by ATLAS [7], including a variety of limits set up on several vastly different physics models.

As depicted in Fig. 1.3, the so-called Run 3 started in 2022 and is scheduled to conclude by the end of 2025. This Run is expected to collect an integrated luminosity of about 300 fb^{-1}, doubling up the combined total achieved in Run 1 and Run 2. Following Run 3, the LHC will enter its third Long Shutdown (LS) period (LS3), slated to end in 2029. This interval will see the main preparation of the experiments and the accelerator in the next phase: HL-LHC. The purpose of HL-LHC is to reach a peak luminosity of 7.5×10^{34} cm^{-2}s^{-1} in the ultimate performance scenario [8], to achieve a yearly integrated luminosity around 300 fb^{-1} and up to 3000 fb^{-1} during the whole expected project lifetime at $\sqrt{s} = 14$ TeV.

The luminosity increase will be reached through a series of different measures, mainly the use of new inner triplet quadrupole magnets based on Nb_3Sn technology. These magnets are designed to provide a higher magnetic field strength and larger

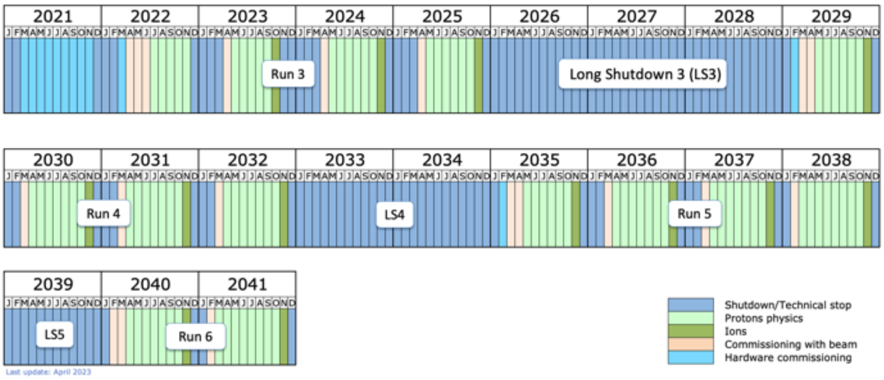

Fig. 1.3: Schedule of LHC running periods, as of April 2023. [9]

aperture, with the consequence of a lower beam beta function in the collision region. Various new corrector magnets will be installed, adding superconducting radiofrequency crab cavities in the interaction regions to allow beam rotation before interaction regions to favor head-on collision of bunches.

The increase in luminosity is needed for a variety of physics searches [10] [11] [12]. Regarding Standard Model (SM) measurements, HL-LHC will allow CMS to achieve unprecedented precision levels on many Higgs couplings. This includes the coupling to muons, which has a branching fraction of $\sim 10^{-4}$, and the Higgs self-coupling, a process with a cross-section nearly 1000 times smaller than that of single Higgs production. Vector boson scattering is another critical area of study. It is closely linked to Electroweak (EWK) symmetry breaking and presents significant measurement challenges due to large background noise. Recent years have seen successful measurements of many channels in this process [13], and the increased data from higher luminosity will be instrumental in identifying more complex final states. Also Beyond Standard Model (BSM) searches will profit the luminosity increase as rare processes will become more easily observable, with examples like $B^0_S \to \mu^+\mu^-$ expected to reach a significance of $6.8\ \sigma$.

1.2 The CMS Phase-2 Upgrade

To take advantage of the increased luminosity of HL-LHC the CMS detector will undergo significant upgrades during the LS3 to adapt to the increased luminosity and the ensuing harsher radiation conditions. This upgrade is referred to as the CMS Phase-2 Upgrade.

A key aspect of these upgrades is the enhancement of the detector's data handling capabilities, necessitated by the expected rise in data rates. A critical component in this context is the L1 trigger, which requires substantial improvements to manage these higher data rates effectively without compromising the detector's physics potential. The planned enhancements include increasing the trigger rates from 100 kHz to 750 kHz for the L1 trigger, and from 100 Hz to 7.5 kHz for the High-Level Trigger (HLT). A scheme of the actual data acquisition system, comprising L1 and HLT, is visible in Fig. 1.4. Accompanying these changes, the time available for L1 trigger computation, namely, its latency, will be increased from the current 3.2 microseconds to 12.5 microseconds. This adjustment in latency is strategically implemented to enable the integration of tracking information from the Outer Tracker (OT) into the L1 trigger process, a key advancement that will significantly improve the event selection efficiency. Detailed descriptions of the data stream, modules, and electronic systems facilitating this enhancement can be found in Sec. 4 and Sec. 2.

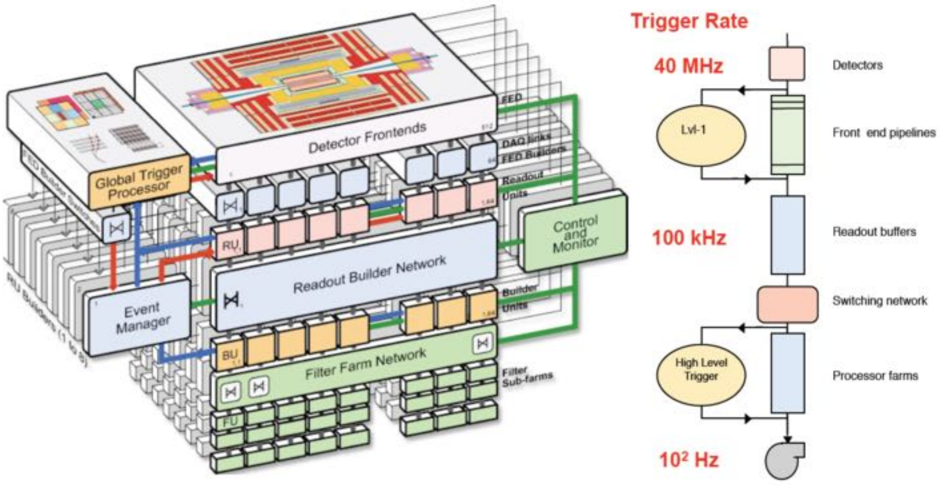

Fig. 1.4: Scheme of the present structure of the data acquisition system, L1 and HLT for the CMS experiment [14].

As part of the Phase-2 upgrade, three main systems will be upgraded in the CMS detector, the present state of which is visible in Fig. 1.5 and described in [2][15]: the muon system, the calorimeters, and the tracker.

Whilst the muon system itself is expected to cope with the increased rate, the front-end electronics for the drift tube chambers and the cathode strip chambers will need to be replaced for both performance and radiation hardness. In the forward region, new chambers based on the gas electron multiplier [16] techniques will be installed.

Regarding the Electromagnetic Calorimeter (ECAL), both the front-end and off-detector electronics in the ECAL Barrel will be improved, while the ECAL Endacp will be replaced. Avalanche Photodiodes will remain operational throughout Phase 2. However, an amplification in dark current is inevitable due to bulk silicon damage from hadron exposure. To reduce this effect by a factor ~ 2 [17], the operational temperature for ECAL Barrel will be adjusted from the Phase-1 of 18 °C down to 9 °C. The front-end upgrade will enable streaming of data at full granularity (i.e. single crystal information at 160 MHz), while the present system allows only information of 5×5 crystals groups at 40 MHz.

The Hadronic Calorimeter (HCAL), consisting of brass absorbers and plastic scintillator layers read out by hybrid photodiodes, will see the photodiodes replaced with Silicon PhotoMultiplier (SiPM) already before LS3.

A new combined detector, called High Granularity Calorimeter (HGCAL) [18], will completely replace the endcap portion of both ECAL and HCAL. The design of the new detector uses silicon sensors as active material in the front sections and plastic scintillator tiles, with the scintillation light read out by SiPMs, towards the rear. This detector will provide high transverse and longitudinal granularity, improving pile-up (PU) rejections and identifications of electrons, photons, taus, and jets.

The Phase-2 upgrade will also feature the installation of the Minimum Ionizing Particle Timing Detector (MTD) [19], which will allow for precise timing measurements of Minimum Ionizing Particle (MIP), with a resolution that starts at 30-40 ps and rises to 50-60 ps towards the end of HL-LHC operations due to radiation damage. This enhancement is critical for accurately assigning charged tracks to interaction vertices in dense collision environments. In terms of its construction, the MTD combines two technologies: crystal scintillator technology read out with MTDs in the Barrel Timing Layer, and Low Gain Avalanche Detectors in the Endcap Timing Layer.

The whole silicon tracker will be completely replaced and the next chapter is dedicated to describing such an upgrade.

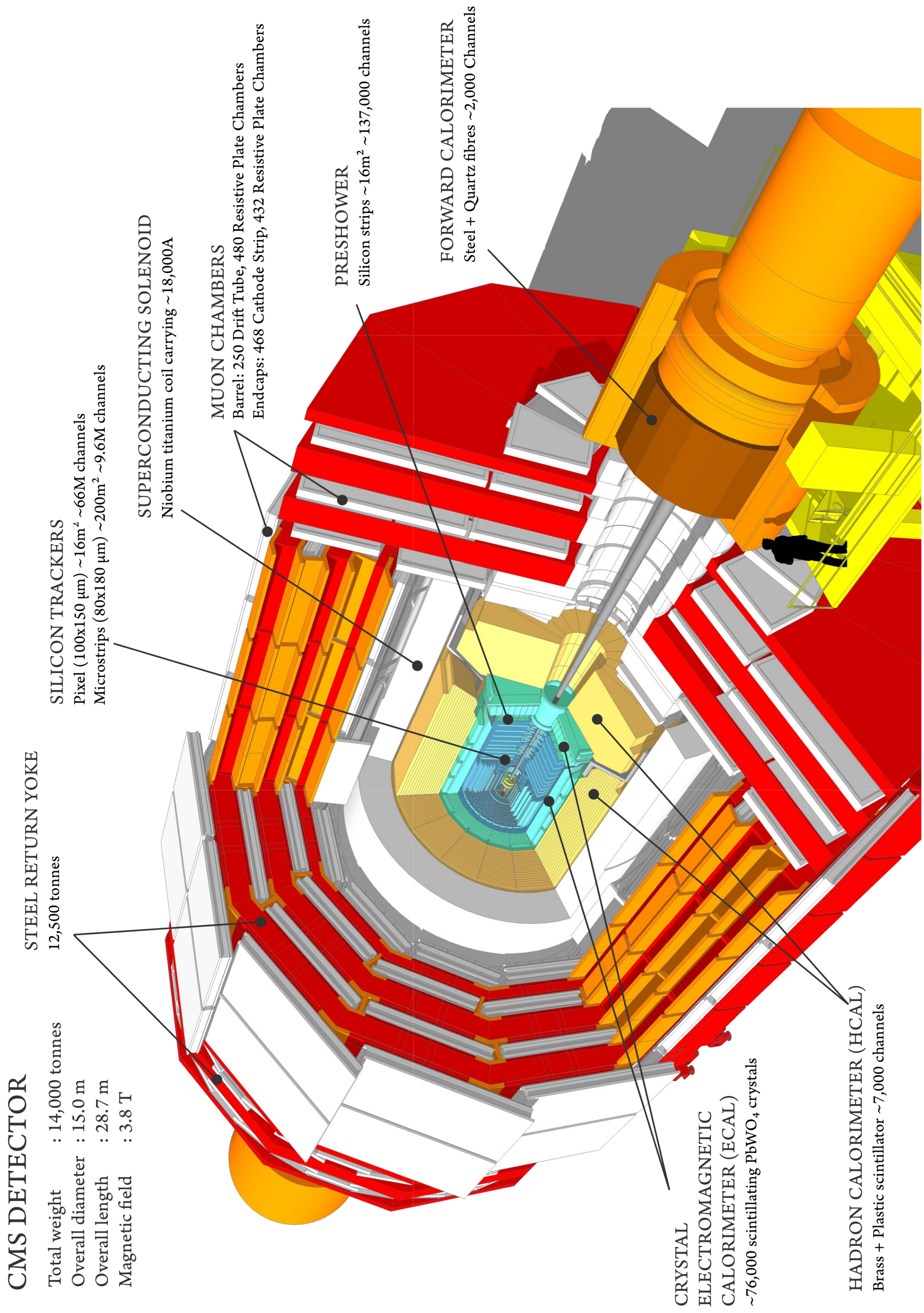

Fig. 1.5: Scheme of the present CMS detector. [20]

2 CMS Phase-2 Tracker Upgrade

The preceding chapter has laid the groundwork for understanding the heightened particle flux and data flow challenges posed by the HL-LHC. This chapter is dedicated to an in-depth discussion of the anticipated upgrades to the CMS tracker detector, crucial for addressing these challenges.

Initially, the chapter will provide an overview of the current configuration of the CMS tracker, underscoring the imperatives and objectives that drive the need for its upgrade. Subsequently, the focus will shift to a comprehensive analysis of the planned enhancements for both the Inner Tracker (IT) and the OT. Special emphasis will be placed on the technological advancements in the OT, detailing its components and functionalities. The final section will elucidate the integral role of the OT in augmenting the capabilities of the L1 trigger system, a critical aspect in coping with the expected increase in data volume and event rates.

2.1 Present tracker and upgrade perspectives

The present tracker, one quarter of which is sketched in Fig. 2.1, is divided into two sectors:

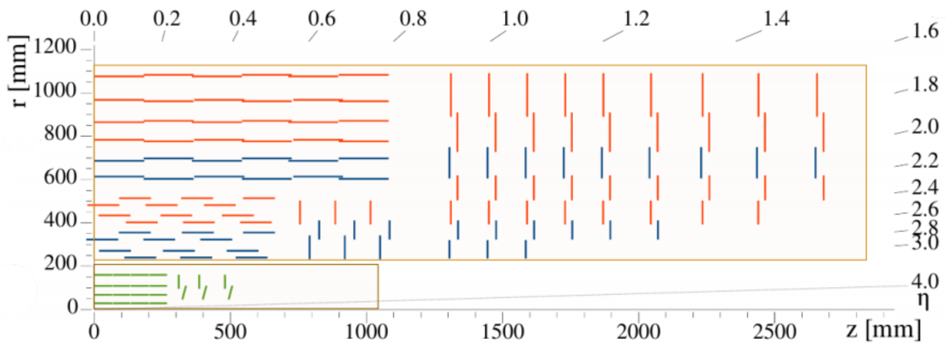

Fig. 2.1: Sketch of one-quarter of the Phase-1 CMS tracking system in r-z view. The pixel detector is shown in green, while single-sided and double-sided strip modules are depicted as red and blue segments, respectively. [21]

Inner tracker Positioned in the radial region below 200 mm from the beam, is equipped with pixel silicon detectors. Each pixel module is about 18.6$\times$66.6 mm^2, with a pixel size of 100$\times$150 μm^2 and 300 μm thickness. It's composed of four layers parallel to the beam in the barrel region, up to a pseudorapidity η (with $\eta = -ln[tan(\theta/2)]$ where θ is the polar angle) of 1.4 and two sets of three disks perpendicular to the beam in the endcap region (up to $\eta = 2.5$). This setup makes a 4-hit coverage for particles up to $\eta = 2.5$, with a resolution on the measured position of about 10 μm for the barrel and 30 μm for the endcap.

Outer tracker Positioned beyond 200 mm from the beamline, is equipped with single and double-sided silicon strip detectors read out by APV [22] chips. It's divided into 4 different regions. The innermost region, known as the Tracker Inner Barrel (TIB), comprises four cylindrical layers that extend radially up to $\eta = 1.4$. Surrounding the TIB is the Tracker Outer Barrel (TOB), which adds six more layers parallel to the beamline, also extending up to $\eta = 1.4$. As the η value increases beyond 1.4, the Tracker Inner Disk (TID) comes into play, featuring six disks arranged perpendicular to the beamline, with three disks allocated for each endcap. Beyond the TID, the tracking scope further extends with the Tracker EndCap (TEC), which includes eighteen additional disks (nine per endcap) also positioned perpendicular to the beamline. This detector achieves a resolution in the direction perpendicular to the strips between 10 μm and 50 μm.

Even though the tracker performs very well, performance will degrade due to radiation damage beyond 500 fb^{-1}. The IT detector has already been replaced during the 2016/17 technical stop with the so-called Phase-1 pixel detector [15] due to inefficiencies addressed in the readout chip at higher rates.

The performance degradation for the tracker has been extensively studied in the Technical Proposal for CMS Phase-2 upgrade [10] [23]. This analysis highlights the necessity to replace both the Phase-1 pixel and strip detectors to maintain the tracker's efficiency and accuracy. The primary concern with the pixel detectors is the reduced hit efficiency, a result of diminished charge collection efficiency caused by accumulated radiation damage. In the case of strip detectors, the major issues are the increase in sensor depletion voltage and the rise in leakage current. While lowering the operation temperature can mitigate the effects on leakage current, this approach faces limitations. Specifically, already at 1000 fb^{-1} all the double-sided strip sensors will no longer be able to function effectively at their nominal operating temperature, due to the increase of the sensor depletion voltage and of the leakage current. The latter can be mitigated, up to a certain point, by lowering the operating temperature of the cooling system, while the former cannot. This will lead to the deterioration of tracking and b tagging performance and a worsening of the impact parameter resolution.

In this framework, several requirements for the Phase-2 tracker upgrade arise:

Radiation tolerance Full efficiency must be ensured up to a luminosity of 3000 fb^{-1}. FLUKA [24] [25] simulated particle fluence in 1 MeV neutron equivalent per cm^2 ($n_{\mathrm{eq}}/\mathrm{cm}^2$) for $\sqrt{s} = 14$ TeV pp collisions are shown in Fig. 2.2 and correspond to ~ 1 order of magnitude more than the current tracker. Whereas for Phase-2 IT, the concept of accessibility is envisioned to replace modules and other pieces damaged from radiation, it's not for the OT upgrade.

Increased granularity To cope with the higher instantaneous luminosity (targeting 140-200 collisions per bunch crossing), a lower channel occupancy under percent level (per mille level) must be achieved in the OT (IT).

Improved two-track separation Highly energetic jets tracking currently has limited performance due to hits merging in the IT, so track separation must be improved to optimally exploit HL-LHC data.

Reduced material budget Calorimeters and overall event reconstruction performances in CMS are greatly affected by the amount of material (material budget from the actual tracker is visible in Fig. 2.5 on the left). A lighter tracker would be greatly beneficial for the experiment.

Robust pattern recognition Due to the hard pile-up conditions, track finding will become more difficult in HL-LHC conditions, so the new tracker design should make this easier when targeting the HLT.

Contribution to L1 trigger Due to inefficiencies of selection algorithms in high PU conditions, the selection of interesting physics events at the hardware level trigger will become much more important and CMS chose to anticipate part of the reconstruction happening in the HLT in L1, given the higher latency and bandwidth possible.

Extended tracking acceptance CMS physics program will greatly benefit from better reconstruction of tracker and calorimeters in the forward region, so the upgraded tracking system will provide efficient tracking up to $\eta = 4$.

A comprehensive sketch of the Phase-2 CMS tracker is depicted in Fig. 2.3, where different modules are distinguished by varying colors. A detailed description of each module and its specific functions will be covered in the rest of this chapter. The

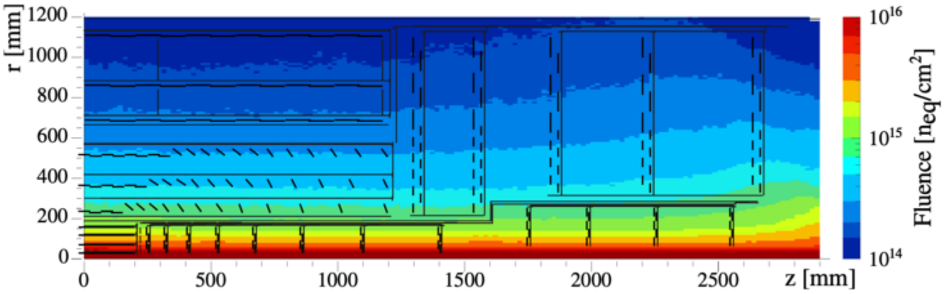

Fig. 2.2: FLUKA simulated particle fluence in 1 MeV neutron equivalent per cm^2 for $\sqrt{s} = 14$ TeV pp collisions for the Phase-2 Tracker [21].

upgraded tracker design ensures full coverage up to $\eta = 4$. In terms of tracking efficiency, Fig. 2.4 presents simulations of the average number of hits, both overall and for each layer of the tracker. These simulations consistently show an average hit count exceeding five across the entire coverage area, indicative of the tracker's robust tracking performance. Furthermore, as illustrated in Fig. 2.6, the simulated capabilities for reconstructing top-antitop quark ($t\bar{t}$) events with the Phase-2 tracker are expected to be at least on par with, if not superior to, the Phase-1 tracker. Notably, great improvements are foreseen in the impact parameter resolution and reconstruction efficiency near the jet axis.

Additionally, simulations concerning the material budget of the upgraded tracker, as shown in Fig. 2.5, reveal a substantial improvement. Despite the enhancements in performance, the design modifications will enable a reduction of nearly 50% in the amount of material positioned in front of the calorimeters.

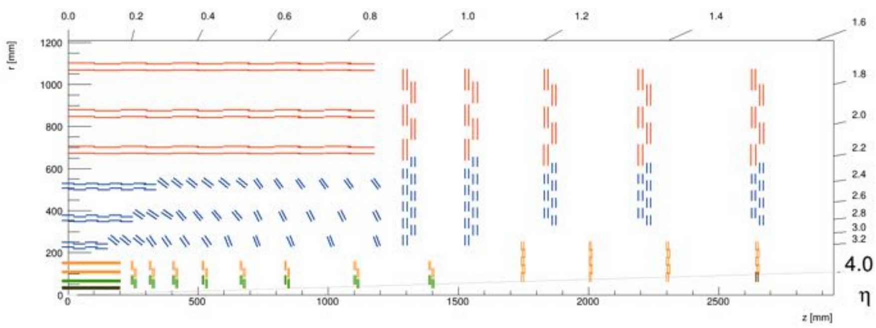

Fig. 2.3: Sketch of one-quarter of the Phase-2 CMS tracking system in r-z view. In black, the 3D pixel modules, whilst in yellow planar pixel modules are shown. In the outer section, blue (red) lines represent PS (2S) modules, as described in Sec. 2.3.1 [21].

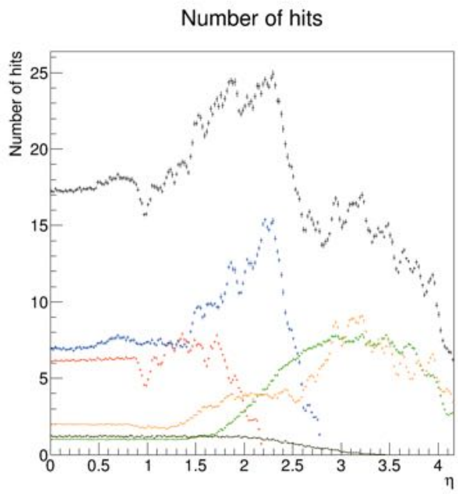

Fig. 2.4: Average number of hits for the angular coverage range of the tracker. In yellow and green are the IT modules, and in orange and blue OT modules. Black points are the sum of hits in the whole tracker. [21]

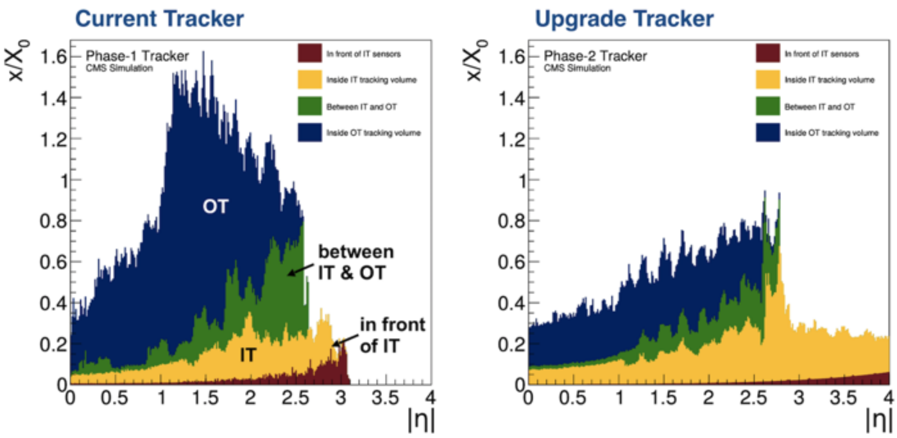

Fig. 2.5: Material budget for the tracker for Phase-1 tracker (left) vs Phase-2 (right). [21]

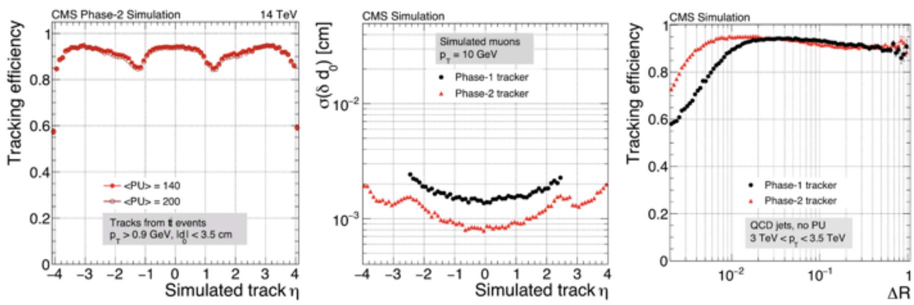

Fig. 2.6: Tracking performances of simulated $t\bar{t}$ events for Phase-1 vs Phase-2 tracker. On the left, efficiency at different η and PU is shown, in the middle the muon transverse impact parameter resolution as a variable of η, and on the right the tracking efficiency as a function of $\Delta R = \sqrt{(\Delta\eta)^2 + (\Delta\Phi)^2}$ from the jet axis [21].

2.2 Inner Tracker

As outlined in Sec. 2.1, one key aspect of the Phase-2 upgrade requirements for the CMS tracker is addressing the anticipated high hit rates, which could reach up to 3 GHz/m^2 in the innermost layer, especially considering a PU of 200. To effectively manage these high rates, the upgraded IT will be equipped with a narrower pitch compared to the current one. Two kinds of sensors will be used: either n-in-p silicon planar or 3D sensors, both with 150 μm active thickness segmented in 25×100 μm^2. This will result in a six-times reduction of the pixel area with respect to the Phase-1 tracker, providing better transverse and longitudinal impact parameter resolution, track separation, and lower occupancy. Even though 3D sensors provide better radiation hardness, their production is extremely expensive and they will be used only for the area that will withstand the most intense flux: the first layer of the tracker barrel.

Regarding the readout chips, 4 groups of 4 pixels each (referred to as a pixel region), will share digital electronics for buffering, control, and data formatting. This pixel readout chip has been developed within RD53 [26], a joint CMS and ATLAS collaboration. The CMS flavor of RD53 will be described in detail in Sec. 2.2.3.

The arrangement of the modules in Phase-2 IT is shown in Fig. 2.3. The detector will feature a barrel part with four layers, called Tracker Barrel Pixel Detector (TBPX), eight small double-disks per side, called Tracker Forward Pixel Detector (TFPX), and four large double-disks per side called Tracker Endcap Pixel Detector (TEPX). In the barrel region, modules are arranged in ladders: neighboring ladders are mounted to achieve $r - \phi$ overlap, but no overlap in z is achieved on a single ladder. The gap at $\eta = 0$ is avoided by mounting an odd number of modules and splitting the barrel mechanics into slightly asymmetric halves. Simple installation and removal are also previewed, to replace damaged parts and access the service cylinders.

2.2.1 Planar Silicon Sensor

Planar silicon sensor will be used for the whole IT, except for the first layer of the TBPX. For the target integrated luminosity of 3000 fb^{-1}, the sensors will be exposed to 2.3$\times$10^{16} n$_{\mathrm{eq}}$/cm^2. In these conditions thin sensors are preferred over thick ones: even if the latter has a larger signal at the beginning, this advantage expires when severe trapping caused by radiation damage is present at large fluence.

The layout of four adjacent pixels is shown in Fig. 2.7 on the left, where the peculiar position of the metal layers, in blue, called bitten implant, is visible. The bitten

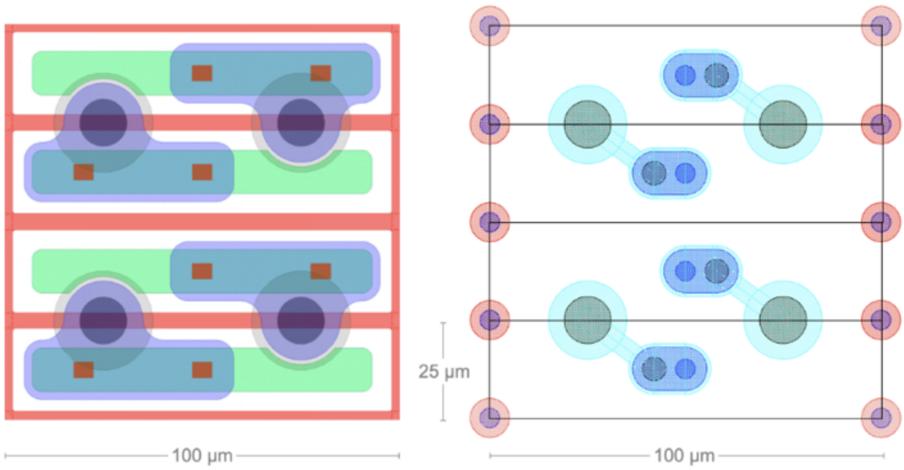

Fig. 2.7: Drawing of four adjacent pixel cells for both planar sensors (left) and 3D sensors (right). The n+ implants are shown in green, the metal layers in blue, the p-stop areas in red, the contacts in orange, and the bump bond pads in purple. [27]

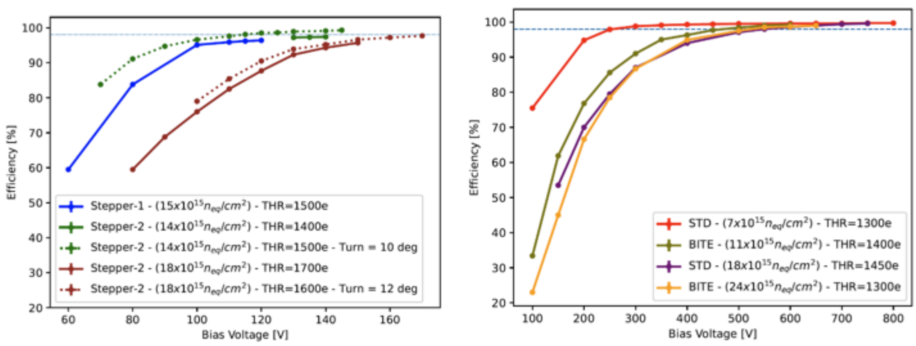

Fig. 2.8: Efficiency as a function of the bias voltage for FBK 3D sensors irradiated up to 1.8×10^{16} n_{eq}/cm^2 (left) and FBK planar sensors irradiated up to 2.4×10^{16} n_{eq}/cm^2 (right). Threshold and angular tilt are indicated too [27].

implant has been chosen due to its best performance in cross-talk reduction, proven to be below 10% on non-irradiated sensors.

As it's possible to see in Fig. 2.8 on the right, irradiation studies have been performed, proving efficiency over 99% for planar sensors up to 2.4×10^{16} MeV n_{eq}/cm^2, operating at a bias voltage of 500 V.

2.2.2 3D Silicon Sensor

In 3D sensors, electrodes are formed from narrow columns penetrating the bulk, as can be seen in Fig. 2.9. This arrangement decouples the distance between electrodes from the sensor's thickness, which reduces the aforementioned charge carrier trapping at large fluence, making this sensor less prone to thermal runaway

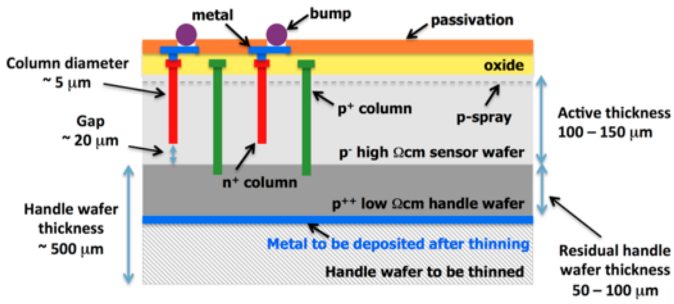

Fig. 2.9: Schematics of 3D sensors for the single-sided process used at FBK [21].

issues. In addition, a smaller depletion voltage is required compared to planar sensors to achieve efficient charge collection. Lower depletion voltage means not only lower power consumption but also reduced risk of edge sparking.

Electrodes are crafted directly on one side of the silicon wafer through Deep Reactive Ion Etching, forming both p+ and n+ type columnar electrodes. The doping process differentiates these electrodes: p+ columns are etched into a high-resistivity layer, while n+ columns maintain a critical 20 μm gap from the wafer's backside, optimizing sensor performance and production yield. After proper performance tests over different production batches with different geometries, a design that incorporates cells with four p+ corner columns and a central n+ read-out electrode. Fig. 2.7 on the right displays this four-cell structure, highlighting a 3D cell with its central n+ electrode linked to a bump pad.

Studies on sensor irradiation have been performed and results are displayed in Fig. 2.8 on the left. Efficiency over 99% has been proven up to 1.8×10^{16} n$_{eq}$/cm^2, with a bias voltage of 140 V.

2.2.3 Readout chip (CROC)

The Read Out Chip (ROC) used for the inner tracker, as previously stated, has been developed through a joint collaboration with ATLAS under the RD53 collaboration [26]. Achieved through the Complementary Metal-Oxide Semiconductor (CMOS) 65 nm technology, the chip will need to withstand 1.2 Grad of total ionizing dose and a maximum hit rate of 3.2 GHz/cm^2 and need strong protection against Single Event Upset (SEU) effects. The chip guarantees also a low power consumption (less than 1 W/cm^2 at CMS trigger level readout of 750 kHz) and serial powering through on-chip shunt-Low-Dropout (shunt-LDO) regulators. The chip provides analog readout with Time-Over-Threshold (ToT).

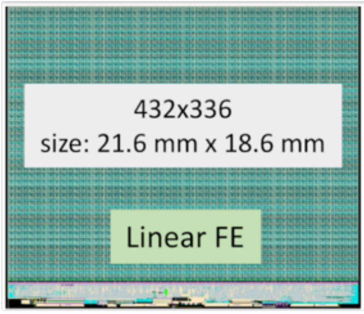

Fig. 2.10: Multi cell schematics of a CROC (left) picture of a CROC and readout structure (right).

The RD53A was the first R&D purpose prototype common for ATLAS and CMS, it featured three analog Front End (FE): synchronous, linear, and differential, with 76800-pixel channels, arranged in 192 rows and 400 columns.

The CMS flavour of RD53 (CROC) measures 16.8×21.6 mm^2, corresponding to 432 rows times 336 columns of 50×50 μm^2 elementary cell for an analog FE linear architecture, as visible in Fig. 2.10 on the left. Multiple test beams have been performed using CROC, both at DESY and CERN SPS test beam (TB) areas, using EUDET-like telescopes [28] with irradiated chips. Preliminary results show a hit efficiency $\geq 96\%$ for irradiated 3D pixel modules with CROC [29], and $\geq 98\%$ for planar sensors after irradiation, at $V_{bias} \simeq 800$ V [30].

2.2.4 Pixel Module

The sensor, with readout chips, a flex circuit, and mechanical support, will be assembled in a structure called a module. A typical IT module scheme is shown in Fig. 2.11. It features the sensor bump-bonded to the CROC, a High-Density Connector to distribute signals and powering, and, only in the TBPX, an Aluminium Nitride cooling plate, which ensures mechanical stability and heat removal. Modules will come in two flavors, as it's possible to see in the middle and right of Fig. 2.12. The two different configurations, called 2×1 and 2×2, are defined by the number of ROC bonded to the sensor. To overcome yield issues in fabrication, TBPX 2×1 modules that will carry a 3D sensor won't feature one, big sensor, but two smaller ones placed close together.

Modules with planar sensors require a protective treatment to endure High Voltage (HV) bias, reaching up to 800 V after irradiation: the tested solution is a protective 18 μm thick layer of Parylene-N, showing resilience up to 1 kV. During the production phase, the coating process will be applied to fully assembled multi-chip modules.

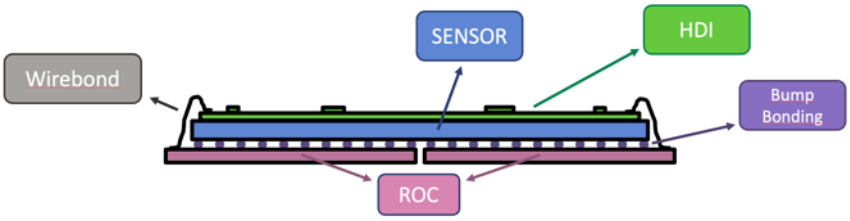

Fig. 2.11: Scheme of an IT module.

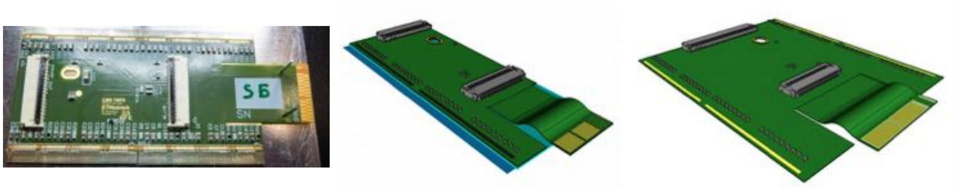

Fig. 2.12: On the left, an inner tracker 1x2 module, on the center and the right, respectively, the drawings for 1x2 and 2x2 IT modules.

This procedure necessitates special masking for connectors and pigtails to prevent coating deposition in areas where it could impede functionality. Additionally, careful masking of the module's backside is essential, especially when thermal efficiency is a critical factor for the module's performance. This step ensures that the coating does not adversely affect heat dissipation capabilities.

Different methods have been developed to assemble modules, achieving a precision between 10 to 20 μm. For TBPX modules, manual assembly is the chosen method. This process involves using jigs and templates. Mechanical stops, such as pins, ensure precise component placement, while vacuum fixation provides stability during positioning and adhesive curing. Stencils ensure even glue distribution. Efficiency is increased by assembling multiple modules at the same time. In the case of TFPX modules, the approach is slightly different. Jigs and templates are still used. However, components are positioned using a gantry system, adjusting according to reference markers. Like with TBPX modules, stencils aid in glue distribution. The process is made more efficient by assembling several modules in parallel. TEPX modules follow a more automated assembly process. A multi-tool robotic arm is used for assembly. It places parts from trays onto the assembly area and applies glue using a special stamp tool. This method enables batch assembly, handling six to twenty-four modules at a time.

2.2.5 Read out architecture, powering and mechanical structure

The readout and control system for the IT is centered around the Low Power Gigabit Transceiver (lpGbt) [31], embedding up- and down-link communications with the detector. This system utilizes custom electrical links to connect each pixel module to a 'portcard'. A portcard is an opto-converter module containing three lpGbts and VTRx+ (Versatile TRansceiver plus) [32] links, powered through cascaded DC-DC converters. These portcards, totaling 680 in number, are positioned on the service cylinder of the IT, an area with manageable radiation levels for the electronic components.

The up-links in this system are responsible for transmitting data and monitoring information from the modules to the counting room electronics. Each pixel module can have up to six electrical up-links, operating at 1.28 Gb/s, with a specific number depending on its location and local hit rate. This arrangement includes a 25% bandwidth headroom for electrical link occupancy. Conversely, the down-links manage the distribution of the clock, trigger, commands, and configuration data to the modules, with one electrical down-link at 160 Mb/s allocated per module.

Efforts are underway to optimize electrical link implementation concerning data rates, reliability, and material usage. Furthermore, efficient data formatting techniques are being explored to potentially halve the data rate, thus reducing the number of lpGbts required. The IT's back end will be composed of 28 Data, Trigger, and Control (DTC) boards, which will be described in Sec. 4.2.1. These will be integrated with the luminosity processors for real-time luminosity measurements and the central CMS data acquisition system. This comprehensive system is illustrated in the diagram in Fig. 2.13.

The integration of serial powering in the IT is a crucial advancement to meet the HL-LHC's stringent physics demands, offering a practical solution for supplying the necessary 50 kW of power. A scheme of the powering is visible in Fig. 2.14. This approach is unique in its minimization of material within the system, which is vital to maintain optimal tracking performance. Modules are organized into 576 serial power chains, with each chain accommodating up to twelve modules. In this configuration, modules are powered in series, while the chips within each module are powered in parallel.

A notable feature of this system is the shunt-LDO present on each chip, which ensures voltage regulation for individual chips while maintaining a consistent current throughout the system. This arrangement allows for parallel operation of chips within a module, with current capacities varying based on module size (4 A for 1x2 modules and 8 A for 2x2 modules). The sensor bias follows the serial power chains, using a single return line.

Despite its efficiency in power distribution and reduced material usage, serial powering presents challenges. It's an inherently inefficient system, necessitating additional voltage and current to ensure the proper functioning of the LDO and shunt. Each module requires an individual ground, leading to the need for AC-coupled I/O and complex bias distribution to sensors. Moreover, this method introduces new potential failure modes. However, extensive system-level testing has proven the viability of this approach. In the CMS, primary failure mitigation is facilitated by the capability for full access to the IT for maintenance.

The power system is further streamlined by the use of a single power supply module that incorporates a current source for serial powering, high voltage provision for the sensor (ranging from 0 to 800 V), and low voltage for portcards. This module also includes pre-heaters necessary for CO_2 cooling, demonstrating a comprehensive approach to power management in IT.

The redesigned structures in the detector employ lightweight carbon fiber materials, which are uniquely integrated with cooling pipes. These structures feature disks with a flat geometry, a departure from the turbine-like design found in the current detector. This update is complemented by an enhanced fiber routing system, effectively reducing radiation-induced attenuation.

The cooling mechanism is based on an evaporative CO_2 system, operating at a temperature of -35 °C. This system is efficiently distributed through stainless steel pipes, each having an outer diameter of 1.8 mm. In total, the system comprises 168 cooling loops, ensuring optimal temperature regulation and stability across the detector's structure. This innovative approach enhances the detector's performance and contributes to its overall durability and reliability.

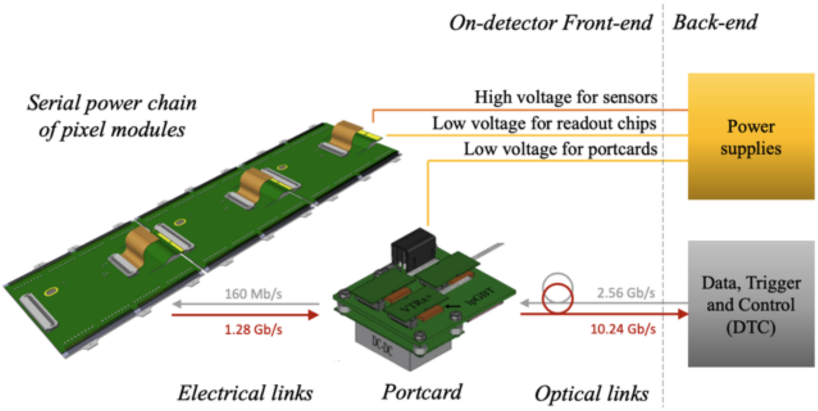

Fig. 2.13: Scheme of the data flow from modules to DTC board.

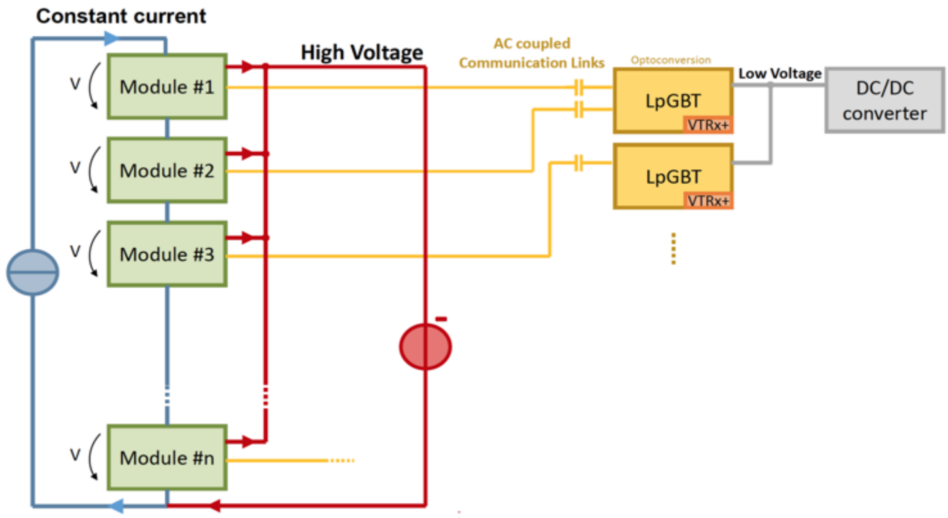

Fig. 2.14: Powering scheme for the modules.

2.3 Outer Tracker

The OT design for the Phase-2 upgrade takes into account its involvement in the L1 trigger due to online track reconstruction, which will be described in Sec. 2.4.

A layout of the upgraded OT is visible in Fig. 2.15. In the upgraded OT, the so-called p_T modules, and will be described deeply in 2.3.1 and are divided into 2S modules and PS modules, described respectively in Sec. 2.3.3 and Sec. 2.3.2.

Module installations span from a radius of approximately 210 mm to 1120 mm. Extending along the z-axis up to 1200 mm, two sets of three cylindrical layers, the innermost one equipped with PS modules and the outer one with 2S modules, form respectively the Tracker Barrel PS (TBPS) and Tracker Barrel 2S (TB2S).

Complementing these are five endcap double-disks on each side, covering the 1200 mm to 2700 mm z-axis region, forming the so-called Tracker Endcap Double Discs (TEDD).

A key design aspect of the OT is ensuring hermeticity for particles from the luminous region ($|z| < 70$ mm), guaranteeing intersection by at least six module layers for particles within the rapidity range $|\eta| < 2.4$. Extensive studies reveal that a five-layer configuration would significantly impair track finding for the L1 trigger, especially when detector inefficiencies arise. In contrast, a six-layer structure maintains robust performance despite potential inefficiencies in one layer.

In the TB2S, modules are mounted on ladder structures, with consecutive modules placed on alternate sides of the ladder's central plane, ensuring z-axis overlap (Fig. 2.16 left). The ladders are staggered in the radial direction to create a hermetic barrel layer at varying radii. The TBPS modules, in the central section, are mounted on planks (Fig. 2.16 center), achieving z-overlap with radial staggering and complemented by rings at larger $|z|$ values for tilt angle optimization (Fig. 2.16 right).

The TEDD double-disks use 2S modules in the outer part ($r > 60$ cm) and PS modules in the inner part ($r < 60$ cm). Modules are mounted on different surfaces of the dees to form hermetic layers, with consecutive rings along the radius mounted on separate disks for radial overlap.

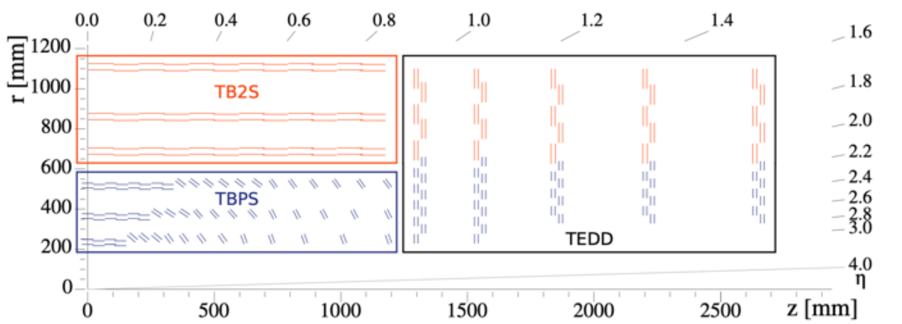

Fig. 2.15: Sketch of one-quarter of the OT in r-z view. Blue (red) lines represent PS (2S) modules. The three sub-detectors, named TBPS, TB2S, and TEDD, are indicated.

2.3.1 p_T modules

The p_T modules, including both 2S (Strip-Strip) and PS (Pixel-Strip) configurations, embody a novel approach to particle tracking and transverse momentum (p_T) reconstruction. Central to their design is the dual-sensor setup connected through a flex hybrid to a single Application-Specific Integrated Circuit (ASIC). This configuration is instrumental in measuring the p_T of particles. As a charged particle traverses a p_T

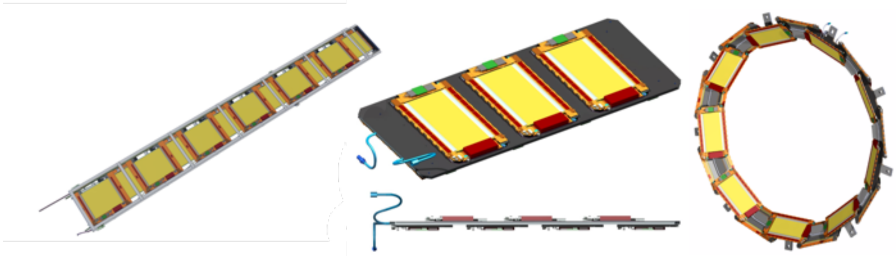

Fig. 2.16: Left: model of a TB2S ladder, housing twelve 2S modules. Center and right: Drawings of the TBPS support structures. In the central section, modules are mounted on either side of a flat support structure (center), referred to as plank, while the tilted section is composed of rings (right).

module, it interacts sequentially with both sensors, leaving electronic signatures in each. The single ASIC reads out these signals, ensuring synchronized data processing and allowing for the correlation of spatial information from both sensors. By analyzing the displacement between the paired hits in the two sensors and considering the module's geometry, the ASIC calculates the particle's path curvature through the magnetic field within the CMS detector, as it's possible to see in the schematic in Fig. 2.17. The curvature of this path is inversely related to the particle's transverse momentum: higher p_T results in less bending, whereas lower p_T leads to more pronounced curvature.

The ensemble of the position in one of the sensors and the displacement in the second one is called a stub. A stub is reconstructed when the hit in the correlation sensor is in a tunable window (in green in Fig. 2.17). A tunable correlation window is needed to accommodate different p_T selections across the whole OT, given the different spacing in sensors and the different tilting (as visible in Fig. 2.15). Selection for particles with transverse momentum $\geq$3 GeV has been proven to have a 99% efficiency [21].

Data from p_T modules feature two distinct readout paths, depicted in Fig. 2.18: the trigger path and the L1 path. The trigger path, read out at 40 MHz, will be used for the hardware tracking reconstruction in the CMS OT upgrade for the L1 trigger and consists of stub information, in which tracks are ordered by decreasing p_T. In parallel, the L1 path is activated by an L1 trigger and retrieves information from a buffer memory. This path provides comprehensive data on all the strips and pixels within a module, offering a complete picture of particle interactions. Hits from low transverse momentum, not present in the trigger path, are then retrieved this way.

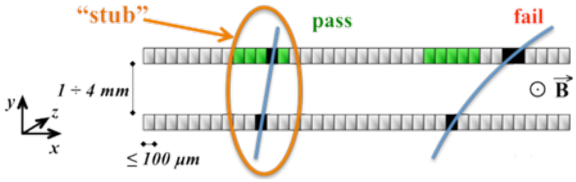

Fig. 2.17: Scheme of the working principle of p_T modules: knowing the distance between the two silicon sensors paired in a module and the tunable window (in green) it's possible to select interesting high p_T particles quickly [21].

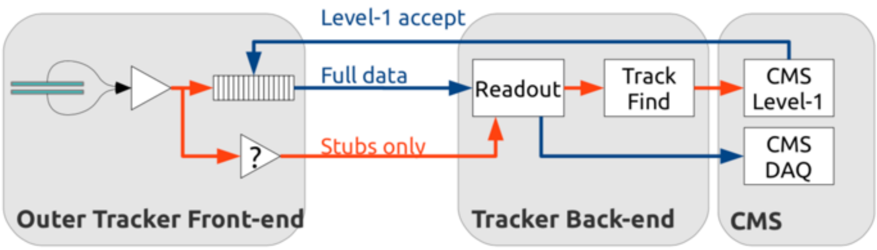

Fig. 2.18: Scheme of the readout of p_T modules: the two paths, the L1 path, and the trigger path, are shown respectively in blue and orange.

2.3.2 2S Modules

Each 2S module is equipped with two identical strip sensors, which are AC-coupled and feature each strip segmented into approximately 5 cm lengths. The sensors have a strip pitch of 90 μm, and on each side of the 10×10 cm^2 sensor, there are 1016 strips. Strips on each side are divided into 8 columns and one CMS Binary Chip (CBC) reads out corresponding columns in each sensor. To fully instrument a module, 8 CBCs per side are placed, culminating in a total of 2032 channels per side. The CBCs are responsible for detecting signals from strips from the two different sensors and creating stubs. The data from all eight CBCs on each side is then processed and compressed by one Concentrator Integrated Circuit (CIC) [33] chip per side of the module. The CIC chips are integral to the system as they handle the complex task of data compression, making the data more manageable for transmission. After the data compression, the processed information is routed through lpGbts, reaching the VTRx+ on the module, which is the last stage in the readout chain. The VTRx+ is responsible for further transmitting the data to the back-end electronics of the CMS detector. An in-depth description of the CBC chip and its working principle will be the topic of the next section (2.3.2.1). Given that the CIC is a common chip between 2S and PS, taking as input data from both types of chips, it'll be described with PS module chips (MPA and SSA), in Sec. 2.3.3.3.

A bias ring surrounds the active area of the n-on-p sensor, ensuring the distribution of the ground potential to each strip via polysilicon resistors. The sensors are designed to maintain high voltage stability up to 800 V, achieved using a single floating guard ring. Additionally, a highly doped p+ implant at the periphery of the sensor defines the depletion volume, offering protection against damage from wafer dicing. The sensor's periphery is also inscribed with alignment marks, strip numbering, and labels in the metal layer, further enhancing its structural integrity and facilitating alignment and identification processes.

Each sensor within the 2S module is assigned a unique identification tag, encoded in scratch pads or laser fuses, ensuring precise tracking and management of individual components. With a physical thickness of 320 μm, these sensors offer a balance between signal sufficiency for the detector's lifetime and reduced material introduction, leading to lower bias currents compared to sensors with larger active thicknesses. The base material's resistivity is targeted to be higher than 3 kΩcm, ensuring that the initial full depletion voltage remains below 300 V.

2.3.2.1 CMS Binary Chip

The CBC chip [34], designed for the CMS detector, operates using advanced technology in 130 nm CMOS. This chip is tasked with reading the charge generated by ionizing events in the silicon strips of the CMS detector and translating these events into binary 'hit' or 'no-hit' values for each channel. The chip can store data from each event for up to 512 bunch crossing intervals, equivalent to a trigger latency of 12.8 μs at a clock rate of 25 ns, allowing the external system sufficient time to decide which event data should be read out.

A scheme of the top-level architecture of the chip is visible in Fig. 2.19. The chip has two distinct clock domains. The first is a 320 MHz clock domain, in green in Fig. 2.19, used for all Input/Output interface activity, except for the 1 MHz I2C-type slow-control interface, which initializes register settings for comparator thresholds, amplifier biasing, and other functions. The second domain, in red in Fig. 2.19, is derived from the Fast Control Interface (FCI) in the 320MHz domain and operates at 40 MHz matching the 25 ns repetition rate of the Bunch Crossing (Bx).

Timing adjustments relative to the Bunch Crossings are facilitated by a Delay Locked Loop (DLL), which receives the 40 MHz clock from the FCI. The DLL produces multiple phase-shifted versions of the original clock, allowing users to select the appropriate version for use in various circuits, thereby tuning their phase relationship to the Bx timing. Selection of the clock phase from the DLL is controlled by an I2C programmable register, with a delay from 0 to 25 ns, in 1 ns increments. The ASIC also provides a 40 MHz clock output, mainly for testing purposes.

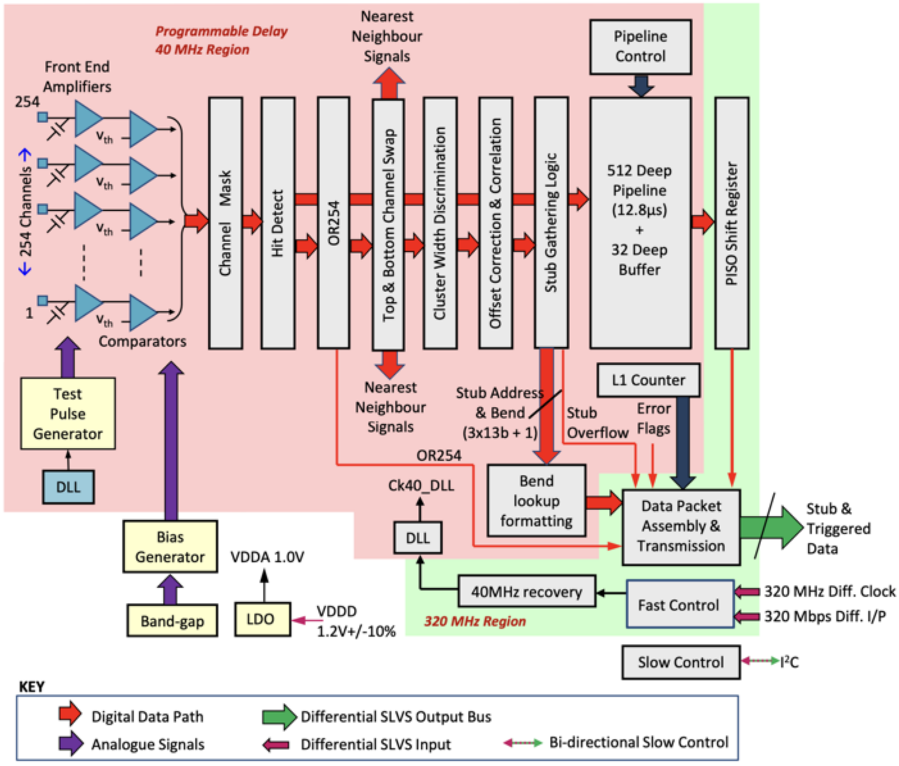

Fig. 2.19: Block diagram of CBC chip [34].

The CBC features 254 channels of analog front-end, a scheme of which is available in Fig 2.20, consisting mainly of a pre-amplifier and a post-amplifier, plus a comparator, as part of the digital front end, converting the charge deposited in the silicon sensors to binary hit data. The CBC is designed to operate with odd and even channels connected to different sensor layers of the module, allowing one CBC ASIC to service 127 strips from each of the two sensor layers. The analog front-end amplifiers can be stimulated using an on-chip test pulse generator, instigated by a fast command via the FCI. The phase relationship of the test pulse to the delayed 40 MHz clock is controlled by another DLL circuit, with a programmable 1 ns resolution available.

The analog front-end circuits are powered by an on-chip LDO, supplied by a 1.2 V (nominal) power source also used for the digital sections of the ASIC. Various analog biases used by the front-end circuits are derived on-chip using bias generation circuits referenced by a Voltage Reference Bandgap. These bias circuits have default settings on start-up but can be re-programmed via the I2C interface.

Different readout modes for hit detection are available providing four different outputs, with an example case shown in Fig. 2.21, each of which with its distinct characteristic:

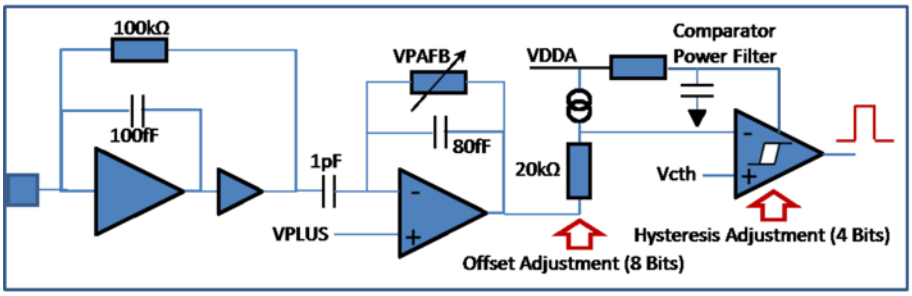

Fig. 2.20: CBC3.1 analog front end description [34].

Fixed Pulse Width The signal from the Hit comparator is held constant for the duration of a 25 ns clock cycle. This method captures transitions of the comparator output that are not synchronized with the clock. The result is a consistent 25 ns pulse, irrespective of the original pulse width from the comparator. If hits occur in consecutive clock cycles, they will be recorded as long as the channel drops below the comparator threshold after each hit;

40 MHz Sampled Output The comparator's output is monitored using a 40 MHz clock. This setup records the comparator's output only when it aligns with the rising edge of the clock. The output resets to zero on the next rising clock edge after the comparator resets. The output pulse has a minimum duration of one clock cycle. Hits that occur back-to-back in successive clock cycles are registered, even if the channel does not drop below the comparator threshold between hits;

Logical OR Output The outputs from the first and second methods are merged through a logical OR operation, yielding a composite output;

HIP Suppressed Output Tied to the second method, a HIP suppression mechanism is included. It evaluates the length of the pulse, and if it surpasses a predetermined number of clock cycles, the output is automatically reset to zero. This duration threshold is set by configuring 3 bits in a register via the I2C interface. This suppression function can be applied to either the 40 MHz Sampled Output or the Combined Logical Output, depending on the chosen setting of the multiplexer.

After the Hit Detect stage, the process is divided in two, as visible in Fig. 2.19. One route directly conveys the raw hit data to the 512-depth pipeline memory, whereas the other route processes the hit data in search of stubs. The hit data's, as visible in Fig. 2.22, entry into the pipeline is managed by a Write Pointer, which operates on a delayed 40 MHz clock and continuously cycles unless it is reset. A Read (Trigger in the figure) Pointer, which waits for a predefined latency period after the Write

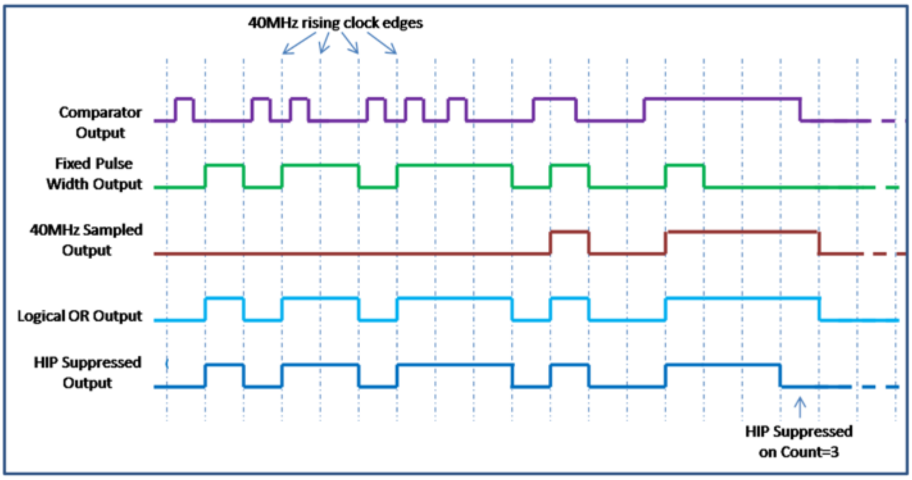

Fig. 2.21: Examples of hit detect processing for different input signal scenarios [34].

Counter before it starts to have the right association with L1 Trigger and the relative data. When an L1 Trigger signal is received through the FCI, the Read Pointer retrieves the Hit data from the relevant pipeline location and transfers it to the Output FIFO, which has a capacity for 32 events. From there, the data is sent off-chip at a speed of 320 MHz.

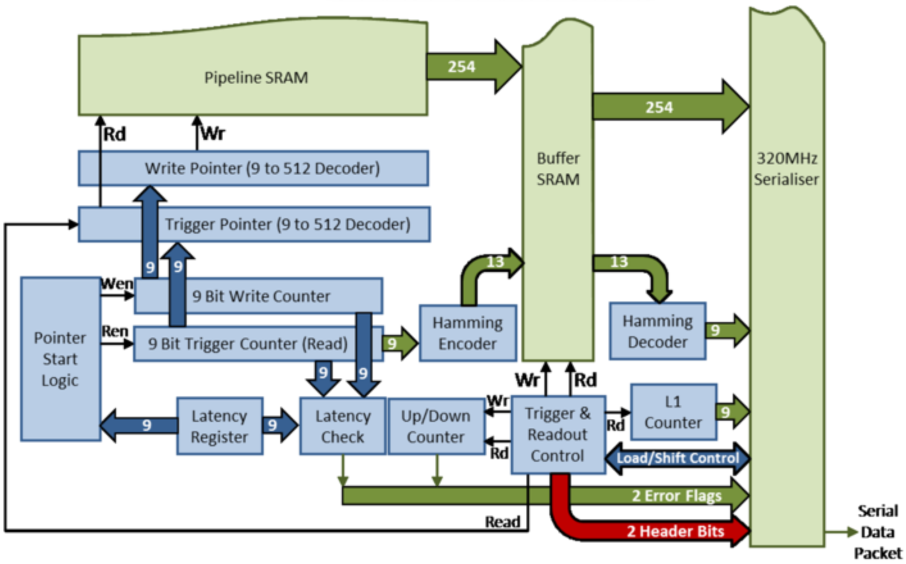

Fig. 2.22: Block diagram of the Pipeline Control Logic [34].

Simultaneously, the Stub Finding Logic (SFL) processes the hit data asynchronously, looking for coincidences of hits on channels connected to different sensor layers. The output from the SFL is latched using the delayed 40 MHz clock and then multiplexed by the Stub Gathering Logic to the Stub Data Assembly Logic, arranging it into the packet structure for output on dedicated SLVS outputs operating at 320 Mbps. The SFL also generates Bend data related to the angle of the Stub, initially at 5-bit resolution but converted to 4 bits via a programmable Look Up Table (LUT) before being assembled into the Stub data packet.

2.3.3 PS Modules

The Pixel Strip (PS) modules are made of a coupled strip and macro pixel sensor, and their assembly will be fully described in Sec. 3.2. The strip sensor of a PS module has an area of approximately $5 \times 10\ cm^2$ and is divided into two rows, each containing 960 strips. These strips are about 2.5 cm long with a pitch of 100 μm. The readout of each half of the strip sensor is managed by eight SSA.

Similarly, the pixel sensor in the PS module covers the same surface area as the strip sensor. However, it is divided into 960×32 macro pixels, each measuring approximately 100 μm $\times$ 1.5 mm. The pixel sensor is interfaced with 8×2 MPAs, which are bump-bonded to it. Each SSA is paired with an MPA responsible for reading the corresponding pixel channels.

The data handling within the PS module is quite complex. The SSA continuously transmits data about strip clusters using eight lines to the MPA. The MPA then correlates this information with pixel hits to reconstruct stubs, which are then sent to the CIC using five lines at a frequency of 320 MHz. Triggered data, meanwhile, are stored in the SSA and MPA until a trigger signal is received, at which point the SSA hits are relayed to the MPA. The MPA processes both strip and pixel hits, performing clusterization and zero suppression, and then transmits the consolidated data to the CIC via a single line at 320 MHz.

In the next paragraphs, SSAs, MPAs, and CICs will be described.

2.3.3.1 SSA

The SSA [35] is designed specifically for reading out signals from strip sensors. Its architecture encompasses both analog and digital circuits, facilitating efficient data processing and transmission.

At the forefront of the SSA is an analog front-end circuit, which utilizes a double-threshold binary system to interpret signals from the silicon strip sensor. This system includes a detection threshold set at approximately one-quarter of a MIP energy and a HIP threshold at about 1.5 MIP. This dual-threshold approach enables the SSA to differentiate between standard particle hits and those from high ionizing particles.

Following the analog stage, the digital back-end circuit of the SSA takes over. This section is tasked with generating two types of data streams: the trigger data and the L1 data streams. The trigger path involves a strip clustering logic that calculates centroid positions of hit clusters while filtering out wide cluster hits. This path also includes strip position encoding and an offset correction logic to compensate for parallax errors due to the planar nature of the sensors. The trigger data is then sent to the MPA paired with the SSA through eight differential links operating at 320 Mbps.

Concurrently, the L1 path in the SSA is responsible for storing strip hits in Static RAM (SRAM) until an L1 trigger signal is received. In this path, strip hits are stored uncompressed, while HIP threshold data are managed with a zero-suppression technique, limiting their number to 24 HIPs per bunch crossing. The L1 data is transmitted to the MPA via a single differential link, also operating at 320 Mbps. A block diagram of the SSA data paths is shown on the left side in Fig. 2.23.

The total bandwidth between the SSA and MPA, facilitated by these high-speed links, reaches 2.88 Gbps. This ensures a rapid and efficient relay of particle hit information for further processing.

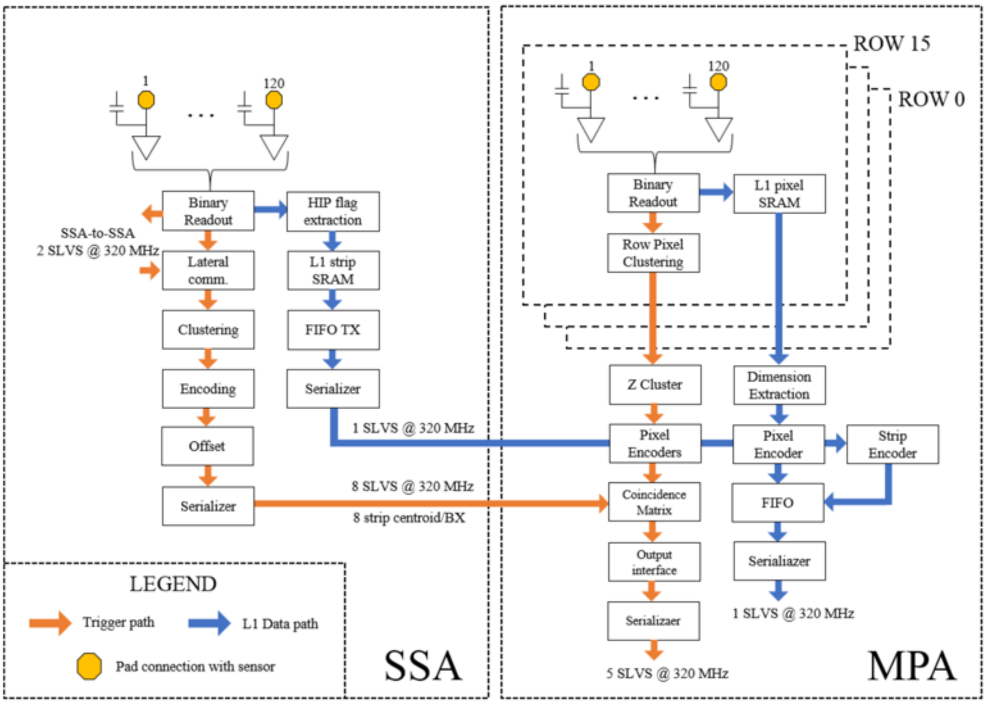

Fig. 2.23: Block diagram of SSA chips (left) and MPA chip (right) [36].

2.3.3.2 MPA

The MPA is responsible for reading out macro-pixel sensors and matching those data to the ones obtained from the SSA to create stubs. The MPA operates using a single threshold binary system, set at about a quarter of a MIP. It stores binary macro-pixel data in SRAMs until an L1 trigger is received. Upon receiving this trigger, events are processed by the L1 data logic, which also handles strip data. Both macro-pixel and strip data undergo a similar processing routine: cluster information is extracted and encoded with the position of the first pixel/strip in the cluster and its width. A HIP flag is added to strip cluster data.

In the trigger path, large macro-pixel clusters are discarded, similar to the procedure in the SSA. The remaining hits are encoded, and the logic combines these with strip clusters. Only macro-pixel and strip cluster pairs with a position difference below a configurable threshold (between 200 μm and 400 μm) are selected. This selection depends on the desired p_T threshold and the module's position in the tracker. The selected pairs, known as stubs, contain the position of the macro-pixel clusters and the position difference between the strip and macro-pixel, referred to as the bend. The stubs are then grouped over two bunch crossings and transmitted to the CIC using five differential links operating at 320 Mb/s, resulting in a total bandwidth of 1.92 Gb/s per MPA. A block diagram of the MPA data paths is shown on the right side in Fig. 2.23.

The physical design of the MPA is tailored to meet the requirements of sensor granularity and module assembly. The MPA is divided into a pixel array and periphery, with the pixel array containing 16 rows and 118 columns per MPA, given a pixel size of $100 \times 1467\ \mu\text{m}^2$.

The total chip size is 11.9×25 mm^2, including a periphery of about 2 mm, and the ASIC thickness is approximately 250 μm. The spacing between MPAs is set at a minimum of 100 μm to facilitate multi-chip module assembly. To ensure no loss of active area, unconnected sensor macro-pixels at the edges of each macro-pixel row are shorted to their neighbor, resulting in macro-pixels with double width at these edges.

2.3.3.3 CIC

The CIC serves to integrate and manage inputs from FE chips. The CIC's architecture, a scheme of which is visible in Fig. 2.24, is divided into FE blocks and an output block, each serving specific functions in data handling.

Data from each FE chip travels to the CIC via six differential lines operating at 320 MHz, split between L1 and trigger data lines. In the case of MPA chips, due to the expected higher occupancy in PS modules, trigger data is sent in synchronous frames extending over two clock cycles, effectively averaging the stub rates for efficient processing.

Each FE block in the CIC corresponds to a single FE chip, with eight such blocks present. These blocks process trigger and L1 information, treating them distinctly. For the trigger information, the processing is uniform across FE chip types, whether they are CBC or MPA. However, for L1 data, the CIC adapts its approach based on the chip type: CBC data enter unsparsified and are processed within the block for necessary compression, while MPA L1 data, already sparsified, bypasses this process. Additionally, there's a CBC deserialized mode for debugging, allowing raw CBC data transmission at a limited rate.

The CIC's output block plays a crucial role in data integration. It consolidates data retrieved from all FE blocks by deserializing the 48 input lines and re-serializing it in the 6 output lines, formats it into an output data packet, and undertakes stub selection within the trigger path. Finally, the data transmission from the CIC to the lpGbt is executed through seven lines running at the same frequency. The trigger data, stored and sorted over eight bunch crossings based on their bend information, are transmitted in an 8-clock cycle synchronous block. This method minimizes data loss and maintains the required synchronicity for the concentrator's output.

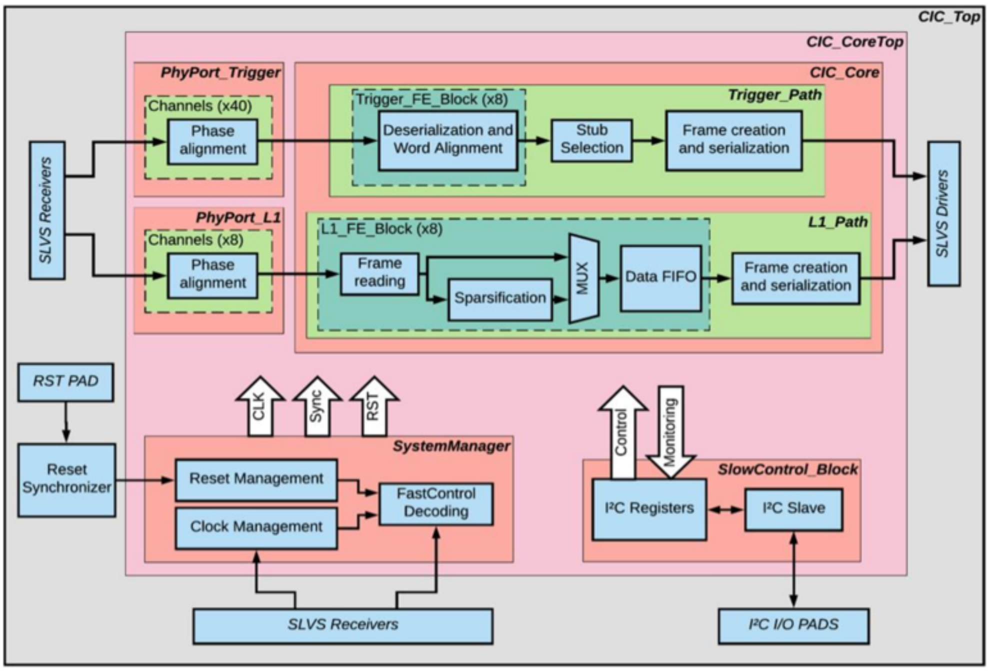

Fig. 2.24: Block diagram of CIC chip.

2.4 Track Trigger

The design of the OT is motivated by the necessity to read out and process a substantial volume of trigger data produced by the detector, including the 2S and PS modules, as detailed in Section 2.3.1. By analyzing stubs, keeping into account the two different separation distances 2S sensors (1.8 and 4.0 mm) and the three different distances for PS sensors (1.6, 2.6, and 4.0 mm), an on-detector data reduction by a factor of 10 to 100 can be achieved. The programmable nature of the acceptance window allows for adaptable data rate and transverse momentum filtering across different detector regions. This adaptability enables the reading of stubs at the bunch crossing rate, which is subsequently transmitted to the off-detector L1 tracking system.

With a pileup of 200 events per bunch crossing, simulations predict approximately 15,000 stubs will be generated every 40 MHz. The track finder is tasked with reconstructing tracks within approximately 5 μs, keeping well within the 12.5 μs latency budget allocated for the L1 trigger. The track-finding [37] procedure encompasses stages of data organization, pattern recognition, track fitting, and duplicate removal. This processing is executed on Field Programmable Gate Arrays (FPGA) situated on Advanced Telecommunications Computing Architecture (ATCA) [38] boards. The data is organized regionally (either in η across the azimuthal angle ϕ sectors or in $\eta - \phi$ towers) and distributed in a time-multiplexed manner. Time multiplexing is realized through n identical system copies, utilizing high-speed serial links for data distribution and powerful FPGAs for processing. Stub data are dispatched from the DTCs to each system copy every n $\times$ 25 ns. The DTC output rate is expected to be around 600 Gb/s, with the DTC/L1 track finding interface comprising 25 Gb/s optical links.

The current design, termed the 'hybrid approach,' emerges from the combination of two distinct methodologies: the 'TMTT'[39] and the 'Tracklet'[40] approaches. The algorithm comprises two stages, each derived from one of the original proposals. The first stage seeds the algorithm by generating potential tracks from pairs of stubs across different module layers and projecting these onto the remaining tracker layers. With the six barrel layers labeled L1-6 and disks D1-5, the seeding pair combinations employed include L1+L2, L3+L4, L5+L6, L1+D1, L2+D1, and D1+D2, D3+D4. This approach ensures high efficiency by minimizing the chance of missing a track across all combinations and guarantees comprehensive coverage of the track-finding region. The 'tracklets' or seeds are projected both radially inwards and outwards from the hit pairs, with a narrow window around the projection searched for compatible hits in other layers. The initial tracklet and stubs from other layers are then merged into a track object. At this stage, only track objects with four or more hits in distinct layers are deemed valid. If multiple track objects share a hit, they are merged into a single object, a step necessitated by the high likelihood of forming duplicate initial tracklets from different seeding layer combinations.

The second stage involves fitting the valid track objects to a set of helical parameters. This fitting employs a Kalman filter [41], adept at both fitting and excluding inconsistent hits within the track object. The algorithm's performance, in terms of efficiency and resolution, has been thoroughly evaluated using software simulations [42]. When implemented in firmware, the design is further divided into more granular modules, as illustrated in Fig. 2.25, to enhance maintainability and facilitate debugging.

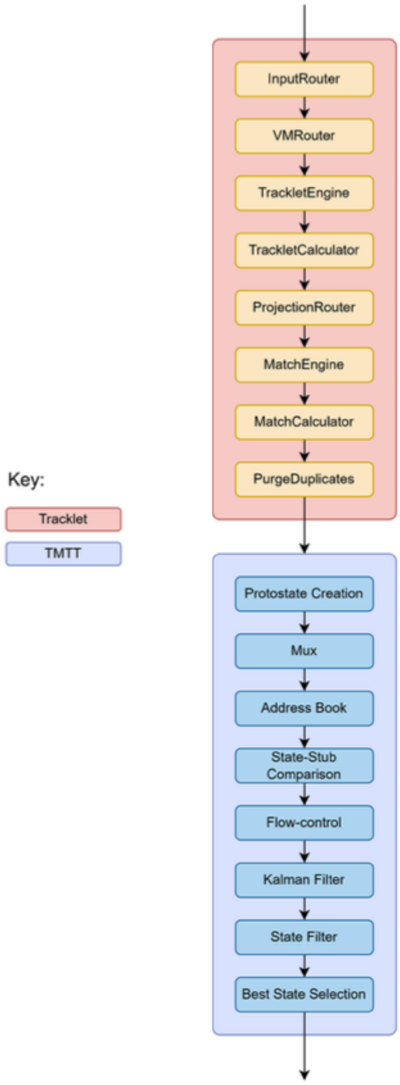

Fig. 2.25: Diagram showing the individual firmware modules for the entire track-finding chain [43].

3 OT Modules assembly

Over the last three years, a comprehensive program to develop and optimize the assembly procedure for OT modules has been carried out. The primary goal of this program has been to define a precise procedure that meets the rigorous demands of both mechanical and electrical tests.

This chapter delves into the assembly process of silicon sensor modules for the OT. Assembling these modules is not just a meticulous task; it represents the confluence of sophisticated technology and precision engineering.

The operating principle of the p_T modules relies on achieving an ideal alignment between the seed and correlation sensors. However, in practical scenarios, perfect alignment is unattainable. Instead, certain tolerances are allowed in the sensor alignment, ensuring that the mechanism remains functional despite minor misalignments. In particular the relative rotation and shifts (parallel and perpendicular to the strip's direction) are the quantities that have a huge impact on p_T mechanism.

The following sections will describe the results of this R&D program. They will explore the various stages of module assembly, starting with the preparation of individual silicon sensors and continuing through their integration with readout electronics and other components. Special attention will be given to the technological advancements achieved in the assembly process, such as automation and quality control measures. Furthermore, the challenges encountered during the assembly process, such as the precise alignment of sensors and ensuring the durability of the modules under extreme conditions, will be examined.

First, the different components of the modules will be described and the requirements for the assembly will be defined. Then, the procedure for assembling PS and 2S modules will be described.

3.1 Modules Components

Both the PS and 2S module types consist of various components that can be categorized into three main groups: sensors, electronics, and mechanics. All the information about the various hybrids can be found in [44], [45] and [46].

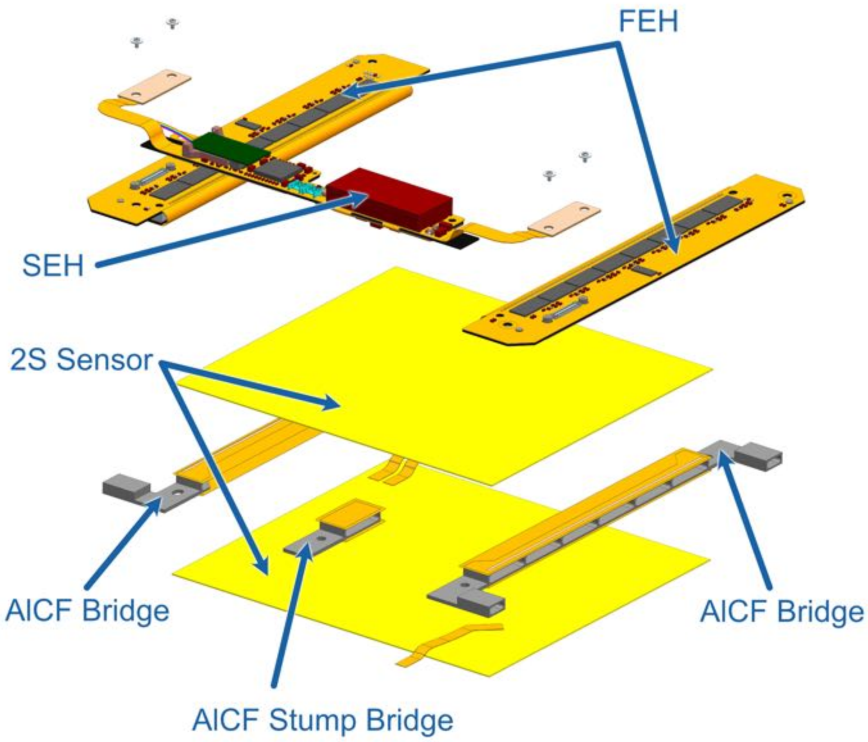

Fig. 3.1: Exploded view of a 2S module, highlighting the different components.

Fig. 3.1 provides an exploded view of a 2S module, illustrating its components. The following is a brief description of these components:

Sensors: 2S modules are made of two identical microstrip sensors. On the back of each sensor, an HV tail is present to bring the bias voltage on the backplane;

FEH: 2S module Front-End Hybrid, hosts the microstrips readout chip (CBC) and the concentrator chip (CIC);

SEH: 2S module Service Hybrid, hosts all the circuitry responsible for generating and providing the different voltages needed by the module. It also contains key components such as the lpGBT and VTRX+ chips. These chips are responsible for managing communication with external systems.

Bridges: Aluminium Carbon Fiber (AlCF) objects responsible for the mechanical separation of the two sensors; two bridges go through the whole sensors parallel to the FEHs while a shorter one, stump bridge, gives rigidity in the middle region. Bridges are also used to mechanically connect the module to the tracker detector structure.

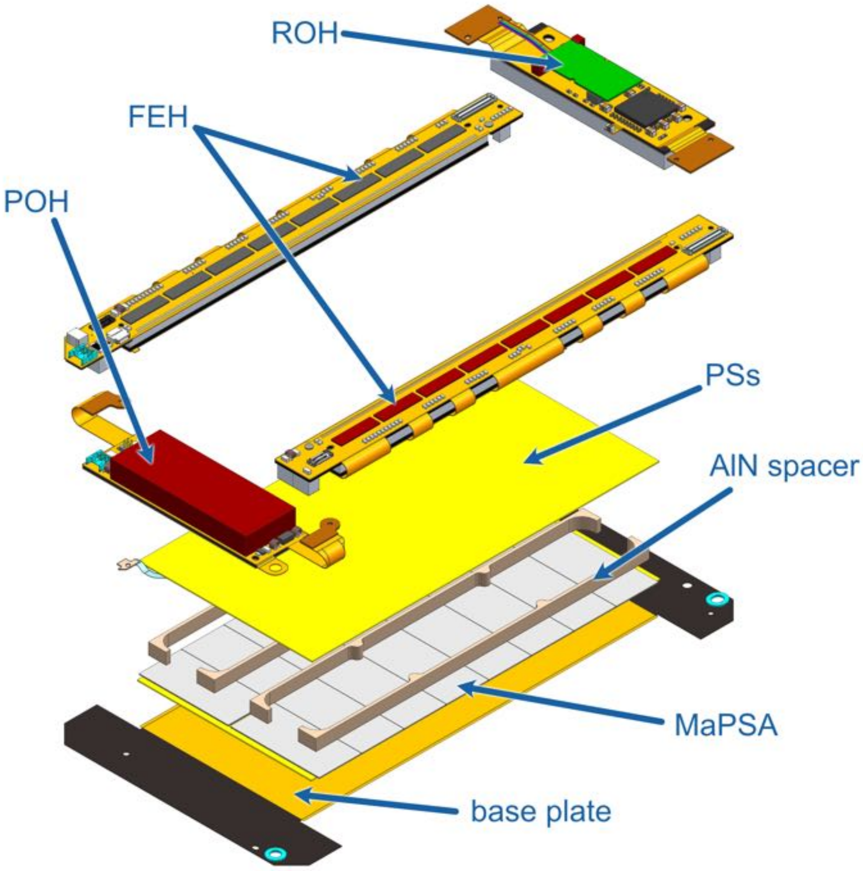

Fig. 3.2: Exploded view of a PS module, highlighting the different components.

In Fig. 3.2 an exploded view of a PS module is shown, with labels for all the components. A PS Module is composed by:

PSs: PS module microstrips sensor, on the back of the sensor an HV tail is present to bring the bias on the backplane;

MaPSA: PS module macro pixel detector, a macro pixel sensor with MPA readout chip bump bonded;

FEH: PS module Front-End Hybrid, hosts the microstrips readout chip (SSA) and the concentrator chip (CIC);

POH: PS module Power Hybrid, hosts all the circuitry responsible for generating and providing the different voltages needed by the module;

ROH: PS module Read-Out Hybrid, hosts the lpGBT and VTRX+ chips which manage the communication with external systems.

Spacers: Aluminium nitride (AlN) ceramic objects responsible for the mechanical separation of the two sensors;

Baseplate: Mechanical base made of a 3-plies Carbon Fibre (K13D2U) in an EX-1515 Cyanate Ester matrix, responsible for the mechanical connection of the module to the tracker detector structure.

Two types of epoxy glues are used for the modules' assembly: a low-viscosity one (Polytec 601LV) and a high-viscosity thermal conductive one (Polytec TC437). The low-viscosity glue is usually used to stick together very flat and smooth surfaces. If one of the two surfaces is rough or the planarity is not perfect, though, the high-viscosity glue allows for better coverage and minimizes the risk of having blank spots. Both types of glue have a curing time of 24 hours at room temperature, as a consequence this is the minimum time to wait between two consecutive steps.

3.2 PS Modules Assembly

In this section, all the steps to build a PS module will be described. This process goes through:

1. Gluing of aluminum inserts on the baseplate;
2. Gluing of polyimide sheet on the baseplate;
3. Gluing of HV tail on the back of the PSs sensor;
4. Wire bonding of the HV tail to the sensor backplane;
5. HV tail bonds encapsulation;
6. Gluing of the spacers on top of the MaPSA sensor;
7. Gluing of the PSs sensor on top of the MaPSA+spacers;

8. Metrology measurements to check PSs to MaPSA alignment;

9. Gluing of the MaPSA+spacers+PSs on the baseplate;

10. Gluing of the electronics (FEHs, POH, ROH);

11. Wire bonding of both PSs and MaPSA to the FEH;

12. Encapsulation of the bonds.

Some of the steps involve independent objects so they can be parallelized, i.e. preparation of the baseplate (items 1 and 2) can be done in parallel with the HV tail gluing and wire bonding.

3.2.1 Baseplate preparation

The assembly of the PS module begins with the baseplate preparation which consists of gluing three aluminum inserts, a small washer, and one polyimide sheet on the baseplate itself. The polyimide sheet is needed to electrically isolate the backplane of the sensors, which will be biased with negative voltage, from the baseplate which is directly connected to the cooling circuitry of the CMS tracker and thus to electrical ground.

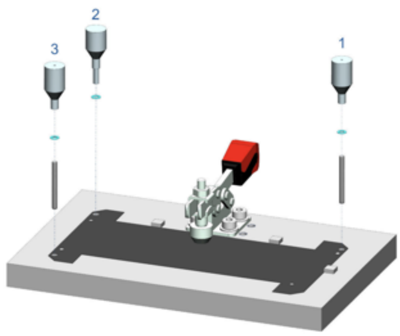

Fig. 3.3: Drawing of the fixture used for inserts gluing.

Fig. 3.4: Process of gluing one of the inserts of the baseplate of a PS module.

In Fig. 3.3 a rendering of the fixture developed to glue the inserts on the baseplate is shown. The fixture is composed of a simple aluminum plate with three stops for baseplate alignment and three holes where heavy pins (1, 2, and 3 in the figure) will be placed for insert positioning.

First of all the baseplate is carefully placed on the jig and secured with a toggle clamp. Inserts are placed on the heavy pins which are then inserted in the positioning holes. The low-viscosity glue is then manually applied at four points around each insert, as visible in Fig. 3.4. After 24 hours, the heavy pins are removed, and the baseplate is released and cleaned for the next step.

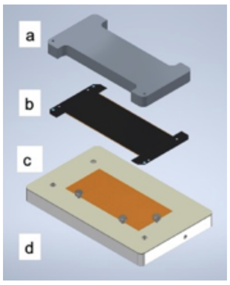

Fig. 3.5: Drawing of the fixture for polyimide sheet gluing for PS modules. In d, the mainplate is visible, in c the polyimide sheet, in b, the baseplate, and in a the weight used to ensure even glue distribution.

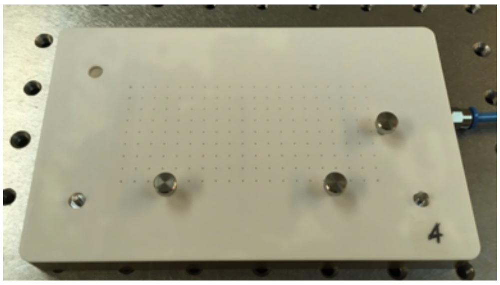

Fig. 3.6: Picture of the main plate used for polyimide sheet gluing for PS modules.

In Fig. 3.5 a rendering of the fixture used to glue the polyimide sheet on the baseplate is shown. The main plate, Fig. 3.6, is composed of a steel plate covered in Teflon with three removable pins to align the polyimide sheet and two fixed pins to place the baseplate. The small hole matrix is needed to keep in place the polyimide with vacuum. The gluing proceeds as follows: the polyimide sheet is placed on the plate and aligned to the removable pins; once in place the vacuum is opened and the removable pins are removed; the baseplate is placed under a glue dispensing controlled machine, Nordson EV4, and a precise low viscosity glue pattern is deposited on it; the baseplate is then placed face down on top of the polyimide sheet placing the inserts on the fixed pin to assure a good alignment; finally, a weight is placed over the assembly to ensure even distribution of the glue. After this step, the vacuum is turned off to avoid the risk of glue being drawn into the fixture. Then, a 24 hour curing phase starts.

3.2.2 PS strip sensor preparation

In parallel with the baseplate preparation, the attachment of the HV tail to the PS strip sensor's backplane is performed. The fixture used to perform this operation is shown in Fig. 3.7. The sensor (in yellow) is placed on the fixture and carefully pushed against the stops, once in place it's kept in position by the vacuum. The HV tail is positioned onto the sensor and the jig, and its placement is secured by three small pins which define its absolute position and orientation. A small drop of low-viscosity glue is manually applied on the back of the HV tail which is then left free to go on top of the sensors, a small weight bar is placed on the tail to ensure a good glue connection.

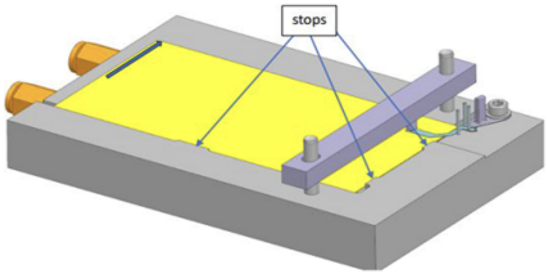

Fig. 3.7: Drawing of the fixture for HV tail gluing for PS modules.

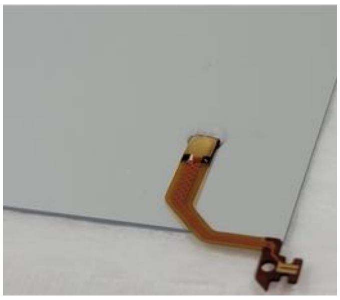

Fig. 3.8: An encapsulated HV tail on a PS sensor.

After the canonical 24 hours for glue curing, the electrical connection between the HV tail and the sensor backplane is established through wire bonds. After removing the weight bar, the fixture with the sensors and HV tail is placed inside the bonding machine where 15 wires are bonded. To safeguard the wires from damage and corrosion, they are completely covered in a silicon elastomer, Sylgard 186 [47]. An encapsulated HV tail is visible in Fig. 3.8.

3.2.3 Bare module assembly and metrology

Two different procedures have been developed by the CMS collaboration to glue together the two sensors, PS strip, and MaPSA: an automated and a manual one. While both approaches share similarities in their fundamental process, each method possesses unique characteristics and steps that differentiate them from each other. The two Italian assembly centers, Perugia and Bari, developed the manual procedure. This procedure will be detailed in the following section.

3.2.3.1 Sensor-to-sensor gluing

The manual procedure starts with spacers gluing on top of the MaPSA, then proceeds with the gluing of the PS strip sensors on top of the spacers creating the so-called "sensors sandwich".

The main fixture used to build the sensors sandwich is shown in Fig. 3.9. This tool is a steel plate equipped with a vacuum chamber and several alignment pins. Specifically, it includes three fixed pins for aligning the MaPSA, two fixed pins for aligning this tool with the one holding the spacer holder (shown in Fig. 3.10), and three adjustable stops that are used to precisely align the PS strip sensors with the MaPSA.

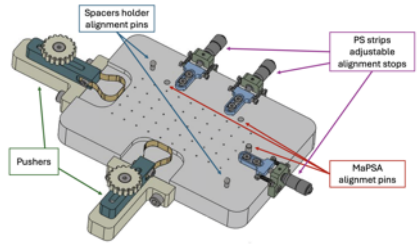

Fig. 3.9: Drawing of the fixture for manual PS sandwich gluing.

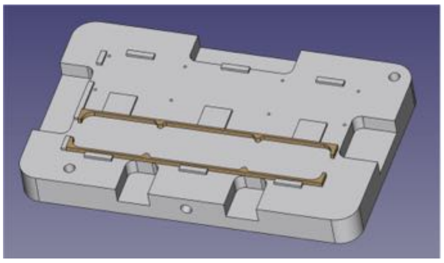

Fig. 3.10: Drawing of the fixture holding sensors spacing for PS modules, in grey the baseplate is visible and on top of the baseplate the spacers are visible.

The first step in assembling the PS module involves calibrating the adjustable stops. These stops can be moved using micrometric screws and then securely locked into position. A key feature of the PS module is the differing dimensions of the PS strip sensor and the MaPSA. Specifically, the Pixel sensor on the MaPSA is 600 μm longer than the PS strip sensor. While both sensors share the same lateral dimensions, the MaPSA includes MPA chips that extend 200 μm beyond each side of the PS strip sensor.

To accommodate these size discrepancies, the two fixed pins for the MaPSA on the longer side are designed to protrude only 200 μm from the plate (less than the sensor's thickness) To take into account these differences, the two fixed pins for the MaPSA on the long side raise from the plate of only 200 μm (which is less than the thickness of the sensor) and the adjustable stops have a pocket on the bottom side to avoid collisions with the MPA chips.

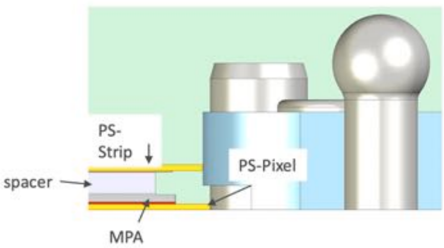

Fig. 3.11: Detail of the adjustable stop and MaPSA pin on the short side of a PS module from the side view of the fixture for calibration.

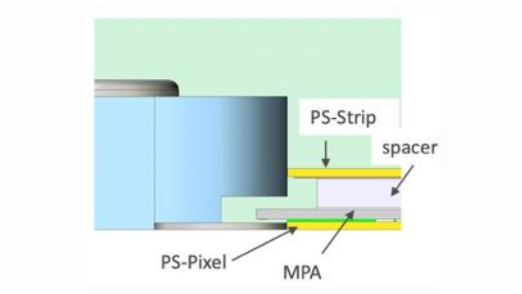

Fig. 3.12: Detail of one of the two alignment points on the long side of the PS module from the side view of the calibration fixture. Adjustable stop pocket in blue.

In Fig. 3.12 and 3.11 two details of the calibration are shown, both pictures are a side view of the fixture. Fig. 3.12 shows one of the two alignment points on the long side, the adjustable stop (blue) pocket can be seen along with the Pixel sensor touching the short pin and the PS strip touching the stops. To calibrate these two points the fixture is placed under an optical metrology machine and the edge of the stops is placed, thanks to the micrometric screws, exactly in line with the short MaPSA pins. On the other hand in Fig. 3.11 a detail of the adjustable stop and MaPSA pin on the short side is shown, here the stop is placed, with the micrometric screw, with a 300 μm shift with respect to the MaPSA pin to accommodate the sensors different length. The calibration doesn't need to be repeated for every module, the plan is to perform the calibration once a month during production.

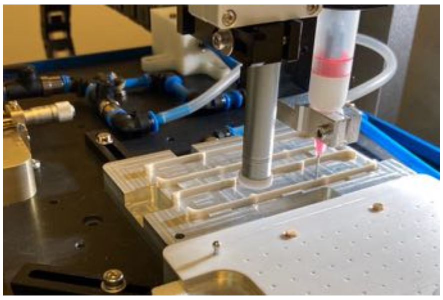

Fig. 3.13: Picture of the gluing process for spacers of a PS module.

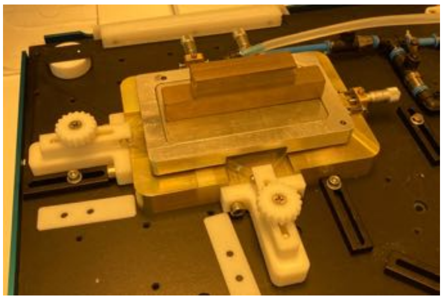

Fig. 3.14: Jig for PS modules spacers gluing during the 24-hour curing period.

Once the main jig is calibrated the sensor sandwich procedure can start. The initial step involves placing the MaPSA sensor on the jig with its backplane facing downwards. This sensor is then pushed against the alignment pins using two pushers. Once in position, its placement is secured by activating the vacuum on the jig. Following this, the four spacers are positioned on the holding jig, as shown in Fig. 3.10. These spacers are held in place by the vacuum to ensure proper alignment and stability during the assembly process. High-viscosity glue is then deposited on top of the spacers, through the use of a glue dispensing controlled machine, Fig. 3.13. To conclude this step the spacers holder is placed on the main jig, and the relative alignment is provided by two dedicated pins. In Fig. 3.14 a picture of the two fixtures coupled is shown, an additional weight is added on top during the 24 hours of curing to efficiently squeeze the high viscosity glue.

Next, the sensor sandwich is formed without moving the MaPSA. The spacers holder is removed and the main jig with MaPSA+spacers is positioned on the glue dispensing robot's area. High viscosity glue is dispensed on the spacers, Fig. 3.15, and the strip sensor is placed on top to create the sandwich, Fig. 3.16. Pushers (visible in Fig. 3.21), raised to touch only the PS strip sensor, are used for alignment. A weight is added on top for planarity and correct glue thickness, with another 24-hour curing period.

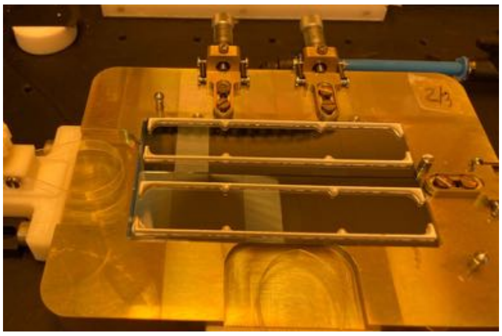

Fig. 3.15: MaPSA with glued spacers.

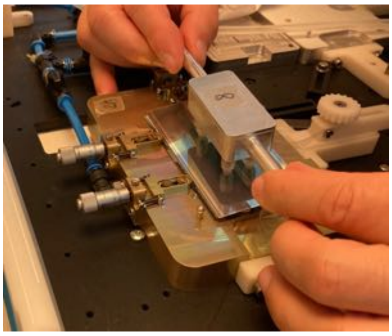

Fig. 3.16: Positioning of the PS strip sensor on top of the spacers to complete the sandwich.

3.2.3.2 Sensors sandwich on baseplate

To complete the bare module the sensor sandwich is glued onto the baseplate. The 3D rendering of the fixture used to perform this step is shown in Fig. 3.17. The fixture is quite simple, it has three short pins to align the sensor sandwich, two pushers to keep the sensor sandwich in position, and two longer pins to align the baseplate.

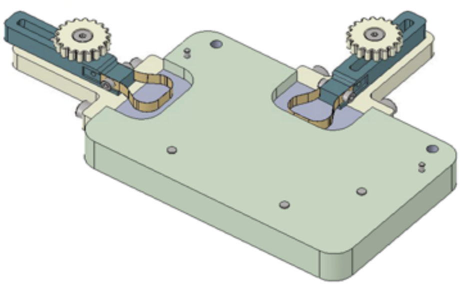

Fig. 3.17: Fixture to glue the PS sensor sandwich to the baseplate.

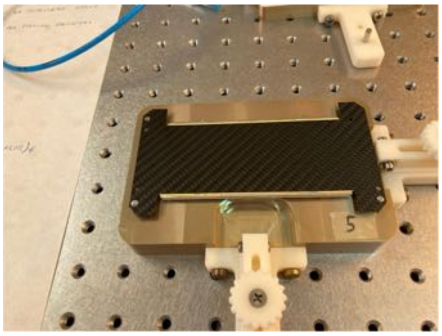

Fig. 3.18: Glued PS sandwich.

The sensor sandwich is placed on the fixture with the PS strip sensor facing down and carefully pushed against the alignment pins with the pusher. The previously prepared baseplate is then placed under the glue dispensing robot and the low viscosity glue is precisely deposited. The baseplate is then placed face down on the sensor sandwich, aligned with two pins, Fig.3.18. A weight is added on top, and the glue cures for 24 hours. This completes the bare module, making the module ready for readout hybrid integration.

3.2.3.3 Metrology

Before the module is completed with the electronics a check of the sensor-to-sensor alignment is mandatory, if a bare module exceeds the tolerances on sensor rotation and shifts it will be discarded. The limits set by CMS for the proper functioning of the PS module are:

- Rotation between the two sensors: $< 800\,\mu rad$.
- Translations in the direction of the strips $< 100\,\mu m$.
- Translations perpendicular to the strips $< 50\,\mu m$.

Metrology measurements for PS modules are relatively simple. This simplicity is due to the MaPSA extending 600 μm longer than the strip sensor, which makes the fiducial marks on both sensors easily visible from above using a camera. By examining these fiducial marks, the relative positioning of the two sensors can be accurately determined. Tab. 3.1 provides a list of PS prototypes along with their respective sensor-to-sensor alignment values.

PS Module	**Rotation (μrad)**	**Shift $\parallel$ (μm)**	**Shift $\perp$ (μm)**
PSproto 1	425	4	-4
PSproto 2	2500	7	-34
PSproto 3	25	-2	10
PSproto 4	145	3	2
PSproto 5	60	4	-6
PSproto 6	20	3	4
PSproto 7	-100	15	5
Mean $\pm\ \sigma$	96 $\pm$ 179	6 $\pm$ 4	-5 $\pm$ 14

Tab. 3.1: List of some PS prototypes with their related metrology measurements, Mean $\pm\ \sigma$ have been calculated only with in-specs modules.

All the prototypes meet the CMS tolerances but one where the rotation exceeds the limit value by a factor of three. The cause of this high rotation was due to a human error during the placement of the PS strip sensor on top of the MaPSA.

3.2.4 Hybrids gluing

The hybrids gluing represents the last step involving glue. High viscosity glue is used for all the hybrids (FEHs, POH, ROH). To guarantee the module's functionality and precision, stringent alignment standards are enforced. The transverse alignment error between the PS strip/MPA and FEH bond pads must be kept below 200 μm, while the height difference should not surpass 300 μm. Additionally, the gap between the PS strip/MaPSA and the hybrids is required to be less than 200 μm. For the POH/ROH, the maximum allowed placement error is restricted to 100 μm from the reference position.

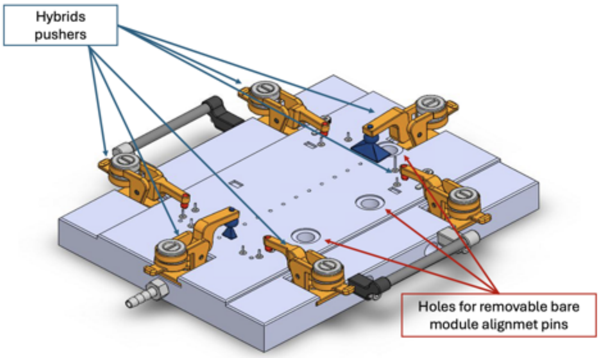

Fig. 3.19: Drawing of the fixture used for hybrids gluing.

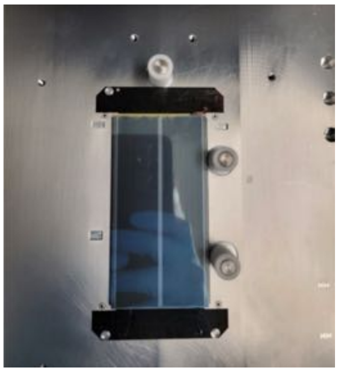

Fig. 3.20: PS sandwich aligned through pins on the proper jig.

In Fig. 3.19 a rendering of the fixture used for this step is shown. The jig is a steel plate with six pushers to keep the hybrids in place, several small pins to align the hybrids, and 3 removable big pins (not present in the rendering) used to put the bare module in place before the vacuum is turned on. In Fig. 3.20 the placement of the bare module is shown. The object is gently pushed against the big pins and once the vacuum is opened, the pins are removed. At this point all the small pins needed to align the hybrids are inserted, once this is done the gluing process starts.

The first hybrid to be placed is the POH. A uniform layer of glue is manually dispensed on the back of the hybrid and then it is put in position with the help of two pins. The relative pusher (top right in Fig. 3.19) is engaged to squeeze the glue and have a good connection with the baseplate. After the POH it's the time of the FEHs. These hybrids are also glued on the baseplate with two small glue joints on the two ends. Glue is dispensed manually for these hybrids too, and two pins for each FEH are used to align it with the bare module. Two pushers for each hybrid are then engaged. After the FEHs are in place, the POH tails, which are below the FEH, must be bent to mate the connector on top of the FEH.

The last step is ROH gluing. The glue is manually dispensed on the back of the hybrid which is then placed on the fixture. Two pins define the position of the hybrid but an additional four pins (two on each side) are needed to align the ROH tails to the FEHs to have the connectors perfectly aligned. Fig. 3.21 shows a picture showing a module in the process of the gluing of the hybrids. The fixture is then left in storage for 24 hours to let the glue cure, then the PS strip HV tail is connected to the right FEH (Fig. 3.22).

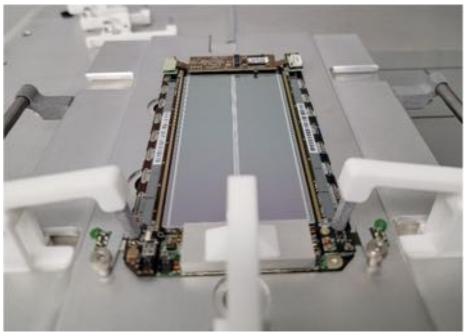

Fig. 3.21: Hybrid glued to the sensor, the pushers keeping in place the POH are visible.

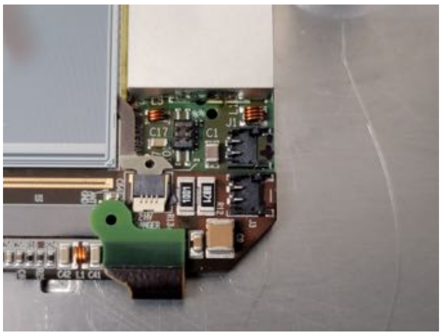

Fig. 3.22: PS strip sensor HV tail connected to the right FEH.

3.2.5 Wire bonding and encapsulation

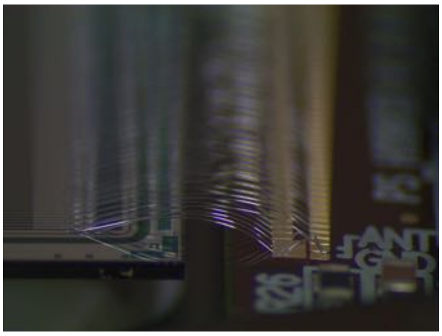

Fig. 3.23: Wire bonds between the PS strip sensor and the FEH.

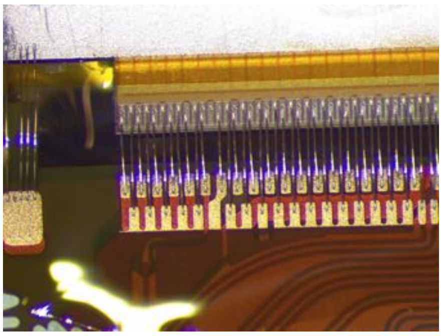

Fig. 3.24: Wire bonds between the MaPSA and the FEH.

The last step of the module assembly is the wire bonding and encapsulation. The module is transferred to ad hoc fixtures (one for the bonding of the strip side and one for the MPA side) and placed inside the bonding machine. The one used in Perugia is a Delvotek M17L.

Each module has 960 bonds on each sensor side for the strips (Fig. 3.23), 3 bonds on each corner of the sensor for the ground connection, 936 bonds on each side for the MaPSA (Fig. 3.24), and 6 bonds for the bias of the Pixel sensor.

The specifications for wire bonding in the construction of PS modules are detailed and precise to ensure optimal sensor performance. The height of the wire must be less than 700 μm above the PS sensor top face and less than 300 μm above the MPA face. Each PS sensor should have 2-3 bias bonds, and while the goal is to have no missing PS strip sensor readout wires, up to two missing wires per row of 960 are acceptable. There should be no missing wires between the hybrid and the MPA chip, and only one pair of shorted PS strip sensor readout wires is permissible if it cannot be repaired. Similarly, there should be no shorted wires between the hybrid and the MPA.

The bonding of the prototype done so far completely meets the specifications. This allowed us to already define the machine parameters and programs to completely wire bond a PS module. Time optimization of the bonding process is now under focus, to maximize the availability of the bonding machine.

As for the HV tail, wire bonds within the PS modules are safeguarded by encapsulation with Sylgard 186. This encapsulation requires a 24-hour curing period to achieve optimal durability and protection. Encapsulating the wire bonds is a two-day procedure, allowing for the thorough treatment of both the top and bottom sides of a single module. The height of the encapsulant above the PS sensor top face should remain below 1000 μm and less than 600 μm above the MPA surface. This is to ensure that all wire bonds on the module are fully covered and adequate protection is given without hindering the functionality of the module.

In Fig. 3.25 a fully assembled PS module is shown.

3.3 2S Module assembly

In this section, all the steps to build a 2S module will be described. Even though the procedure is similar to the one for PS modules, it has its peculiarities. This process goes through:

1. Gluing of polyimide strips and HV tail on the backplane of the first sensor (Top);
2. Gluing of polyimide strips and HV tail on the backplane of the second sensor (Bottom);
3. Wire bonding of the HV tails to the sensors' backplane;
4. HV tails bonds encapsulation;
5. Gluing of the "sandwich" sensor-bridges-sensor;
6. Metrology measurements to check sensor-to-sensor alignment;
7. Gluing of the electronics (FEHs and SEH);

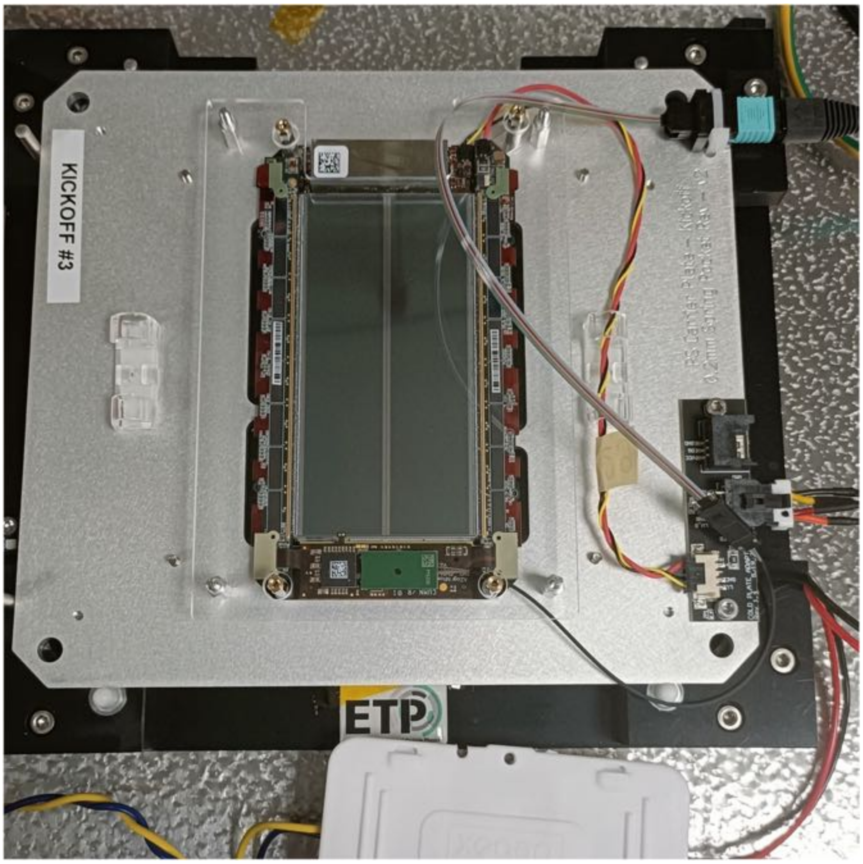

Fig. 3.25: Full PS module after encapsulation. On the long sides, the two FEHs are visible, with the eight SSAs per side. The MPAs are not visible, as they're covered by the sensor. On the bottom, the ROH is visible, with the VTRX+ attached. On the top, the POH is visible, with its DC-DC converter.

8. Wire bonding of both sensors to the FEHs;
9. Encapsulation of the bonds.

3.3.1 Sensors preparation

The AlCF bridges in the 2S modules are electrically connected to the cooling circuitry and the ground of the tracker and keep the sensors separated at the right distance. To ensure electrical isolation up to 800 V, polyimide strips are used. The goal is to maintain 650/700 μm of polyimide between the high voltage potential and the AlCF bridge, with a minimum distance of 500 μm. Approximately 700 μm of overlap is left between the strips and the sensor edge, allowing a placement window of $\pm$200 μm in this direction. In the direction of the bridges, the strips must be entirely within the sensor, providing a placement tolerance of +200/-150 μm, details can be seen in Fig. 3.26.

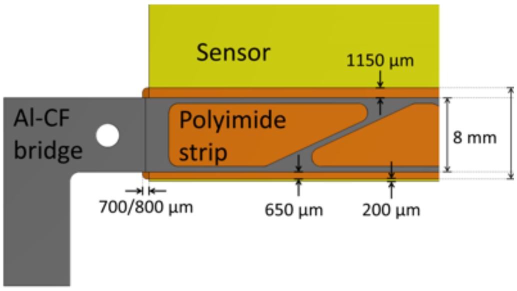

Fig. 3.26: Schematic of the polyimide strip placement for the AlCF bridges.

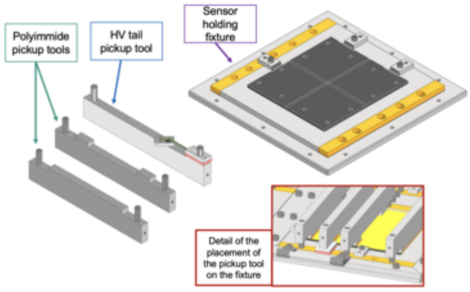

Fig. 3.27: Drawing of the fixture used for sensor preparation.

In Fig. 3.27 a rendering of the different components of the fixture used to glue the polyimide strips and the HV tail on 2S sensors. It is composed of a sensor holding plate with three stops for sensor alignment and precision holes for strips and is completed by the HV tail pick-up tool. The sensor is placed face down on the holding

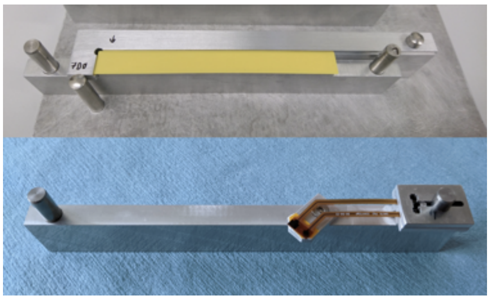

Fig. 3.28: One polyimide strip (top) and top sensor HV tail (bottom) on their pick-up tools.

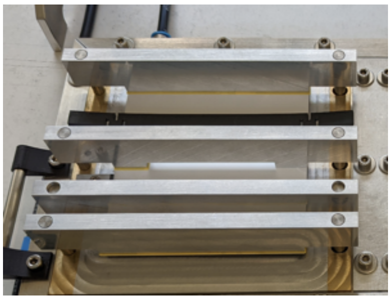

Fig. 3.29: Pick-up tool placed on top of the sensor.

plate, carefully pushed against the stops, and then fixed with a vacuum. The fixture is then placed under the dispensing glue robot which dispenses low-viscosity glue on the sensor backplane exactly where the objects are supposed to be placed. In the meanwhile each polyimide strip is placed on the pick-up tool and aligned with the help of an L-shaped stop and the HV tail is positioned on its pick-up tool. The HV tails on the top and bottom sensors are different: on the top one, the HV tail has two connectors, one for the bias and one for a thermistor, while on the bottom sensor, the HV tail has only one connector for the bias. Fig. 3.28 shows one polyimide strip (top) and top sensor HV tail (bottom) on their pick-up tools.

To complete this step the pick-up tools are placed on top of the sensor holding fixture via precision holes, a picture of the pick-up tools in place is shown in Fig. 3.29.

After 24 hours, for glue curing, the pick-up tools are removed and the fixture is placed on the wire bonding machine to connect the HV tail to the sensor backplane. The HV tail is finally encapsulated with a drop of Sylgard 186, Fig. 3.30.

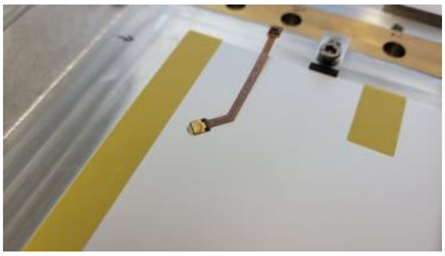

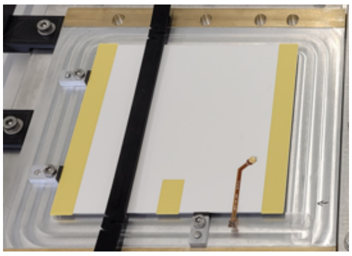

Fig. 3.30: Encapsulated HV tail for 2S module on a top sensor.

Fig. 3.31: Encapsulated HV tail for 2S module on a bottom sensor.

This procedure is done for top and bottom sensors in the same way, the only difference is on the different HV tail, in Fig. 3.31 a bottom sensor at the end of this stage is shown.

3.3.2 Bare module assembly and metrology

3.3.2.1 Bare module assembly

Once the preparation of the top and bottom sensors is finished the following step is the bare module assembly. This step is crucial since it defines the relative positioning of the two sensors.

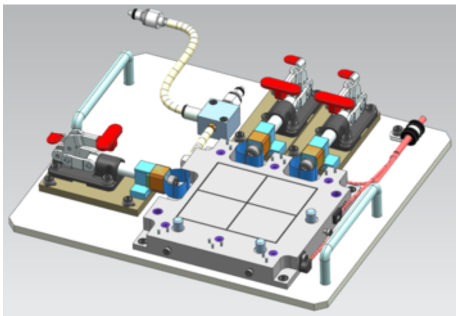

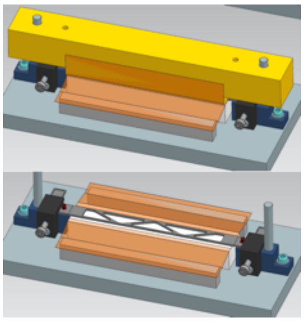

Fig. 3.32: Drawing of the Jig used for 2S sandwich assembly.

Fig. 3.33: Tool for glue placement on bridges (in grey in the bottom figure) for 2S modules.

The fixture used at this stage is shown in Fig. 3.32, it is composed of a steel plate with three pushers, sensors alignment big pins, and several smaller pins for bridge placement. In Fig. 3.33 the tool used to deposit the glue on the bridges is shown.

The bottom sensor is placed face down on the main fixture, the pushers are engaged to align the sensor on the stop pins, and finally, the vacuum is turned on and the pushers are released. At this point with a spatula a thin layer of high-viscosity glue is

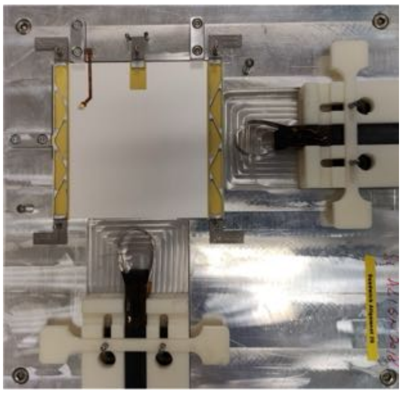

Fig. 3.34: Gluing of the Al-CF bridges on the bottom sensor of a 2S module.

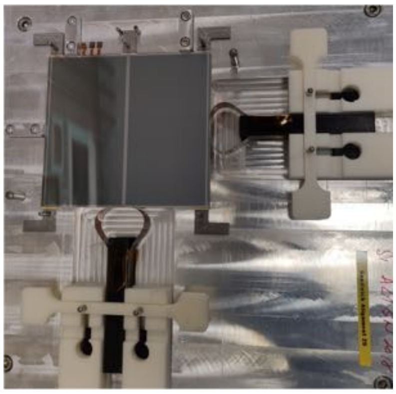

Fig. 3.35: Gluing of the top sensor of a 2S module.

spread on the bottom (white) and top (orange) parts of the glue tools on Fig. 3.33. The bridges are then placed one by one in the bottom part of the tool and the top part is inserted to have the glue dispensed on both sides of the bridges. Once the glue has been dispensed, the bridge is removed and placed on the main fixture using its proper pins. The bridges placed on top of the bottom sensor are shown in Fig. 3.34. The following step is to place the top sensor, face up, over the bridges and then to engage again the pusher to align also the top sensor to the same stop pins as the bottom one, Fig. 3.35. Finally, a weight is added on top of everything to ensure better gluing and uniform glue distribution.

3.3.2.2 Metrology

After 24 hours the bare module can be removed from the jig and alignment measurements between the two sensors are then performed. The limits set by CMS for proper functioning of the module are:

- Rotation between the two sensors: $< 400\,\mu$rad.
- Translations in the direction of the strips $< 100\,\mu$m.
- translations perpendicular to the strips $< 50\,\mu$m.

In 2S modules, contrary to the PS module, the two sensors have the same dimensions and they are placed back to back. This makes it impossible to see the fiducial markers from both sensors together. To overcome this difficulty three techniques have been developed by the community for alignment measurements:

Double-sided Metrology Machine: Utilizes pattern recognition on both sides of the sensor sandwich and a common rotation axis to establish a reference between the top and bottom sensor.

Needle-based: Bias needles beside the bare module serve as reference points to the sensor masks.

Laser-based: Measures relative distance between both sensor edges along the module side, providing only edge alignment. Optical measurement of the dicing edges is necessary to get strip-to-strip alignment.

In Perugia needle-based metrology has been adopted. The bare module is placed on a special jig with a large aperture along the long side of the sensors to allow looking at the two sensors by just flipping the jig. Three small needles are placed at three corners in a position that lets them be visible from each side. The jig with the top sensor facing up is placed under the optical metrology machine and the position of the three needles along with the position of the precision marker on the four corners of the sensor are recorded. Then, the jig is flipped to have the bottom sensor facing

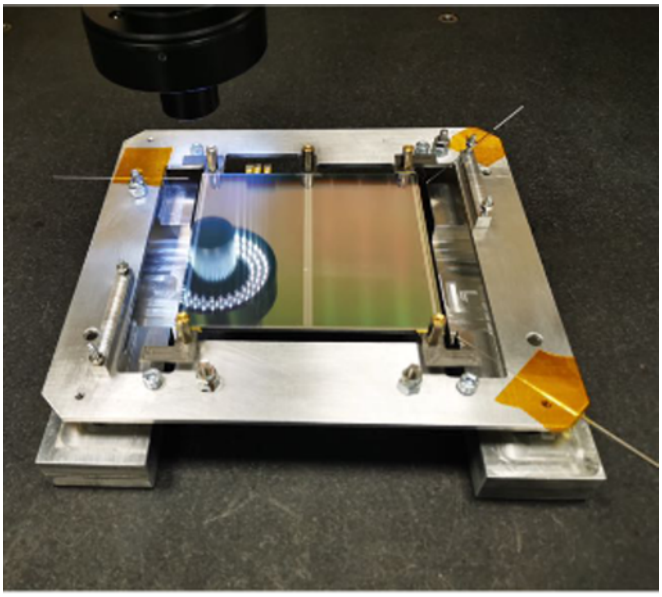

Fig. 3.36: Needle measurement setup for metrology used in Perugia.

up and the same measurements, three needles and four sensor markers, are acquired. Offline, with dedicated software, the data collected are processed, the bottom sensor measurements are flipped to be compared to the one on the top sensor, and then the position of the three needles is aligned in the two measurement sets. After this the position of the two sensors can be extracted from the marker measurements and the relative alignment can be evaluated. A picture of a bare module under the metrology machine for the needle-based procedure, as performed in Perugia, is shown in Fig. 3.36.

2S Module	Rotation (μrad)	Shift $\parallel$ (μm)	Shift $\perp$ (μm)
2Sproto 1	135	13	-4
2Sproto 2	120	22	-10
2Sproto 3	170	39	4
2Sproto 4	45	6	-15
2Sproto 5	400	3	-9
2Sproto 6	90	-5	14
2Sproto 7	100	9	4
Mean $\pm\sigma$	151 ± 108	12 ± 13	-2 ± 9

Tab. 3.2: List of some 2S prototypes with their related metrology measurements.

Tab. 3.2 provides a list of 2S prototypes along with their respective sensor-to-sensor alignment values. All the prototypes built in Perugia meet the requirements for the CMS OT Tracker modules.

3.3.3 Wire bonding and encapsulation

Each 2S module contains over 4000 wire bonds, linking each strip to the corresponding pad of the CBC. Each sensor needs 1016 bonds on each side, and then three ground bonds are placed at each corner of each sensor. The wire bonding process is carried out using the Delvotek M17L wire bonding machine. In Fig. 3.37 a 2S module during the wire bonding process is shown, a detail of the module after the wire bonding can be seen in Fig. 3.38.

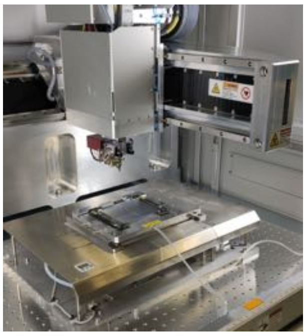

Fig. 3.37: 2S module inside the wire-bonding machine.

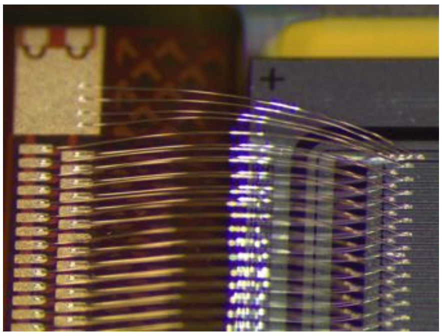

Fig. 3.38: Detail of the wire bonding.

As for PS bonds, it is crucial to shield the wire bonds from mechanical damage and electrochemical corrosion, therefore, they are encapsulated with a silicon elastomer, Sylgard 186.

In Fig. 3.39 a picture of a full 2S prototype module at the end of the assembly procedure is shown.

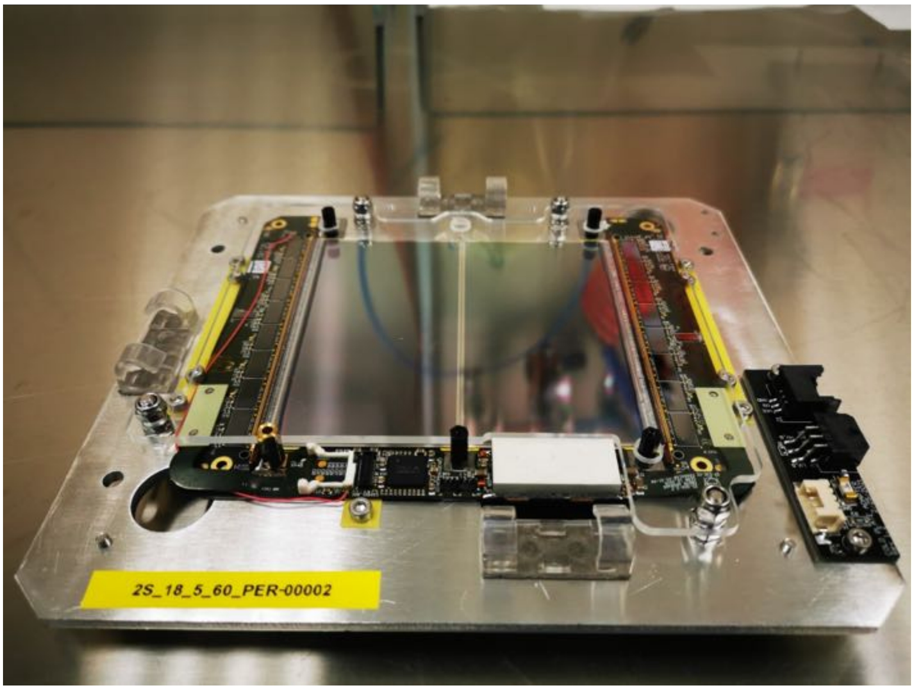

Fig. 3.39: A completely assembled 2S module prototype. On the left and right, it's possible to see the two FEH, with the eight CBCs. In the forefront, the SEH is visible.

4 DAQ development

The development of the Data Acquisition (DAQ) system for the OT modules is a multifaceted task. It necessitates the creation of tools for both data acquisition and the setup and calibration of the modules. These tools must accommodate two distinct configurations: a test setup and a final setup. The test setup, designed for early assembly stages, enables the readout of a limited number of modules to verify their functionality. Conversely, the final setup, employed in the upgraded OT, encompasses not only the configuration and setup functionalities for the modules but also the capability to configure and read out a large number of modules simultaneously. It integrates their data handling errors and coordinates conversion and relays it to the track-finding system for L1 trigger information processing.

The entire system is based on FPGA technology, featuring different boards for each setup. The test system utilizes the Micro Data, Trigger, and Control (μDTC) [48] board, while the final system employs the DTC board. This chapter will first describe the test system setup, outlining the specific calibration tasks required for the modules. Subsequently, an overview of the final DAQ system will be presented, detailing the software advancements made in recent years to adapt the software developed for the μDTC for use with the DTC.

4.1 System test

The μDTC project plays a pivotal role in testing various iterations of front-end ASICs and offers a comprehensive interface for managing module prototypes through both electrical and optical interfaces. This project's main goal was to serve as the DAQ system during the production and integration phases of the OT and IT modules. A schematic of the system is visible in Fig. 4.1.

At the heart of the μDTC system lies the FC7 [49] board: a versatile component based on the Micro Telecommunications Computing Architecture (μTCA) [50] standard, which will be described in detail in Sec. 4.1.1. This standard allows for the integration of multiple computing units, known as Advanced Mezzanine Card (AMC), into a single μTCA crate. Within this crate, a MicroTCA Control Hub (MCH) unit oversees the system's overall control, and monitoring, and facilitates data transfer to the

PC, adhering to the GigaBit Ethernet standard. For scenarios requiring higher data transfer rates, additional data aggregation units can be incorporated into the μTCA crate.

Interestingly, the FC7 board's design allows for its operation outside a μTCA crate. It can be connected directly to a PC using a dedicated adaptor, showcasing its flexibility in various setups.

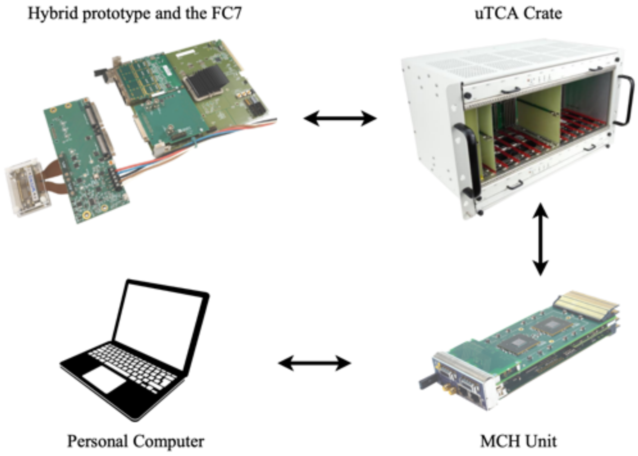

Fig. 4.1: Schematic of the μDTC system [51].

4.1.1 FC7 board

Fig. 4.2: Top view of an FC7 board.

The FC7, visible in Fig. 4.2, is an AMC [49] designed for generic data acquisition and control applications in high-energy physics experiments. It is built around the Xilinx

Kintex-7 FPGA, a versatile component that forms the heart of the FC7's functionality. This FPGA provides a vast array of basic logic elements organized in blocks with a highly flexible interconnect system and a range of I/O, primarily accessible via two on-board FPGA Mezzanine Card (FMC) sockets. A schematic of the different components of the current OT module testing hardware is visible in Fig. 4.3.

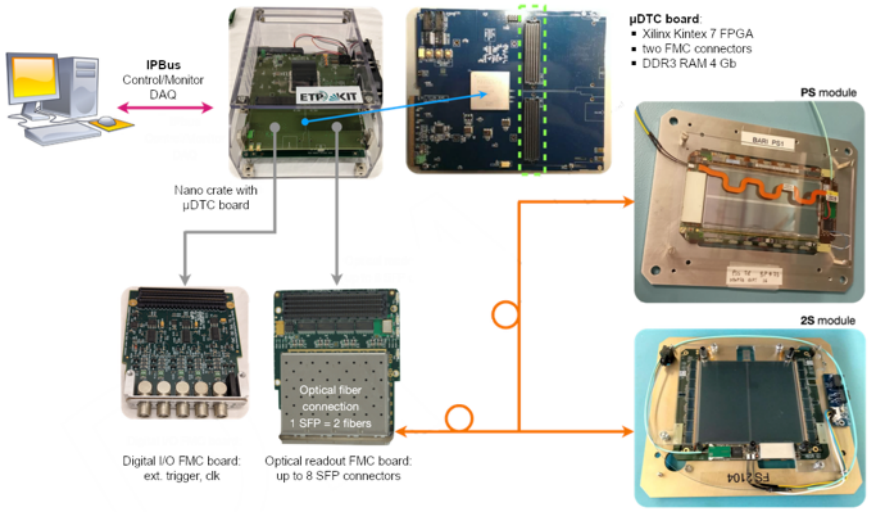

Fig. 4.3: Description of the different components of the current OT module testing hardware with an optical readout chain. In dashed green light, the connector for AMC cards is highlighted.

The FPGA provides an array of basic logic elements organized in blocks and a highly-flexible configurable interconnect system between them, all complemented with a set of I/O blocks. The simplest logic block (also called slice) design features a LUT, the output signal from which depends on the condition of its inputs. From the LUT the output signal is further forwarded to a Flip-Flop (FF) controlled with clock and reset signals and allows to store the received information. A Multiplexer (MUX) is used to select a desired slice output signal either directly from the LUT or after passing the FF. Actual FPGAs feature more complex combinations and larger amounts of logic elements in a similar fashion. The Kintex-7 FPGA in the FC7 contains 74,560 slices, which include a total of 260,600 LUTs, 521,200 FFs, and 89,580 MUXs. Furthermore, the FPGA incorporates 34,380 kB of RAM, optimized for intermediate data storage.

In addition to the FPGA, the FC7 features a clock distribution ASIC to precisely control the frequency and phase of the FPGA clock, essential for various firmware components. The FC7 also includes a Double Data Rate 3 (DDR3) memory chip for intermediate data storage, further enhancing its capability to handle complex data processes.

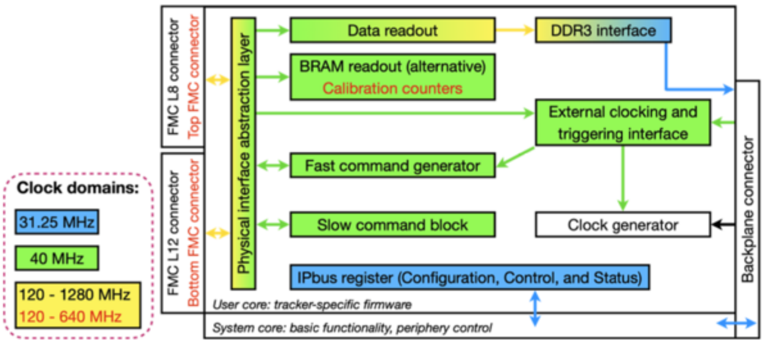

Fig. 4.4: Schematic view showing the different firmware blocks and their relative clock domains, both for IT and OT. Differences for OT are marked in red. In particular, the Data Readout for OT handles both L1-accepted data and the 40 MHz stub data stream.

Equipped with a basic system firmware core, the FC7 controls its peripheral elements, supports μTCA functionality, and manages the communication protocol. However, to fully utilize the FC7's capabilities, this system firmware must be supplemented with user-specific firmware. This customization allows for extending the FC7's functionality to meet specific requirements of various applications, such as the read-out and control of the outer tracker modules.

The firmware used for the system test has to accomplish the following tasks:

1. encode and decode chip commands;
2. send sequences of triggers and injections;
3. store data in a memory buffer;
4. handle external clock and trigger signals;
5. handle handshake to receive event timestamps, typically during beam tests;
6. generalize communication details to support multiple front-end hardware types.

An overview of the firmware blocks is visible in Fig. 4.4.

4.1.2 Module's calibration

Given that each channel per readout chip can have a unique pedestal, whereas the threshold is set for the entire readout chip, offset tuning is essential for calibrating a module. A detailed description of this procedure, using a CBC as an example, is provided here. A similar procedure applies to PS modules as well.

To interpret the binary readout from the chips in terms of analog performance, one typically calculates the occupancy of a given channel while varying the threshold voltage. This threshold voltage, denoted as V_{cth}, is indicated in Fig. 2.20. The resulting plot follows an S-curve equation, where a 50% occupancy corresponds to the pedestal value. By differentiating this S-curve it's possible to extract a gaussian distribution whose σ corresponds to the noise and mean corresponds to the pedestal. These two curves obtained this way are illustrated in Fig 4.5. The V_{cth} is generated by a 10-bit resistor ladder DAC, ensuring a linear and monotonic DAC-to-voltage conversion.

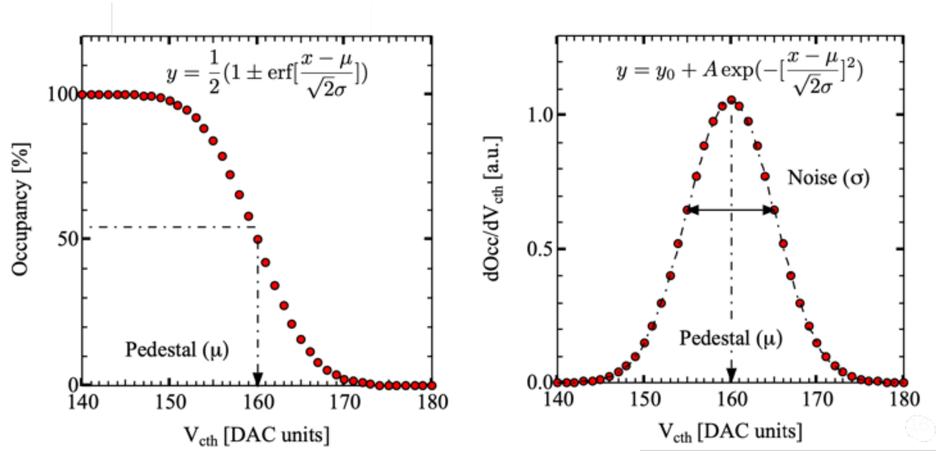

Fig. 4.5: Occupancy vs threshold voltage in DAC unit (left). Gaussian obtained by differentiating the S-Curve in the left figure (right) used to calculate noise and pedestal for a single channel.

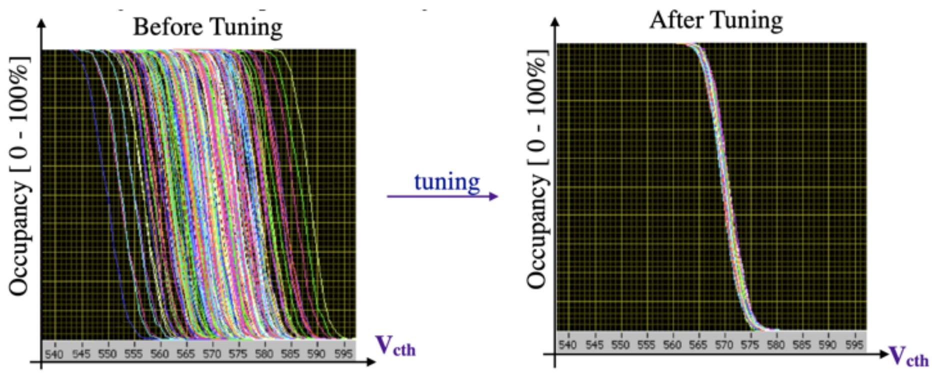

Fig. 4.6: S-Curves for the 254 channels connected to a CBC before (left) and after (right) offset tuning.

Offset tuning is thus a two-step process, controlled by two parameters adjusted by varying the current through the 20 kΩ resistor of the circuit shown in Fig. 2.20. These parameters are controlled through an 8-bit DAC, with a range of approximately 250 to 800 mV. The V_{plus} constitutes the 4 most significant bits, and V_{offset} (indicated as "Offset adjustment" in Fig. 2.20), represents the 4 least significant bits for fine-tuning. Initially, V_{plus} is set to a default value of 500 mV, followed by a V_{cth} scan, resulting in a curve similar to the one on the left in Fig. 4.6, showing slightly different offsets for each channel. Subsequently, a V_{offset} scan is performed to find the optimal value for each channel, aiming to align the curves. The resulting tuned S-curves are visible on the right in Fig. 4.6. Post-offset tuning, it becomes feasible to set consistent threshold values across the entire readout chip and module.

The S-curve measurement also enables inference of per-channel noise, facilitating precise module characterization and identification of assembly inaccuracies. This entire process is software-driven. While hit counts per pixel are performed by the firmware and stored in appropriate registers in PS modules, complete data stream decoding is necessary for 2S modules, as this procedure is not implemented in firmware. One major step needed to go from the system test to the final DAQ system involved adapting calibration and setup software to accommodate differences in data streams, as will be described in Sec. 4.2.1. This adaptation allows for module calibration and measurement using the Serenity board [52], bypassing the need for an FC7. Examples of measurements and calibration processes are shown for 2S modules, via readout through Serenity board, in Fig. 4.7. Calibration examples for PS modules' SSA and MPA chips, via readout through FC7 board, are instead showed in Fig. 4.8 and Fig. 4.9.

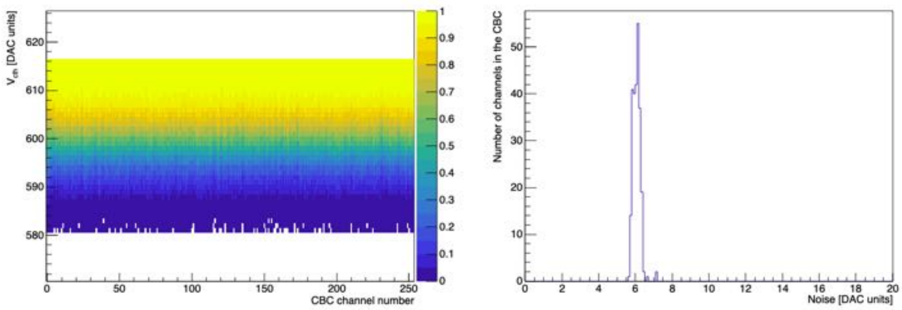

Fig. 4.7: S-curves obtained for each channel in a CBC, after the offset tuning (left). On the z axis, the occupancy of the channel over 100 triggers sent is shown. Noise per channel in DAC unit (right). Obtained through scan with the Serenity.

4.1.3 Hybrid testing setup

To enhance the characterization of hybrids received from manufacturing companies, a specialized hybrid testing setup has been developed. The setup, illustrated on the

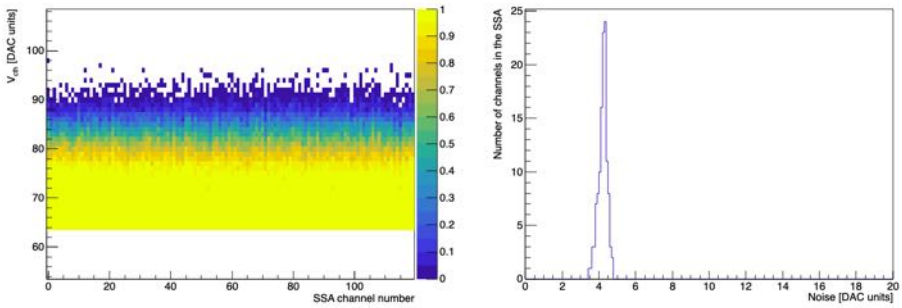

Fig. 4.8: S-curves obtained for each channel in a SSA, after the offset tuning (left). On the z axis, the occupancy of the channel over 100 triggers sent is shown. Noise per channel in DAC unit (right). Obtained through scan with the μDTC.

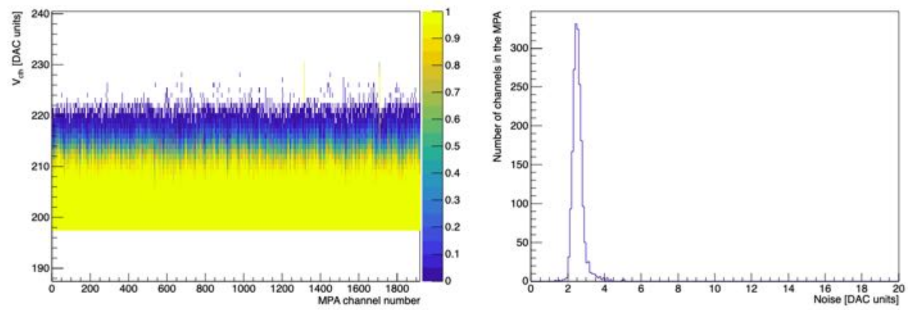

Fig. 4.9: S-curves obtained for each channel in a MPA, after the offset tuning (left). On the z axis, the occupancy of the channel over 100 triggers sent is shown. Noise per channel in DAC unit (right). Obtained through scan with the μDTC.

left in Fig. 4.10, will be installed at the hybrid assembly factory. Its purpose is to test the assembled hybrids for correct assembly and verify the operational integrity of connections between chips, which have been tested by the manufacturer.

The setup consists of a computer equipped with Red Hat Enterprise Linux 8, managing all operations and interfacing with up to three FC7s. These FC7s are utilized for reading out electrical or optical data from the hybrids and for simulating electrical inputs from other chips in the modules, each managing a separate test crate. Each test crate accommodates 12 slots for test cards, essentially adaptors to connect and read out the hybrids' input and output connectors. Jumpers are implemented to connect certain hybrids. The entire assembly is situated in a climatic chamber to maintain optimal humidity and temperature conditions during testing.

Recent years have seen continuous efforts to stabilize a version of the data acquisition software originally developed for the μDTC. Recently, development has focused on strengthening and rectifying certain tests for PS hybrids. This includes addressing

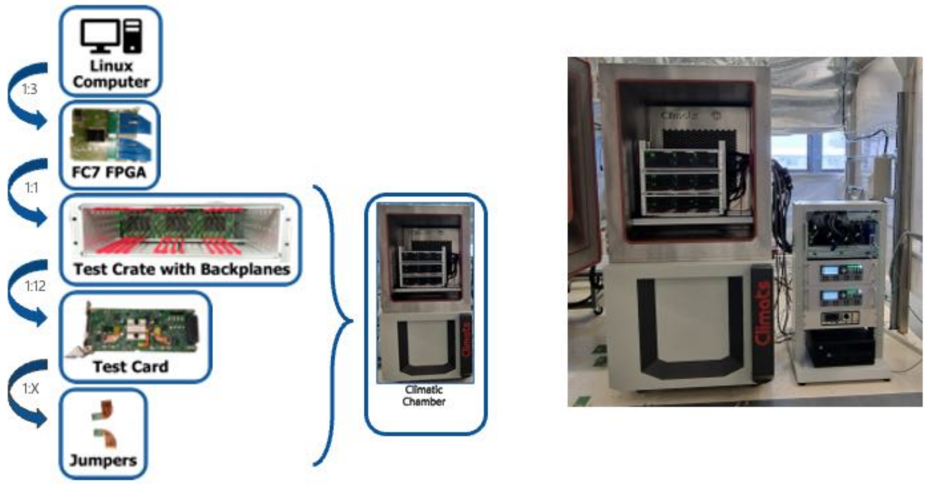

Fig. 4.10: Schematic of the hybrid testing setup (left) and a photograph of the actual setup installed in building 186 at CERN.

issues in the SSA lateral communication lines, the SSA input lines, and the CIC input lines.

The lateral communication of the SSA is crucial as stubs are generated exclusively in the MPA to circumvent edge cases where a particle's hits are at the boundary between SSA-MPA pairs. Before passing strip activation data to the MPA, adjacent SSAs form clusters with the 8 strips in the neighboring SSAs. The goal of this test was to confirm the reliability of these communication lines. The procedure involved:

1. Disabling the analog output for all strips in every SSA;

2. Digitally injecting a strip in an adjacent SSA (in the last or first 8 strips, depending on the side);

3. Verifying if the selected SSA reconstructs the correct centroid.

Initially, some false negatives were observed in these tests. Mainly, two different causes were identified for the false negatives.

First of all, robustness over different patterns was investigated. By introducing configurable centroid injection and embedding encoding and decoding of the pattern in the same software objects, errors related to pattern inaccuracies were fixed. After that, the drive strength for the signal emitted by the SSAs was investigated. Appropriate software scans for this value were implemented and tested multiple times varying hybrids and test cards. This proved that the previous default value was sub-optimal. The implemented procedure lead to zero false negatives across over ten thousand tests on various crates, hybrids, and test cards. Further refinement is possible by by using a debug feature of the SSA, making it possible to inject in every output line a custom pattern, though this has not been deemed necessary.

Regarding the SSA input lines, the test was cured by the false negative observed identifying possible incorrect setup of the firmware blocks handling the data output. The implementation of an appropriate retry mechanism, which reconfigures the firmware block in case of a failure, was the quick fix of choice.

Currently, studies are underway to address issues in the CIC input line tests, where random false negatives have also been noted. The system here is more complex due to the absence of a direct feature for rendering the CIC transparent, necessitating the simulation of inputs through an FC7. Workarounds involve routing the 48 input lines to a common block shared with the lpGbt, which helps in determining phase alignment between lines. Possibilities involve incorrect phase tap selection from both the chip and the FC7, due to degradation of the signal before it's injected in the hybrid. Comprehensive scans for both phases have been conducted, and a software procedure to implement cascade scans to find the best possible phase in case of failure has been implemented. Unintentional behavior has been though still observed and it's under study, via the assembly of module with this hybrids: this will allow testing in real-life scenario and understand if the problem relays in the quality of the signal injected on the hybrid.

4.2 Final DAQ system

The final DAQ system for Phase-2 upgrade of CMS will be based on the aforementioned ATCA standard for processing cards replacing the earlier μTCA standard. ATCA cards, considerably larger than μTCA, offer greater power capacity, facilitating the use of more powerful FPGAs. Up to 14 of these cards can be accommodated in a single crate, with a maximum of two crates per rack. Heat exchangers and water pipes are planned to manage heat dissipation efficiently. Each crate's backplane provides power and other services like network management, while the primary I/O uses optical fibers extending from the crate front.

Both processing cards intended for the tracker back end (BE) are designed for general purposes and are usable in various CMS systems and other experiments. They can support up to two Xilinx Ultrascale+ FPGAs and are equipped with optical transceivers for optimal throughput. A notable advancement in Phase-2 cards is the inclusion of additional computational resources for autonomous control and

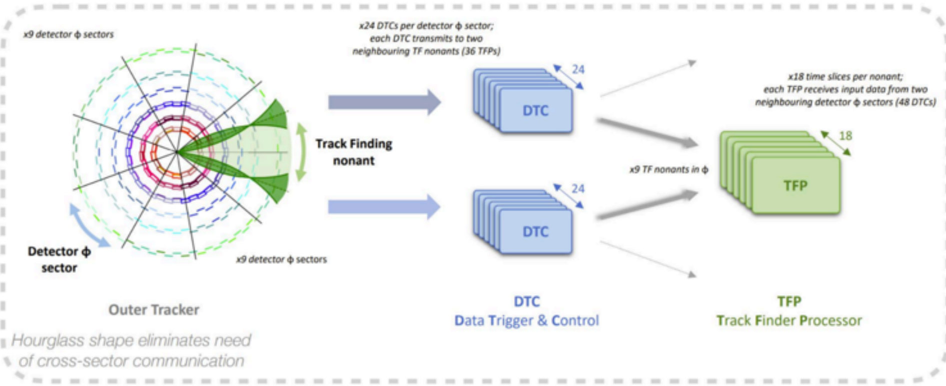

Fig. 4.11: Data handling from different nonants, between DTC and TFPs [53].

management. This is realized through a System-on-Module (SoM), usually based on x86 or ARM architecture, capable of running a standard GNU/Linux operating system. These SoMs enable the development of efficient online software directly on the cards, circumventing the complexities associated with custom embedded system development.

The tracker's BE data handling framework consists of two components: the Data, Trigger, and Control (DTC) board along with the Track Finding Process (TFP). Acting as a bridge to the front-end modules, the DTC decodes and rearranges stub data for efficient processing by the TFP, as visible in Fig. 4.11. Subsequently, the TFP processes this data to form tracks that are forwarded for further analysis. Two boards have been selected for these two different purposes: the Serenity as the DTC, which will be extensively described in Sec. 4.2.1, visible in Fig 4.13 on the left, and the Apollo [54], visible in Fig. 4.13 on the right.

The detector's tracker modules are virtually divided into nine segments in ϕ, termed "nonants", as visible in Fig. 4.12, each processed independently. There are 24 DTCs, each of which is capable of managing 72 link to FE modules, dedicated to each nonant, totaling 216 DTCs for the OT. As depicted in Fig. 4.12, the track-finding process is divided in a similar manner across nonants. However, each is rotated by 20 degrees, overlapping DTC sector boundaries, ensuring accurate track reconstruction across these borders. For tracks crossing DTC sector boundaries, stubs are duplicated and processed in each relevant TFP.

The TFPs adopt a "Time-Multiplexed" architecture: this approach involves gathering, storing, and simultaneously processing data from a single event across multiple processor copies, each working on different events with a Bx offset. This increases the processing time from one Bx to a multiple of N Bx, where N is the period of time-multiplexing. For the TFPs, with a multiplexing period of 18, each processor gets 450 ns for track finding.

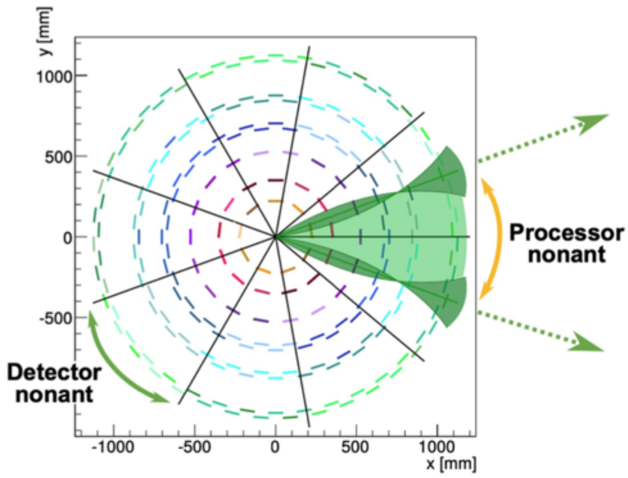

Fig. 4.12: Diagram showing the division of the tracker in nonants, showing also the "hour-glass" sections (highlighted in dark green), where the signal from modules is duplicated in more DTCs.

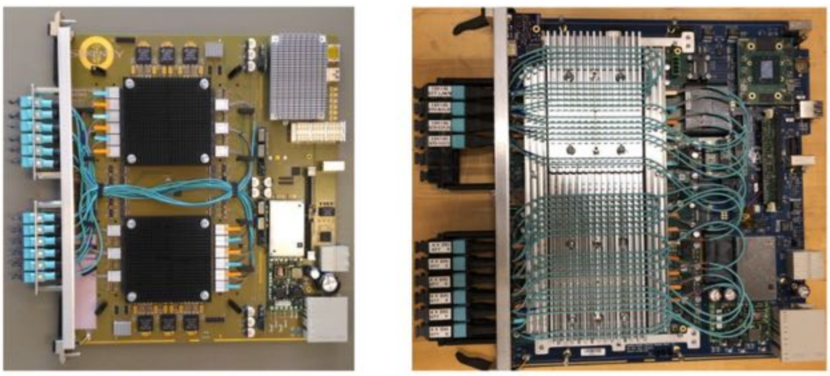

a) Serenity   b) Apollo

Fig. 4.13: Pictures of the two ATCA processing cards selected for the CMS Phase-II tracker DAQ. On the left side, the Serenity board, selected as the DTC, on the right side the Apollo, selected for the Track Finding Process (TFP).

4.2.1 Data, Trigger and Control Board

As mentioned before, the Serenity card is the ATCA chosen for the DTC role. Its adaptability stems from a design incorporating an interposer: this setup allows to decouple the FPGAs, placed on the interposer, from the Printed Circuit Board (PCB) and the commercial CPUs that are then mounted atop the interposer. This structural design allows for flexibility in selecting and replacing different components of the Serenity even after the main PCB assembly, enhancing both versatility and maintainability.

The optical communication on the Serenity board is achieved through a modular approach, using SAMTEC Firefly transceivers [55], making it possible to achieve up to 2.8 Tbps for both receiving and transmitting per PCB.

The design of the Serenity card enables it to support up to two FPGAs. For its specific application for the DTC, the Serenity card integrates a single Xilinx VU13P FPGA [56]. Additionally, the card incorporates a smaller Xilinx Artix-7 class FPGA, tasked with programming and providing timing signals to the larger FPGAs.

In contrast to Serenity, the Apollo board, designed for the TFP, follows a different architectural approach. While it shares the dual FPGA design and SAMTEC Firefly optics with Serenity, Apollo diverges in its method of connecting FPGAs to the board. Apollo achieves various configurations by separating processing elements (FPGA and optics) from service elements (power, timing, management interface) on different PCBs. This design, while enhancing signal integrity due to the direct soldering of FPGAs onto the PCB, limits the ease of replacing the FPGAs compared to the interposer-based approach of the Serenity card.

Concurrently with the new ATCA processing cards, the Extensible, Modular data Processor (EMP) framework was developed. It is a collection of firmware packages aimed at facilitating the rapid development of FPGA algorithms, handling input and output management, timing, and other essential functions, allowing users to concentrate on algorithm design, implementing them in the so-called "payload" block of the firmware. This also makes algorithm designs transferable across different FPGA classes. EMP also includes predefined data types for the payload's input and output buses. The framework is complemented by software tools like 'empbutler', a command-line interface for configuring FPGA clock sources and input/output links.

4.2.2 Data paths

As shown in Fig. 2.18 and explicated in Sec. 2.3.1, two kinds of data stream must be handled by the DTC in the final system: the so-called trigger path, containing information about incoming stubs, which will then be used by the TFP, and the so-called DAQ path, containing all the information retrieved after the L1 trigger, to go to the HLT trigger. The firmware design of the Serenity board takes into account the need to handle both data streams, which will be accurately described in the next two paragraphs.

Some parts of the firmware, though, are somehow shared across the two data paths. The first shared part is the EMP xGBT interface, for which a diagram can be found in Fig. 4.14. This is an interface needed to translate the previously written lpGbt/FPGA firmware block developed by CERN to standard EMP data. It is formed mainly of two parts, a framer, which actually translates the data in EMP compatible format for both receiving and transmitting direction, and a flow control logic, which handles additional commands to the lpGbt, such as slow control commands.

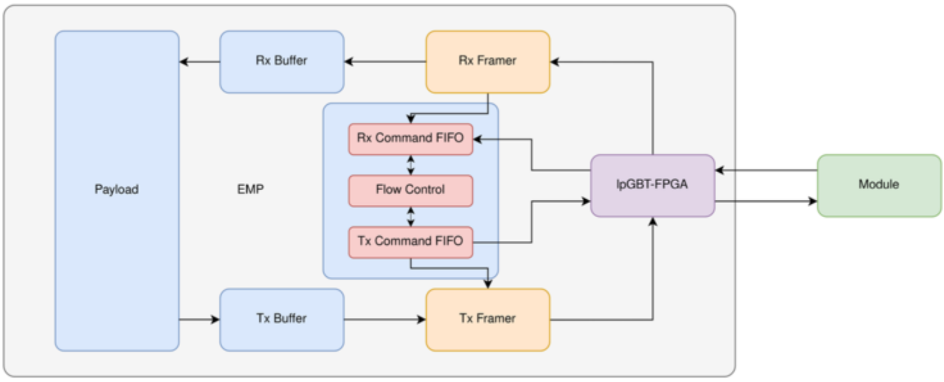

Fig. 4.14: Schematic of the EMP xGBT interface block for the Serenity firmware [43].

The second shared part is the Link Interface, a diagram of which is visible in Fig. 4.15. The link interface is directly connected to the input and output ports of the EMP payload and has to manage both the trigger and L1 (or daq path in the figure) stream in addition to being able to create and send commands to the downstream modules. Part of the job that the Link Interface has to do is also the identification of packets from implicit information, as no header starting sequence is sent. This is done through identification by comparing certain consistent elements across packets, including the module type bit, which stays consistent within a boxcar; padding zeros at the end of the boxcar; and the Bx ID, which, while varying across packets, increments predictably.

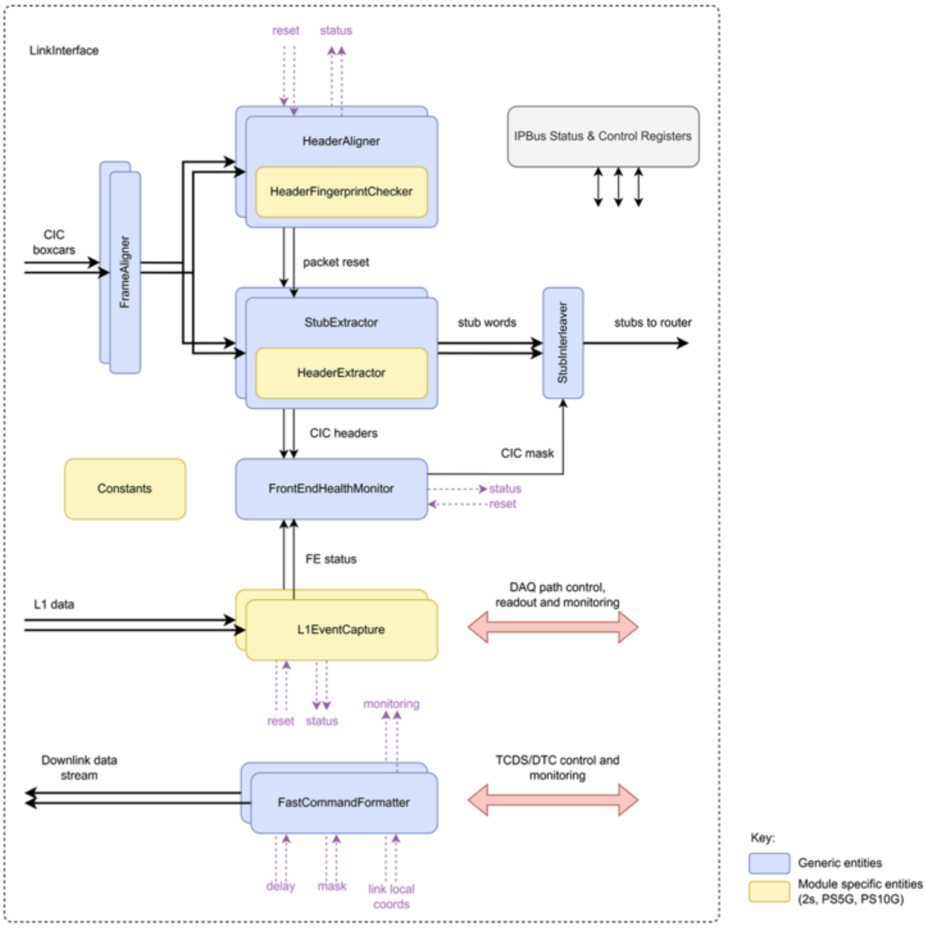

Fig. 4.15: Schematic of the design of the Link Interface block for the DTC [43].

4.2.2.1 Trigger path

The trigger path is the data path followed by stubs, to use them for the TFP. An overview of the firmware block developed for the Serenity board for this path is visible in Fig. 4.16.

The packet transmission from a module CIC over the 6 External Link (e-link) to the DTC occurs over 8 Bxs, in similar ways for PS and 2S modules, as visible in Fig. 4.17. Given that the 8 bits from each e-link from the CIC are sent together, the framer also applies a conversion to EMP-compliant format (column-wise to row-wise), by first arranging the data in a two-dimensional (5,8) array shape and then applying a transpose operation.

Then, stub alignment has to be taken into account, which can derive from two different scenarios: intra- and inter-link misalignments. Intra-link Misalignment occurs when the e-links are not synchronized. A misaligned e-link can cause a bit to

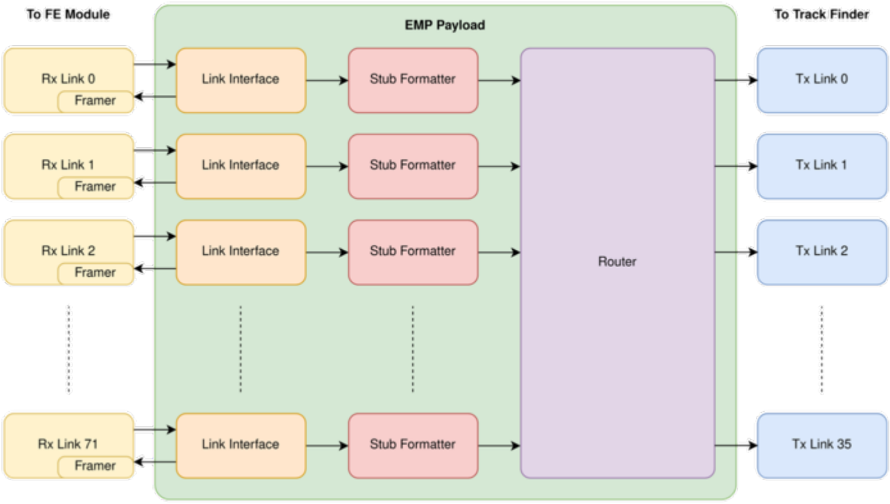

Fig. 4.16: Schematic of the firmware previewed for the trigger path in the final system for the DTC [43].

arrive either earlier or later than others, leading to that bit being placed in a different word by the framer. It's possible to correct this at a module level, where individual e-links can have delays introduced to align them once a misalignment is detected. Alternatively, a similar correction mechanism can be implemented in the framer block or within the payload pipeline before stub extraction. Here, data would be buffered in a shift register with adjustable tap points for each e-link to set the delay. However, such corrections cannot be made during normal operation, as detecting a misalignment requires a known, fixed pattern sent by the modules, only possible during the calibration phase before data collection begins. Inter-link Misalignment instead happens when data from two independent modules arrives at the FPGA at different times. This can be due to the varying lengths of optical fibers used in the Tracker and the finite speed of light. The discrepancies in arrival times can span multiple clock cycles at the FPGA. Correction methods include minor adjustments at the module level by adding a delay to the data sent, limited to a maximum of 25 ns (or one bunch crossing). For larger time differences, corrections must be performed in the DTC system. This involves buffering certain links to synchronize the data presentation on the same clock cycle as the link with the highest latency.

After data is processed by the framer, it moves to the link extractor. The extractor's role, as previously mentioned, is to identify and extract stubs. Unlike header identification, which relies on recognizing specific patterns and consistent values, stub extraction needs a flexible approach due to the variable number of stubs in a packet. As the data arrives, words containing stub information are progressively merged. This merging forms a bit vector, which grows in size until it contains sufficient bits to form an entire stub. When the bit vector reaches this threshold (18

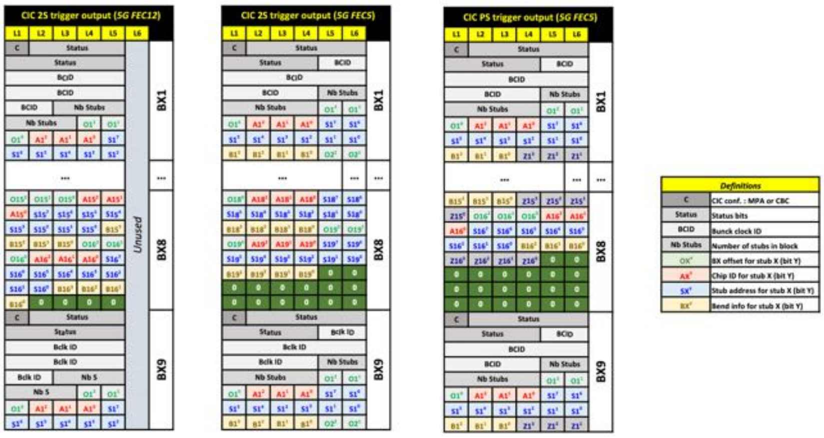

Fig. 4.17: CIC output trigger data format for 2S modules for FEC12 (left), FEC5 (middle) and PS modules (right) [57].

bits for 2S modules and 21 for PS modules, as visible from Fig 4.17), the complete stub is extracted. Following the extraction, the size of the bit vector is decreased by the length of the extracted stub. An additional step is needed though, as stubs from different CICs are decoded independently but the final part of the firmware expects a single stub stream for each module.

Next, the process of stub formatting is carried out. This involves transforming stub coordinates from local to global positioning. The key to this conversion is the use of the link index from which a stub originates. This index serves as an address in a lookup table, which holds the central positions of each module linked to the specific DTC unit. To pinpoint the exact hit location, the local position of the hit is added to this central position.

The last part of the DTC trigger path stems from the inherent design of the track trigger system. This system's architecture involves several cards processing individual events simultaneously. Consequently, there's a need to transition stubs from a spatial division, resulting from multiple input links, to a division based on their bunch crossing. To achieve this transformation, a specific logic block has been implemented in the DTC FPGA. This block operates akin to a systolic array, primarily composed of First In First Out (FIFO) elements. A systolic array is characterized as a networked two-dimensional grid of processing units, with each unit assigned to execute straightforward tasks. The router includes two arrays, each with 36 rows and 18 columns. This arrangement maximizes the FPGA's capabilities, ensuring efficient and effective processing of the high volumes of data generated.

4.2.2.2 DAQ path

Upon receiving a Level 1 Accept (L1A) signal, the DTCs convey the L1A information to connected modules. These modules, in response, transmit the hit data from the relevant bunch crossing via a dedicated L1A route back to the DTC, called the DAQ path [58]. This process involves a unique e-link from the CIC to the lpGbt designated for the L1A upstream data path. The DTC links to a DAQ and TCDS Hub (DTH) card, located within the same crate, which facilitates the transfer of event data to the HLT farm at Point 5. Each DTC has four 25 Gbps optical output links to the DTH. Consequently, the data from the modules is gathered in a large buffer before transmission via these links. The bandwidth of this path is notably lesser than that of the trigger path, and thus, the FPGA logic dedicated to this path is comparatively smaller.

The primary objective of the DAQ path block is to amalgamate FE data and ease their transmission: it's designed to be versatile and modular, capable of handling various event data types and channel configurations. The DAQ path firmware's structure revolves around a central Finite State Machine (FSM) that oversees a token ring chain of channel blocks, each corresponding to an input channel. This FSM initiates the channel readout sequence once all input buffers, containing data for DAQ transmission, are filled. Each channel block has a dedicated FSM for buffer readout and a multiplexing logic for data selection and propagation through the chain, leading to the merging of channel data into packets for the 25 Gb/s output link. The DAQ path system's design is both modular and parametric, allowing each module to cater to a specific number of input channels and adjust the width of the data words. The pipelined structure of the channel chain is crucial for meeting timing requirements, given the high number of input channels and their distribution across the FPGA's floor-plan.

The initial version of the DAQ path firmware has undergone functional simulations and hardware tests, confirming its operational viability. A simplified version schematic with 4 input channels is schematized in Fig 4.18.

Previously to the implementation of the DAQ path, whilst it was possible to set up registers in every chip on a module, it wasn't possible to fully measure and calibrate one with the DTC alone, obtaining pedestals and noise measurements, leading to the necessity to calibrate the module with an FC7, then exporting the calibration files to use them inside with the Serenity. This was due to the fact that, in order to obtain the S-curve mentioned in Sec. 4.1.2, readout of the full module was necessary, whilst only up to six stubs per chip (MPA or CBC) are possible through the trigger path. While in 2S modules full readout and decoding of the L1 data is necessary for calibration, as it's done in unsparsified mode, for PS modules only decoding of the header is necessary, as the sparsification is already performed by the MPA and gives the number of hits in each pixel/strip. The software to control and implement the DAQ path firmware in the daq software for the DTC has recently been implemented. This work included both additions of the possibility to control specific DAQ path's registers and identification and decoding of 2S modules' unsparsified data, which differs from the output received from the FC7 readout mainly due to headers and metadata changes. This implementation saw a lot of usage on 2S modules during the CMS-MUonE joined test beams that have been performed in the last two years. Whilst the software has been ported also for PS modules and the DAQ path firmware is in principle agnostic concerning the input data format, testing about this feature is still ongoing.

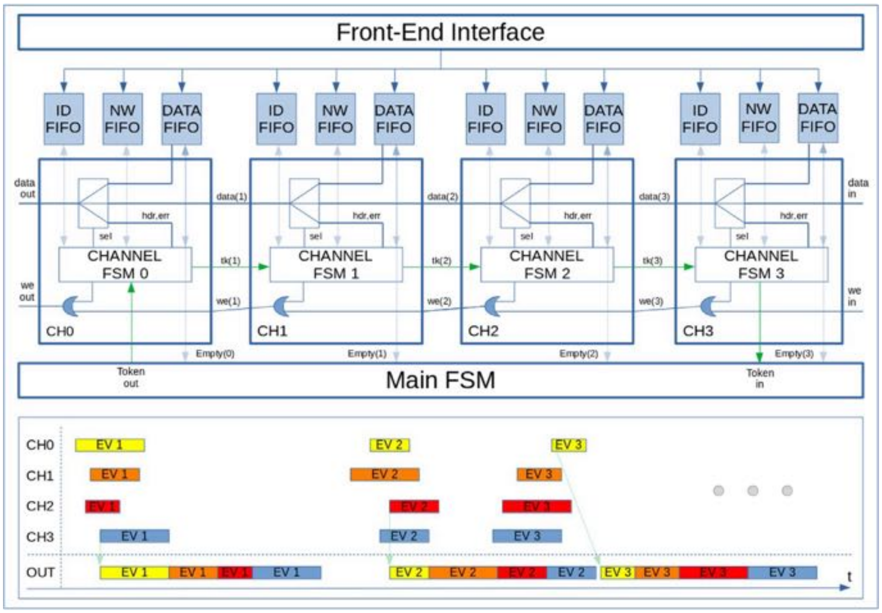

Fig. 4.18: Daq path firmware architecture and data timing. ID FIFO stores the ID information, NW FIFO the number of words and DATA FIFO the data words of incoming event [58].

5 MUonE experiment

MUonE experiment [59], for which the experimental proposal is being written right now, seeks to precisely measure the angle of elastic scattering between electrons and muons, aiming for a large amount of statistics. MUonE has a direct link with the CMS OT upgrade: the chosen building blocks for the proposal, at the moment, are the 2S modules from the CMS OT upgrade. This symbiosis allows both MUonE to use cutting-edge technology without the need to develop it, and CMS to test both modules and the DAQ chain, minimizing the personpower needed thanks to MUonE collaboration's help.

The muon magnetic anomaly, defined as $\alpha_\mu = (g_\mu - 2)/2$, where g_μ is the muon gyromagnetic ratio, represents one of the most interesting observable of the SM: an experiment vs theory discrepancy persists since more than 20 years. The latest result from Muon g-2 collaboration [60] gathered new attention on the topic, showing results in agreement with previous experiments and with 5σ discrepancy to theoretical predictions. Comparison with predictions, though, is limited by the knowledge of the hadronic leading order contribution (a_μ^{HLO}) to the muon g-2, which cannot be computed perturbatively given the inclusion of low energy Quantum Chromodynamics (QCD) contributions. The MUonE experiment proposes to determine a_μ^{HLO} with a novel approach [61] [62] based on direct measurement of the hadronic contributions to the electromagnetic constant ($\Delta\alpha_{had}$) in the space-like region.

In this chapter we'll first delve into the physics problem of the measurement of the magnetic moment anomaly for the muon and then proceed to describe the structure of the foreseen experiment, trying to highlight its strengths and weak points.

5.1 The muon anomaly

The study of the magnetic properties of elementary particles, particularly the magnetic anomaly of the muon, has been a pivotal aspect of high-energy physics research. The magnetic dipole moment $\vec{\mu}$ of a particle is a fundamental characteristic that determines its interaction with external magnetic fields. For a classical system, this interaction is described by the potential energy $U = -\vec{\mu} \cdot \vec{B}$ and the torque $\vec{\tau} = \vec{\mu} \times \vec{B}$, where $\vec{B}$ is the magnetic field. The magnetic moment of a particle with charge e and mass m orbiting in a magnetic field with velocity v in a circular trajectory of radius r is given by $\mu = \frac{evr}{2}$, linking it to the particle's angular momentum $L = mvr$ and allowing us to express it as:

$$\vec{\mu} = g_l \frac{e}{2m} \vec{L} \tag{5.1}$$

where the Landé factor g_l, equal to 1 for a classic system, has been introduced. The addition of the concept of intrinsic spin angular moment, $\vec{S}$, leads to the definition of the intrinsic magnetic moment of a particle from Eq. 5.1 as:

$$\vec{\mu}_S = g \frac{e}{2m} \vec{S} \tag{5.2}$$

Where g is called the gyromagnetic ratio and is analogous to the Landé factor. Dirac's equation refines this understanding by incorporating quantum mechanical principles, leading to the realization that for particles like the electron and muon, the gyromagnetic ratio g is exactly 2. Nonetheless, experimental measurements of the so-called electron magnetic anomaly, defined as

$$a_e \equiv \frac{g_e - 2}{2} \tag{5.3}$$

lead to slight deviations from the value calculated by Dirac already in 1948 [63]. Refinements of the theory were presented in that same year by Schwinger [64], explaining the deviations in terms of a structureless electron interacting with virtual particles that arise from vacuum fluctuations. Experimental and theoretical values for the electron anomaly latest measurements [65] are in agreement to a level of 1×10^{-12}, with discrepancies ranging from 3.9σ to 2.1σ to the Standard Model predicted value, based on different measurements of the fine structure constant [66] [67]. This shows concrete proof of the validity of Quantum Electrodynamics (QED) theories. Nonetheless, the contribution of heavier particles modifying the anomalous magnetic moment of a lepton a_l goes as:

$$\frac{\delta a_l}{a_l} = (\frac{m_l}{M})^2 \tag{5.4}$$

where m_l is the mass of the lepton and M is the mass of the heavier particle. This makes heavier leptons much more sensible to possible new high-mass BSM particles and, in general, a more robust test for new physics. Measurement of τ lepton magnetic anomaly, though, is not possible at the moment for both its short lifetime and the amount of different particles in which it can decay, making the muon the best candidate to investigate this field.

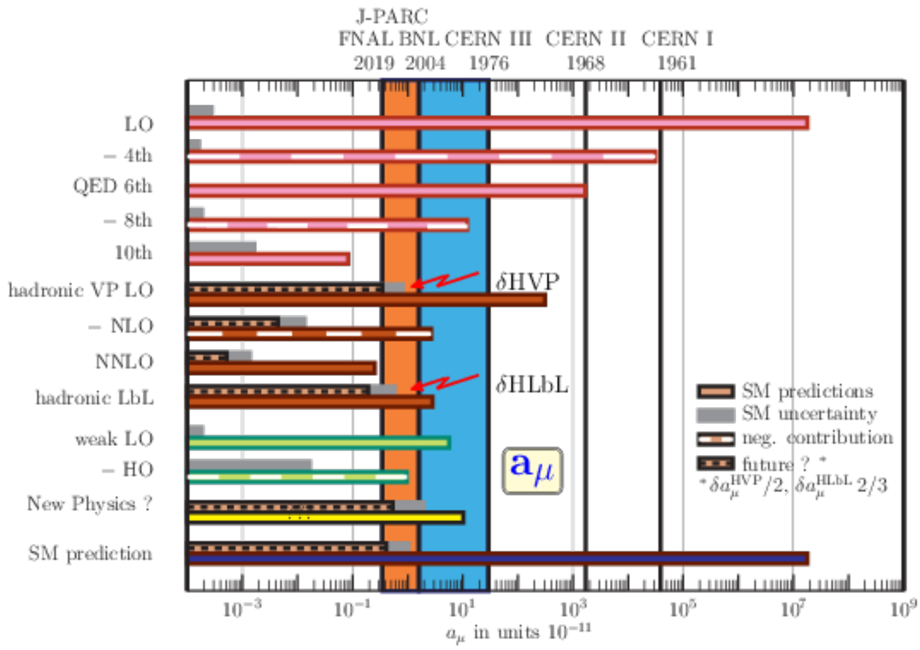

Fig. 5.1: Past and future g-2 experiments testing various contributions [68].

Concentrating on the muon anomaly now, it's possible to write the Standard Model prediction as the sum of a QED, and EWK and a QCD term contribution:

$$a_\mu^{SM} = a_\mu^{QED} + a_\mu^{EWK} + a_\mu^{QCD} \tag{5.5}$$

The different contributions and their uncertainty are visible in Fig. 5.1. The first two contributions, the QED and EWK ones, can be calculated via a perturbative approach with high precision. The QED term can be expressed in a series of the fine structure constant, leading to the most recent values calculated as [69] [70]

$$a_\mu^{QED} = 11658471.8931(104) \times 10^{-10} \tag{5.6}$$

using the fine structure constant measurement from Cs atom oscillations [66].

EWK term is suppressed by the squared ratio of the muon and W boson mass with respect to the pure QED term, and two loop contributions with hadrons are non-negligible. These are treated with dispersive relation or specific hadron models, representing the main source of uncertainty on the total EWK contribution, which is calculated as:

$$a_\mu^{EWK} = (15.36 \pm 0.10) \times 10^{-10} \tag{5.7}$$

The remaining contribution, the hadronic one, is, as visible in Fig. 5.1, the one with the driving uncertainty for the measure taken into account, making the primary challenge for the muon anomaly prediction in accurately accounting for hadronic contributions. These contributions, particularly from hadronic vacuum polarization and light-by-light scattering, are the main sources of uncertainty in the Standard Model predictions. Efforts to refine these predictions will be described in the next paragraph.

5.1.0.1 Hadronic contribution to the muon g-2

The theoretical framework addressing the hadronic contribution to the muon magnetic anomaly diverges markedly from the methods used for QED and EWK contributions due to its non-perturbative nature. This divergence is due to the dominance of strong interactions at low energies, where QCD precludes the effective use of perturbation theory. Central to this framework is the leading hadronic effect, a_μ^{HLO}, arising from a vacuum polarization insertion in the virtual photon line of the Schwinger term diagram, as show in the Feynman diagram in Fig. 5.2.

Fig. 5.2: Hadronic leading order contribution to the muon anomaly [71].

To compute a_μ^{HLO}, the dispersive approach is historically employed, utilizing a dispersion integral based on the principles of causality and unitarity in quantum field theory. This approach integrates the hadronic vacuum polarization function and a kernel function, with the latter approximating as $1/s$. The integral's formulation is further informed by the optical theorem, linking the imaginary part of the hadronic vacuum polarization function to the e^+e^- annihilation cross-section into hadrons. The leading hadronic contribution to the muon anomaly is thus derived from integrating the product of the kernel function and the hadronic ratio $R(s)$, based on experimental data from e^+e^- colliders. This leads to:

$$a_\mu^{\text{HLO}} = \frac{\alpha}{\pi} \int_0^\infty \frac{ds}{\pi} \operatorname{Im} \Pi_{had}(s) \frac{K(s)}{s} \tag{5.8}$$

with:
$$K(s) = \int_0^1 dx \frac{x^2(1-x)}{x^2+(1-x)s/m_\mu^2} \tag{5.9}$$
and:
$$\operatorname{Im}\Pi_{\text{had}}(s) = \frac{\sigma\left(e^+e^- \rightarrow \text{ hadrons }\right)}{4\pi\alpha/s} = \frac{\alpha}{3}R(s), \quad R(s) = \frac{\sigma\left(e^+e^- \rightarrow \text{ hadrons }\right)}{\sigma\left(e^+e^- \rightarrow \mu^+\mu^-\right)} \tag{5.10}$$
Experimental measurements for this purpose are used up to a certain energy threshold, above which perturbative QCD becomes applicable, typically beyond the open $b\bar{b}$ threshold. These measurements, obtained through methods like direct scan and radiative return, are crucial for determining $R(s)$ but also introduce complexities, especially in managing systematic uncertainties and integrating data from different experiments.

In the last years though, a different approach has been attempted by the BMW collaboration for the calculation of a_μ^{HLO} based on lattice QCD, reaching precisions compatible with the dispersion integral only in 2021 [72]. While the dispersive approach relies on experimental data from e^+e^- collisions and a dispersion integral to compute the hadronic contribution, lattice QCD offers a more fundamental, theoretical method. In lattice QCD, calculations are based on simulating the two-point correlator of the electromagnetic current on a discretized spacetime lattice, thereby directly accounting for QCD effects. This approach is computationally intensive and faces challenges such as managing systematic errors due to continuum and volume extrapolations. The contrast between these two methodologies lies in their foundational principles: the dispersive approach is rooted in experimental data and phenomenological analysis, while lattice QCD is grounded in the direct numerical evaluation of QCD. Despite their differences, both approaches aim to refine our understanding of the hadronic contribution to the muon magnetic anomaly, each offering unique insights and facing distinct challenges. The calculation from BMW collaboration and the ones obtained via dispersive approach, though, as visible in Fig. 5.3 are not compatible, leading to tension in the theoretical calculations. This tension is reflected in different discrepancies in g_μ experimental values with respect to the theoretical ones, depending on the calculation of a_μ^{HLO}, which will be treated in Sec. 5.1.1.

5.1.1 Experimental measurements of the muon g-2

The foundational concept for measuring the anomalous magnetic moment (g-2) of the muon involves assessing the spin precession of a muon within a magnetic field. When placed in such a field, a muon exhibits two distinct rotational movements.

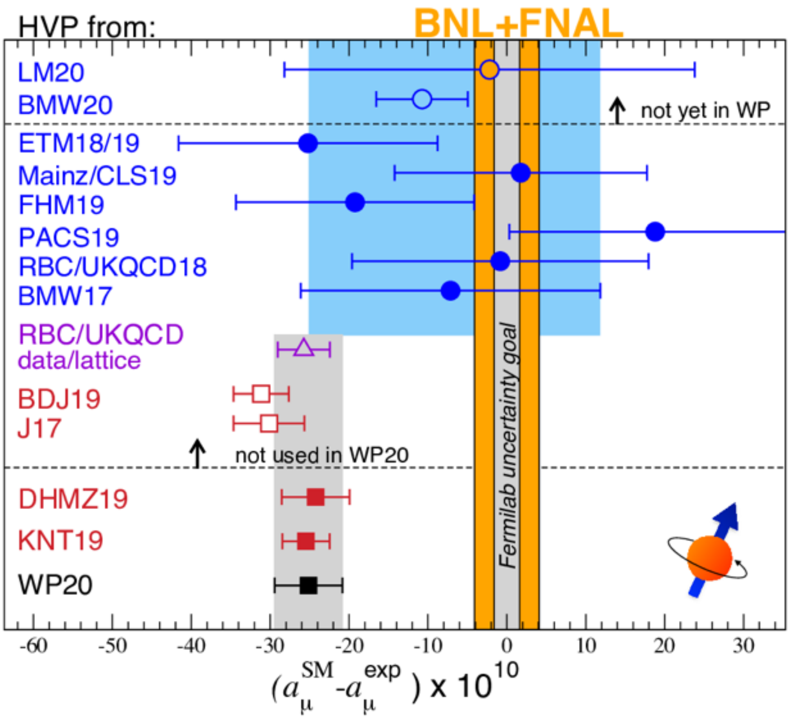

Fig. 5.3: Comparison of theoretical predictions of a_μ with the current experimental value (orange band). Red squares represent dispersive results. Blue circles are lattice results. The purple triangle results from a hybrid approach of the two methods. Figure from [73].

The first is Larmor precession, which arises from the interaction between the muon's spin and the magnetic field, described by the frequency equation:

$$\vec{\omega}_s = g\frac{e\vec{B}}{2m_\mu} + (1-\gamma)\frac{e\vec{B}}{\gamma m_\mu} \tag{5.11}$$

The second rotational movement is characterized by the cyclotron frequency, defined as:

$$\vec{\omega}_c = \frac{e\vec{B}}{\gamma m_\mu} \tag{5.12}$$

In an ideal scenario where g=2, these two frequencies would coincide, resulting in a constant spin orientation relative to the muon's direction. However, the existence of the muon anomaly causes the precession to occur $(1 + a_\mu)$ times faster than the rotation, yielding the anomalous precession frequency ω_a:

$$\vec{\omega}_a = \vec{\omega}_s - \vec{\omega}_c = \frac{e\vec{B}}{m_\mu}\left(\frac{g}{2} - 1\right) = a_\mu \frac{e\vec{B}}{m_\mu} \tag{5.13}$$

Thus, with precise knowledge of the magnetic field, the muon anomaly can be accurately deduced. However, an essential aspect of this process is the measurement of the muon spin polarization. This begins with the generation of a beam of polarized muons, typically achieved through the decay of charged pions. In the decay process $\pi^+ \rightarrow \mu^+ \nu_\mu$, with the assumption of massless neutrinos, the muon neutrino is a left-handed helicity eigenstate. Consequently, due to angular momentum conservation and the pseudoscalar nature of the pion, the emitted muon also exhibits left-handed helicity, resulting in a spin-polarized muon beam. The subsequent step involves measuring this spin polarization.

This measurement is achieved by analyzing the polarization of positrons resulting from muon decay. In the muon's rest frame, the highest energy positrons are emitted when both neutrinos are directed opposite to the positron, with the positron carrying half the total energy and the neutrinos sharing the remainder. As neutrinos are helicity eigenstates, the antineutrino is right-handed and the neutrino left-handed. Due to angular momentum conservation, positrons in this scenario inherit the spin of the parent muon. Moreover, the V-A nature of the weak decay favors coupling to right-handed positrons, leading to the emission of high-energy positrons in the same direction as their spin. Consequently, in the laboratory frame, the muon polarization can be inferred from the temporal distribution of detected positrons.

This methodology has been successfully employed in various experiments, starting with three experiments at CERN between 1961 and 1977 [74] [75], followed by E821 at BNL [76] and the more recent E989 at Fermilab, whose results in 2021 [77] and 2023 [60] have reignited interest in the field. The results from BNL and Fermilab are shown in Fig. 5.4 left. The right plot on the same figure shows discrepancies between measurements and theoretical prediction, with both lattice and dispersive approaches. Notably, the BMW estimate suggests near compatibility between the measurements and the Standard Model prediction. In this context, the MUonE experiment has been proposed to provide a direct measurement of a_μ^{had}.

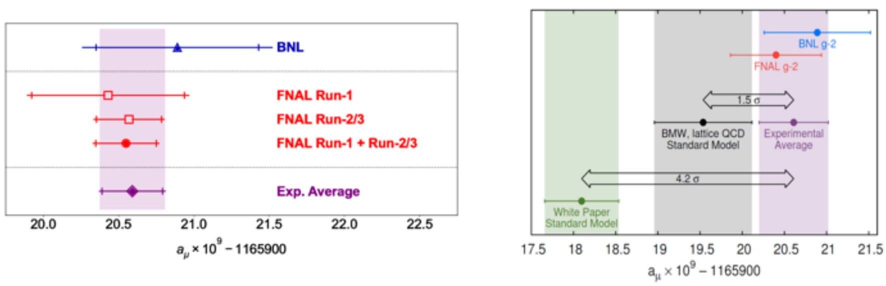

Fig. 5.4: (left) experimental results from Run-1 and Run-2 for Fermilab g-2 experiment [60] and experimental average with the previous BNL results. (right) Comparison of results obtained until the 2021 paper from Fermilab g-2 collaboration [77] and the two different predicted standard model values for the muon anomaly given lattice of dispersive calculation of the hadronic contribution.

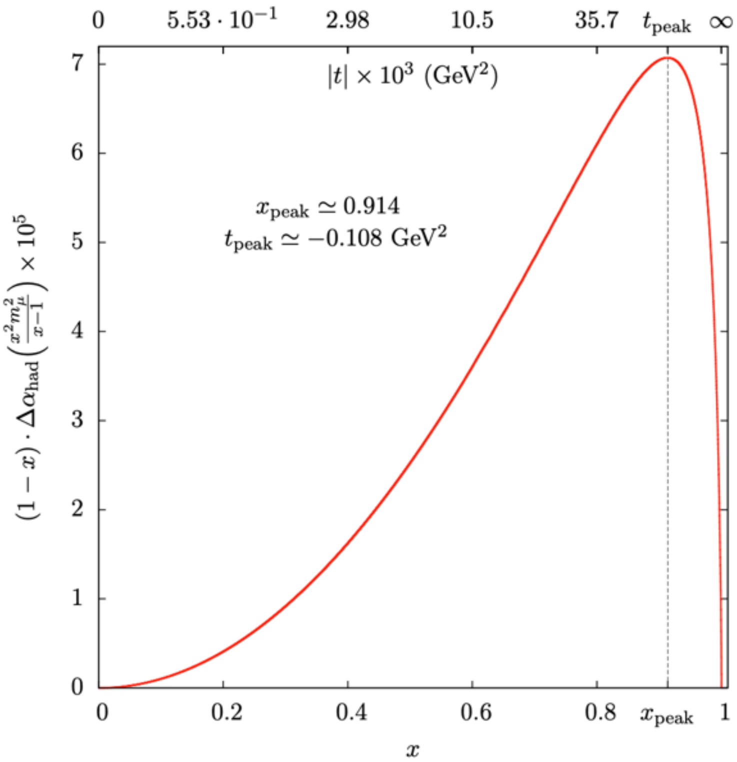

Fig. 5.5: Eq. 5.14 integrated $\times 10^5$ as function of both t and x.

5.2 Theoretical framework for a_μ^{had} measurement in MUonE experiment

As described previously in Sec. 5.1.0.1, the historical approach to a_μ^{HLO} calculation has been via Eq. 5.8. The presence in the integrand of $R(s)$, containing the cross-section of $e^+e^- \rightarrow hadrons$, though, is the root of major difficulties in this calculation: the integrand suffers from high fluctuation at low energy due to hadronic resonances and threshold effects, leading to the use of both experimental values of $R(s)$ up to a certain value and then perturbative QCD calculations. The MUonE experiment proposes a new way of dealing with this issue [61] [62] [59]. Switching from the time-like approach to a space-like approach it's possible to obtain [78] [79]:

$$a_\mu^{\text{HLO}} = \frac{\alpha}{\pi} \int_0^1 dx(1-x)\Delta\alpha_{\text{had}}[t(x)] \tag{5.14}$$

where $\Delta\alpha_{had}(t)$ is the hadronic contribution to the running of the fine structure constant at:

$$t(x) = \frac{x^2 m_\mu^2}{x-1} < 0, \tag{5.15}$$

the space-like squared four-momentum transfer, where x is the fraction of transferred momentum. Given that the leptonic contribution to $\Delta\alpha$ can be calculated via perturbation theory and is known up to three loops in QED [80] and four loops in specific q^2 limits [81] [82] [83], this approach enables the extraction of $\Delta\alpha_{had}$ from a $\Delta\alpha$ measurement, resulting in a smoother integration in Eq.5.14, as shown in Fig. 5.5. An alternative method to compute the total value of a_μ^{HLO}, which is less dependent on the adopted parametrization, has been recently proposed [84].

The MUonE experiment aims at extracting $\Delta\alpha_{had}$ from the measurement of the differential cross-section of the $\mu^+e^- \rightarrow \mu^+e^-$ elastic scattering [59], using an $E_\mu = 150$ GeV muon beam on the atomic electrons of a fixed target. The proposed material for the target is, at the present time, Beryllium, but the choice is not final, and different materials are under study.

As a pure t-channel process, this method allows for unambiguous identification of momentum transfer. Additionally, it enables the matching of electron energy with its scattering angle and the correlation of scattering angles between the two particles, as shown in Fig.5.6. This helps significantly in better background rejection. Another important feature is that for an incident muon beam of $E_\mu = 150$ GeV, it's possible to inspect up to a transferred momentum $x \simeq 0.93$, whereas the peak for Eq. 5.14 is at $x_{peak} \simeq 0.914$, reaching an 88% coverage of the curve with the available 150 GeV muon beam at M2 beam line at CERN [85]. The boosted kinematic of the process also helps in the detector design, making it possible to use a single straight detector to cover the whole acceptance.

MUonE aims to determine a_μ^{HLO} with a statistical uncertainty of $\simeq 0.3\%$ and comparable systematic, to reach a competitive level with the latest lattice results.

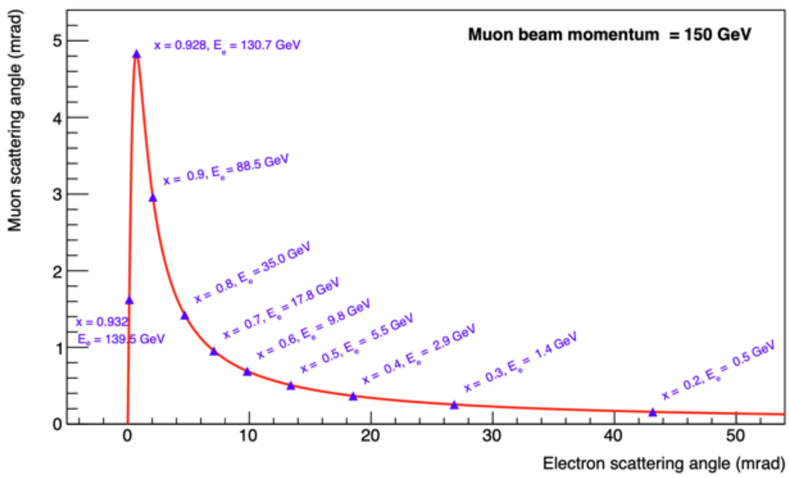

Fig. 5.6: Relation of muon and electron scattering angles for 150 GeV incident muon beam.

5.3 MUonE experimental setup

The proposed experiment [62] consists of 40 identical tracking stations, which will be described in depth in Sec. 5.3.1. The stations are modular, self-contained elements, providing everything necessary for generating and tracking an elastic event. At the end of the 40 stations, as visible in the schematic in Fig. 5.7, will be placed an ECAL and a muon chamber, to perform partial particle identification, in the region covered by the geometrical acceptance.

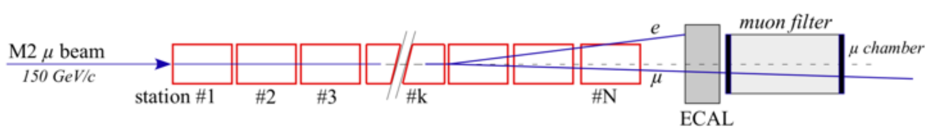

Fig. 5.7: Schematic view of MUonE experimental apparatus.

5.3.1 Tracking station

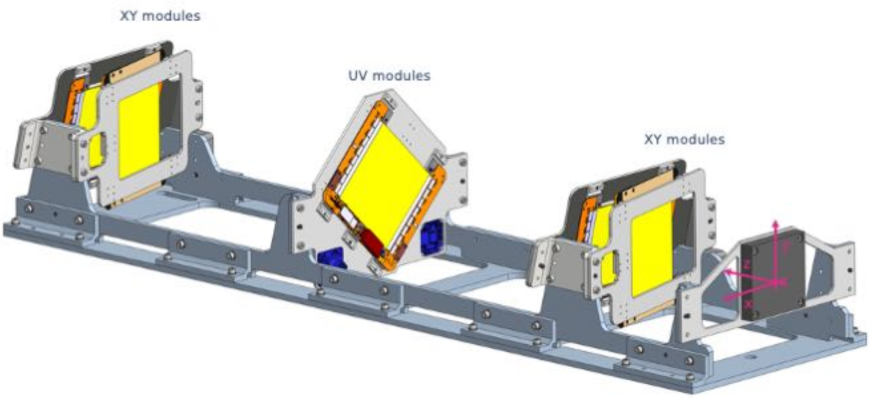

Fig. 5.8: CAD drawing of a MUonE station. The reference system is shown, the beam follows the z direction.

Each station, a scheme of which is visible in Fig. 5.8, features a 1.5 cm thick Beryllium target, followed by the tracking system of lever arm ≈ 1 m, composed of 6 CMS Phase-2 2S modules, which have been thoughtfully described in Sec. 3.3, arranged in 3 planes. The central modules in a station will be rotated of 45 degrees around the beam direction, allowing for track disambiguation, and define the so-called "UV" plane. The first and third pairs of modules are tilted by 233 mrad to enhance single-hit resolution. The whole setup will be mounted on three stepper motors, allowing for fine alignment of the tracking station with the beam.

The mechanical structure is designed to be able to achieve the stringent constraints for systematic uncertainties, ensuring precise control over longitudinal distances. It's constructed of Invar, an alloy comprising 64% Iron and 36% Nickel: its very low thermal expansion coefficient (approximately $1.2 \times 10^{-6} K^{-1}$), would keep the expansion under 10 μm for variations up to ± 8 °C.

Each station will be separately enclosed in a controlled environment, where fluxed dry air will be circulated to protect the silicon sensors from high humidity. A cooling system will also circulate distilled water at 18 °C to remove heat from front-end electronics. Additionally, a laser holographic system is being developed to actively monitor relative displacements and deformations in the mechanical structure with sub-micrometer accuracy.

5.3.1.1 Data acquisition

Regarding the previewed DAQ for the MUonE experiment, it also shares similarities with the CMS readout. Modules will be read out by the Serenity board, in a quite similar fashion as explained for the OT in Sec. 4.2.1. The main difference is that MUonE will only exploit the trigger path, reading out stubs at 40 MHz. Assuming the nominal maximum beam intensity of $2{\times}10^{8}$ muons per spill, so in bunches every $\sim$ 5s, the encoding of stub in 16 bits, a 32-bit header per module, and an expected rate of 3 stubs per 25 ns clock cycle per module, the average data rate is calculated to be around 20 Gb/s per station. This results in each Serenity card handling an average data output of approximately 240 Gb/s.

For the full MUonE experimental setup (40 stations) the data throughput will be too high to allow storage, introducing the need for data reduction. A two-layer process could be implemented, where a first layer of Serenity would collect the events, whereas a second layer, also composed of Serenity cards, handles event building and selection. This layer reads in data at a high rate (less than 1 Tb/s) and implements event filtering to significantly reduce the event rate from 40 MHz to less than 400 kHz. After event filtering, the uncompressed output data rate is expected to be less than 10 Gb/s per station. This second layer of processing also includes various options for data transfer to storage servers, such as Ethernet 1G/10G and PCIe Gen3 connections.

5.3.1.2 Online track reconstruction and trigger

An online track selection will be necessary to reduce the rate, given the previewed 40 MHz triggerless readout. Even though it has still not been possible to implement it or test it up to now, an overview of a possible three-stage process foreseen for the final experiment will be described here. The previewed online tracking will follow the subsequent steps:

1. **Candidate selection**: X and Y axes can be considered independently for the initial selection. A track can be formed of three hits: one at the start of the station, one at the end, and one at the middle, all obtained by the combination of the two planes. A candidate set of hits can be created by propagating the straight line from outer planes to the middle sensors and searching for compatible hits: the acceptance window can be tuned to maximize efficiency at a given occupancy. This process, shown in 5.9, should provide a 10% reduction rate and deals with the impossibility of fitting all the hits combinations, which increase exponentially.

2. **Track fitting**: a possibility to implement the track fitting is via a least square fit implemented with HLS [86], a tool for translation of C++ code into VHDL. This would enable extrapolation of track parameters and associated errors on 2D tracks: 2D tracks sharing middle plane hits will be merged in a 3D track.

3. **Selection**: Once the tracking has been performed, different possibilities are available for online event selection. The most straightforward option would be the use of a vertex constraint, combining different tracks: this should offer $\approx 6\times$ reduction in data rate.

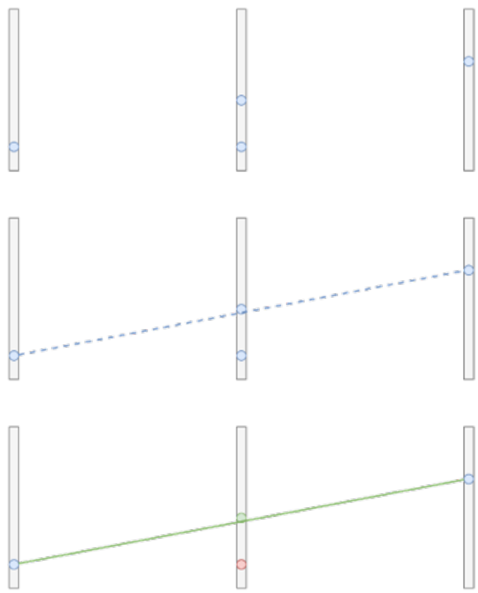

Fig. 5.9: Scheme of the candidate selection for track fitting. The track is initially performed using the first and last modules in a station and drawing a straight line. Hits in the UV modules are then associated to the straight line, based on distance between the candidate track. [87]

5.3.2 ECAL

The ECAL also plays a role for both Particle Identification (PID) and as a redundant check against the tracker system's findings by measuring the electron energy. This measurement is important for the evaluation of systematic effects and to correctly identify background processes. Moreover, event selection is facilitated by the ECAL, such as identifying instances where the energy deposition exceeds a specific threshold or detecting dual showers (electron plus gamma-ray).

The proposed ECAL structure, positioned downstream of all tracker stations, consists of lead tungstate (PbWO4) crystals matrix, mirroring those utilized in the CMS electromagnetic calorimeter [88]. These crystals, having dimensions of 2.5$\times$2.5 cm^2 and a length of 23 cm (26 radiation lengths), are coupled with avalanche photodiodes for readout. Lead tungstate is chosen for its rapid scintillation emission time, effective light yield, and compactness. The tracker system, spanning approximately 40 meters and incorporating passive materials, imposes constraints on the ECAL's coverage, limiting its transverse dimension and, consequently, its full acceptance. The previewed ECAL will be of the order of 1×1 m^2, allowing for measurement of the electron where it's more ambiguous, so for an angle of the electron with respect to the beam direction $\Theta_e < 5$ mrad. This dimension will ensure full containment for electrons with energy E > 30 GeV, while angular acceptance is for E > 10 GeV.

6 CMS - MUonE test run

Following three years of joint MUonE-CMS test beams, with the aim of both characterizing 2S modules, testing the final CMS DAQ chain, and probing the feasibility of MUonE experiment, a test run for MUonE has been performed at the M2 beamline from August 21^{st} to September 10^{th} 2023.

This chapter covers the results obtained for this test run, starting from the description of the whole experimental setup and DAQ chain, highlighting the differences between MUonE chain and what will be the final CMS DAQ chain. After that, the results of a preliminary data analysis will be shown, with the aim of reconstructing physical events, characterizing the modules, and proving the goodness of the acquisition chain.

6.1 Experimental setup

The detector in this configuration was composed of two fully equipped MUonE stations, as described in Sec. 5.3.1. The first one, without a target, was used to detect the incoming muons, while the second, with a target installed, was meant to fully reconstruct tracks and vertexes. The mechanical structure, where the 2S modules are mounted, is equipped with cooling pipes connected to an Arctic AC200 A45HC chiller, fluxing water at 18 ± 0.5 °C, which is meant to keep the structure at a constant temperature to avoid sensor displacement due to thermal effects. Also, dry air was fluxed in the stations to keep the relative humidity below 3%, to avoid an increase in the leakage current and electrical breakdown in the modules. Both stations were enclosed in a ventilated tent to maximize environmental stability. In Fig. 6.1 a picture of the two instrumented stations is shown while in Fig. 6.2 there is a schematic of the arrangement of the 12 2S modules used. In Fig. 6.2 it's also possible to see the global reference frame used for the whole test beam: a right-handed reference frame, with the z direction parallel to the beam direction and the y-axis pointing upward. Two targets were available for this test run, both were made of carbon graphite but with different thicknesses, 2 cm and 3 cm. The setup was completed by an electromagnetic calorimeter, placed downstream of the two stations.

Fig. 6.1: Picture of the 2023 test beam setup. The arrow indicates the beam direction.

The stations were instrumented with seven temperature sensors: six of them were clipped on the frames, to get the nearest possible temperature to the modules and one was kept floating inside the station to monitor the air temperature. Additionally, a humidity sensor was placed inside the station, to offer a complete overview of the environmental conditions in the station. Modules for the OT upgrade include also two thermistors, one directly installed in the lpGbt and one on the sensor itself. This way, the modules themselves will provide temperature measurements, avoiding the installation of other sensors in the Phase-2 tracker. The readout of the thermistor installed on the module was integrated into the software used with the Serenity board, adding another temperature point per module, much nearer to the sensor itself. Two additional temperatures were monitored, the one of the water pumped from the chiller, and the one inside the tent.

Both modules inside the station and the ECAL were powered via a CAEN SY4527 power supply [89]. Two modules were used, the one providing the high voltage needed to bias the silicon sensor being an A7435SN [90] module, and the one providing low voltage for front-end electronics being an A2519C module [91]. 2S modules were powered with a bias voltage between -300 and -400 V, depending on the module, to keep leakage current under 15 μA to prevent damage to the silicon sensors. The voltage to power up the front-end electronics was set to 10.40 V for every module. The power supply, given the Application Programming Interface (API), made it possible to read out and check voltages and currents over all the installed modules.

Data have been acquired with different muon beam intensities up to 40 MHz muon rate inside the tracking station, with and without the target installed. Experimental

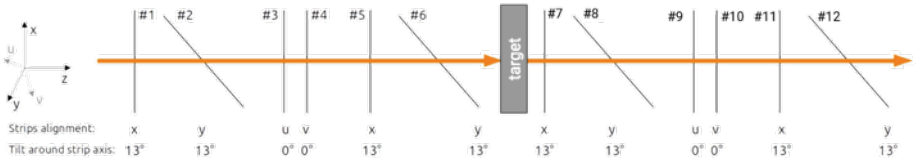

Fig. 6.2: Schematic drawing of the 2023 test beam 2S module setup.

Run	Date	Intensity	Particle	Target	Notes
0	03/09/23	Low	Muon	No	Vcth scan
1	31/08/23	Low	Muon	No	
2	03/09/23	Low	Muon	No	
3	03/09/23	Low	Muon	No	Vcth scan
4	04/09/23	High	Muon	No	Alignment run
5	04/09/23	High	Muon	3 cm	
6	04/09/23	High	Muon	3 cm	
7	04/09/23	High	Muon	3 cm	
8	05/09/23	No beam			
9	05/09/23	High	Muon	3 cm	
10	07/09/23	Low	Electron	No	
11	07/09/23	High	Muon	2 cm	
12	08/09/23	High	Muon	2 cm	
13	09/09/23	High	Muon	2 cm	
14	09/09/23	High	Muon	2 cm	
15	09/09/23	High	Muon	2 cm	
16	10/09/23	High	Muon	2 cm	
17	10/09/23	High	Muon	2 cm	ECAL test
18	11/09/23	High	Muon	2 cm	ECAL test
19		High	Muon	2 cm	ECAL test
20	12/09/23	Medium (10^8 $/mu/$spill)	Muon	2 cm	
21	12/09/23	Medium (10^8 $/mu/$spill)	Muon	2 cm	
22	12/09/23	Medium (10^8 $/mu/$spill)	Muon	2 cm	

Tab. 6.1: List of all the runs taken during 2023 test run.

operations initially started with a low beam intensity, without the target, to commission the configuration of the 2S modules, then the beam intensity was increased to the maximum available still without the target to check the stability of the DAQ system and for alignment studies. Finally, the 3 cm target was inserted and data was acquired with the maximum beam intensity to demonstrate the reconstruction of elastic scattering events. A list of all the runs taken during the 2023 test run is available in Tab. 6.1.

6.2 DAQ readout

Data ingestion has been handled by one Serenity card, which has been described in Sec. 4.2.1, and which is the foreseen card for the final DAQ system in MUonE and CMS. This made it possible to test the configuration and calibration of a large number of modules with the final board, impossible before due to the lack of modules and the availability of the software.

Once collected from the Serenity, data are transferred onward via 10 Gbps ethernet links to commercial PCs, as shown in Fig. 6.3, which consolidate and chunk the data before transfer to EOS for long-term storage and analysis. No local buffering is foreseen, and data are sent through a direct link to EOS from the experimental hall at 2 x 100 Gbps.

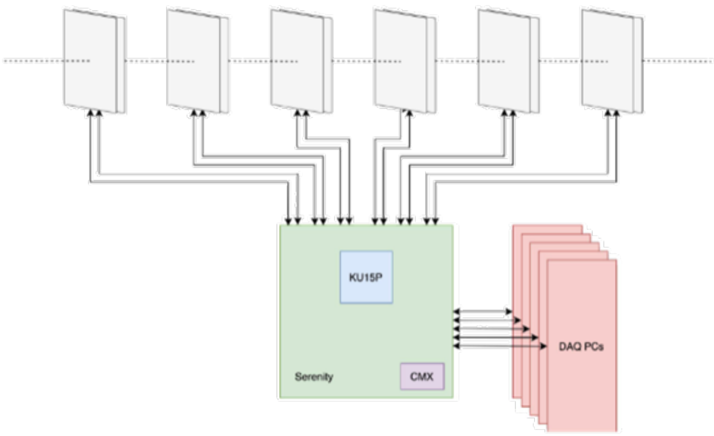

Fig. 6.3: Schematic of the data flow from the modules to the sink PC [87].

A complete overview of the DAQ rack, which was outside of the experimental area, connected to the station via 100 m optical fiber, is visible in Fig. 6.4. Aside from the Serenity, switch and pcs, two auxiliary FC7s were available in the setup. The FC7s were on one side a backup for the module's calibration and configuration, and on the other hand, provided a tested and secure way to verify that the calibration itself succeded correctly.

6.2.1 Processing firmware

MUonE data acquisition chain shows a number of similarities with the previewed one for CMS. Although MUonE experiment plans to acquire triggerless at 40 MHz stubs data and does not need to rate stubs based on their bend, some differences have to be taken into account and a different firmware has been deployed.

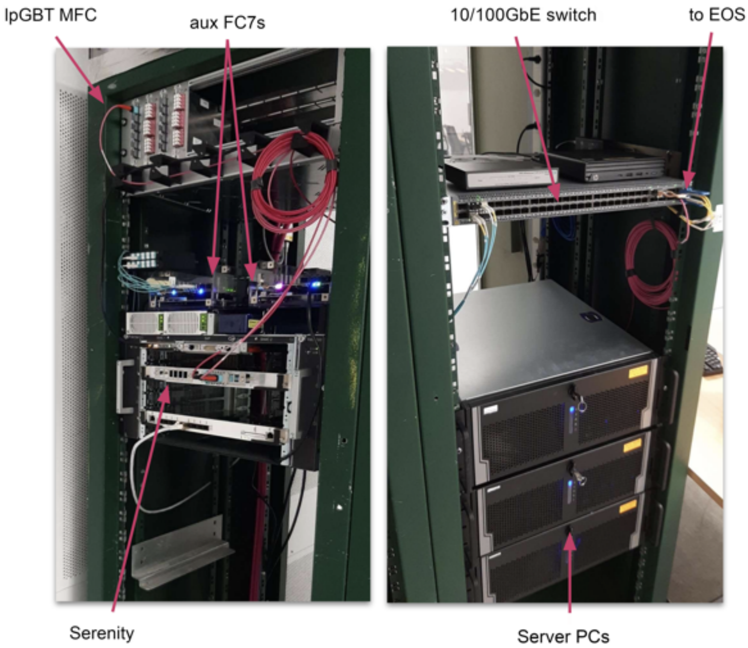

Fig. 6.4: Setup of the rack with Serenity board and connections to EOS.

The only trigger path, described in Sec. 4.2.2.1 is implemented, and each optical link streams data directly from a module to the link interface (Fig. 4.15), the only common firmware block to the CMS Phase-2 tracker.

The subsequent block, the link aggregator, a schematic of which is visible in Fig. 6.5, is custom for the MUonE experiment. It aggregates stubs across all links based on clock cycle using two-layer FIFOs to buffer data.

The stubs, now aggregated into single clock cycles, must be recombined into a single stream for transmission on an ethernet link. This function is provided by the link combiner block, shown in Fig. 6.6. Each clock cycle is sent sequentially and the output is buffered to account for fluctuations in the ethernet link rate. Also, a header with metadata is added to the stream before the stubs.

Communication and data stream from each station to the Serenity board are handled by different instances of the same firmware, so data packed in binary form are saved on disk in 1.2 GB data files for each station. Time-based merging from different stations is handled via software, during the decoding in human-readable form of the highly compressed binary data.

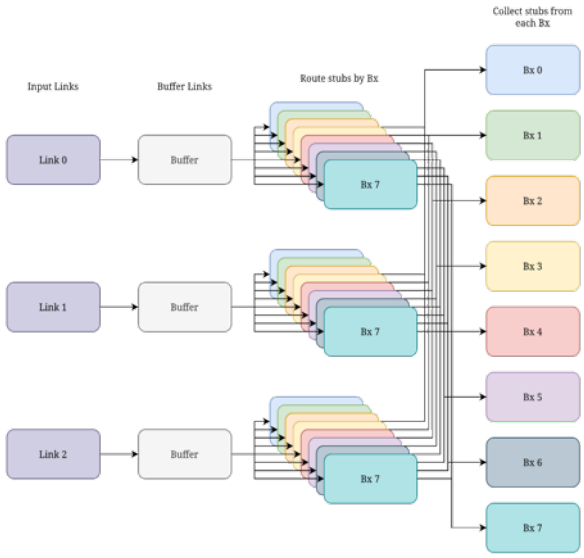

Fig. 6.5: Schematic of the link aggregator firmware block implemented on the Serenity board.

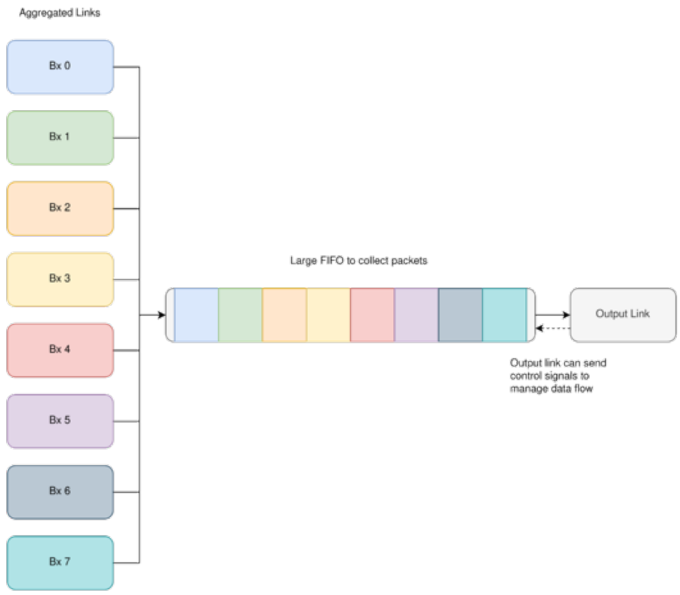

Fig. 6.6: Schematic of the link combiner firmware block implemented on the Serenity board.

6.3 Software

A set of software tools have been developed over the years, during the previous test beams and the test run, aiming for scalability and reusability for the actual experiment run. In the next paragraphs, the most important tools developed will be discussed.

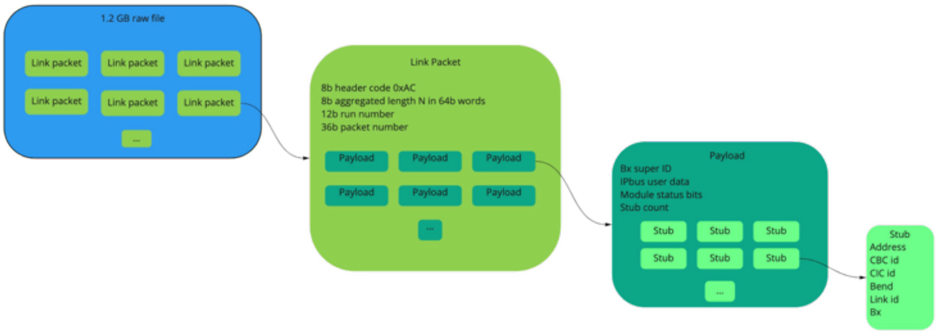

Fig. 6.7: Modular structure of the output files saved on disk from the Serenity [87].

6.3.1 Decoder and merger

The first tool that had to be developed was a decoder, to convert highly compressed binary information in a format easily accessible for analyzers. The input format, schematized in Fig. 6.7, is nested and modular. Each of the 1.2 GB files saved from the Serenity board contained so-called "Link Packets". This packet has a header, namely 0xAC, the number of 64b words contained in the packet, and the packet and run number. "Payload" packets are then identified inside the Link Packet, reading out words until the limit indicated in the Link Packet is reached. A payload contains coarse timing information (the so-called Bx Super Id, which matches the orbit counter previewed for the CMS experiment, so for every super id there are 3564 Bxs), the number of stubs available in the packet, and some status bits from the module, identifying possible errors or overflows. Then, inside a payload packet it's possible to identify the stub packets, which are fixed length, and carry information of the actual strip that has been fired, fine timing information (Bx), making it possible to identify the exact clock cycle in which it has been acquired, and the module from which it comes. A 64b word delimiter is added at the end of each payload, to take into account possible miscounting of the number of stubs in the header.

A high-speed C++ implementation of the decoding, loading packets into memory, and giving back translated information, has been implemented in the form of an API. Decoupling this step from the actual analyzer usable output was a key factor, simplifying the task of keeping the decoding in pace with all the modifications to the data format that have been implemented in the last years.

Regarding the output format, multiple solutions have been explored. During the first test beam, in 2021, given the low data rate, an attempt to store data in a JSON format was made. Even though the format could be compressed, is completely human readable and libraries for almost every programming language are available to read out JSON files easily, the format was abandoned mainly due to the time needed to read out the file. CERN Root Trees were in the end chosen as the format, due to their widespread use in the community, fast access time, and good compression.

Different options were explored for data organization. First attempts were done creating a set of custom classes that reflected the experimental setup: stations, containing modules, containing stubs. To implement this in a Root Tree, creating and maintaining a library with such classes was necessary. This first attempt was abandoned to enhance the easiness of using the data: participants of both MUonE and CMS experiments were interested in the analysis, with different necessities. The output format, in the end, features only objects from C++ standard library. An event in the output tree contains the stubs collected in one clock cycle (25 ns). Each branch is a C++ standard vector, containing reformatted information about the stub. Matching the same index of every branch gives the full stub reconstruction. In the branches, we have:

Local X Strip fired in the module, starting from 0 on the SEH side. This information is obtained from raw data combining the CBC index and the address and taking into account different CBC mappings for the two sides of a 2S module. Also, conversion from half strips to strips is performed;

Local Y addressing which CIC has been fired;

Super ID Orbit counter obtained in the payload

Bx Clock cycle in which the stub has been obtained;

Link Optical link, and so module, from which the stub came.

Module positions and their link was described in a JSON file needed by the decoder to run. This decoupling has been implemented to help with possible misconnections and misordering, allowing for simple software fixes during the decoding.

Some additional checks were implemented in the reformatting process. First of all, possible misordering from the Link Combiner was observed and corrected during the recombination. This has been done by loading stubs into a container-style object and then sorting them by time and reorganizing them by Bxs before writing them in the TTree branches. A cleanup of the stubs was also implemented, checking and removing stubs labeled by unphysical values (e.g. the CIC tags stubs containing errors with bend value equal to 8). Another feature was added, to revert data taking in sampled mode to latched mode: persistency removal. By implementing a double buffer pattern, it was possible to remove successive iterations of the same stub in subsequent Bxs.

A toolset for parallelization via the use of HTCondor of the whole decoding process has been written too, with a one-on-one match, producing a single root decoded file for every raw.

Performances of the whole daq-decode process have been tested, in order to estimate, given a target particle rate, the number of CPUs necessary to have almost online decoding of the files. Results, for a single AMD Ryzen 9 5900X 12-Core processor, are shown in Fig. 6.8 as number of decoded events per second per core. Performance is quite stable up to the number of physical cores, suddenly dropping when going into hyperthreading, so making a physical core run more than one thread, this behavior is under study.

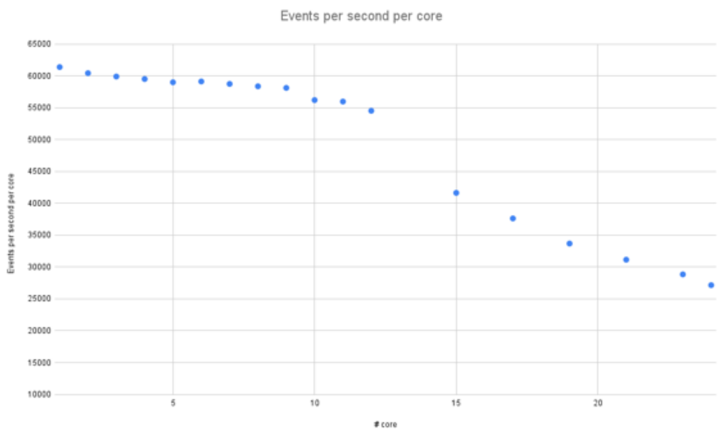

Fig. 6.8: Number of events processed by the daq-decode per core used in the machine.

As mentioned before, the readout of each station was handled in a separate way by the Serenity board, outputting two different file streams for each one. Data had to be merged to use information in the first station to reconstruct the incoming track and match it with the two outgoing tracks for electron and muon after the target. To do this, a separate tool called "merger", has been developed. Even though in principle the two processes - decoding and merging - should have been handled together, this is still under development. The merger used the same container-style approach used in the reformatting, reading files from the different stations, dumping the stubs in a given time range inside the container, and then sorting. Thanks to this approach, it was possible to make the process easily parallelizable, switching from a file-based approach to a time-based one, and dividing the output files into super id ranges.

6.3.2 Data quality monitoring tools

The development of Data Quality Monitoring (DQM) tools was quintessential to verify that everything was going smoothly during the test beams and test run. The aim of the system was to have a web-based toolset, with no need for external installations and the possibility to access it without being on-site.

This was achieved in various ways, and two different kind of DQMs were set into place. First of all, a so-called "online" DQM was created. It features really small latency with respect to the real system. The online DQM is based on a Prometheus [92] database, an open-source time-series database designed for monitoring and alerting, widely used for its scalability and reliability in dynamically changing environments. Information from all the temperature and humidity sensors, voltages, currents, and temperature retrieved from the lpGbt on the modules were exposed as web pages from separate programs running on one of the machines and then scraped by Prometheus. This led us with a complete time-based database, which dates back conditions during all the test beams performed. To interact with the database, a web interface was set in place using Grafana [93]. Grafana is an open-source analytics and interactive visualization web application, renowned for its ability to create complex dashboards that provide operational insights from a wide array of data sources, including Prometheus. This led us to an interactive web page, in which we could retrieve information from the complete run during every test. A screen of the web page obtained through this process for the whole environmental monitoring is shown in Fig. 6.9

Aside from environmental conditions, variables of great interest were the beam profile and the stub rate in each module. This was obtained by inserting two histogramming blocks in the firmware. This generated histograms for the stub position and number of packets received in real-time. The exposing, retrieving the information (scraping), and plotting process that happened for these plots is completely analogous to the one for the sensor and a screen of the obtained page is visible in Fig. 6.10.

Aside from this, which has been referred to as "online DQM", different instances of an "offline DQM" were developed. The offline DQM actually decoded via software part of the data shipped to EOS and performed more complex calculations, mainly taking into account module correlation. Starting from plotting the beamspots, up to making simple and coarse stub reconstruction efficiency calculations and identifying synchronization between modules. The offline DQM was delayed with respect to the online one by order of some minutes, taking into account the shipment and reconstruction time. During the tests, it incorporated different analyses, at first

Fig. 6.9: Screen of the Grafana page with environmental monitoring information.

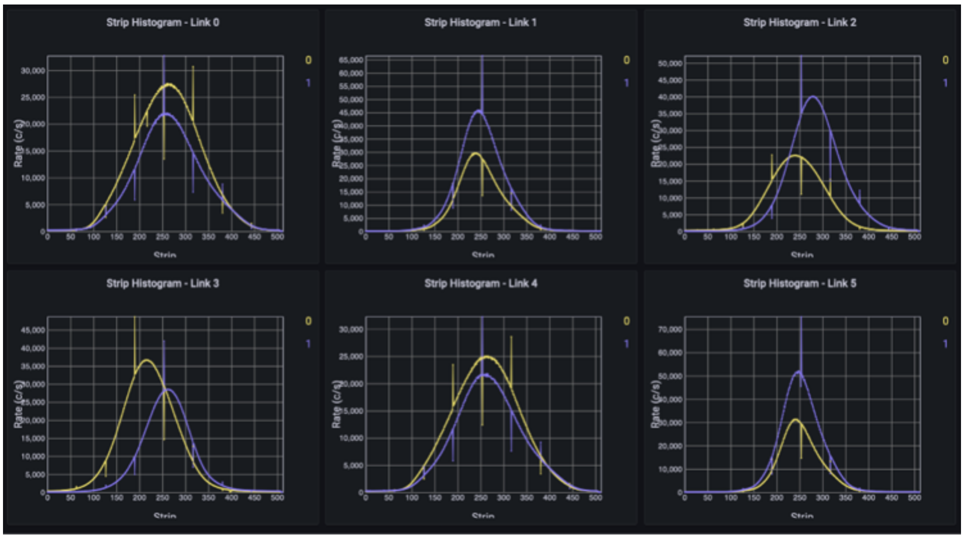

Fig. 6.10: Screen of the online DQM Grafana page with beam profiles obtained by the histogramming blocks implemented in the firmware.

performed manually by the analyzers, becoming a benchmark for the whole test run.

6.3.3 Event display

Between the tools developed, there's a web-based interactive 3D event display. Whilst this kind of tool isn't strictly necessary, it's nicely implemented for different reasons. First of all, different tracking reconstruction algorithms were implemented from different groups of the collaboration. While this is nice and enables cross-checks of the results, an event display makes it possible to easily compare different reconstructions and address possible problems. On the other hand, it helps with outreach purposes.

Key features for the event display development were for it to require minimal installation, so a web-based format was chosen. The implementation was done in javascript, using the WebGL [94] library. WebGL, short for Web Graphics Library, is a JavaScript API Built on the principles of OpenGL ES 2.0 [95] for rendering interactive 2D and 3D graphics within any compatible web browser without the use of plug-ins.

The javascript program, at the present time, takes as input a list in the form of JSON file of stubs and tracks, organized in events. An event can contain any number of stubs and/or tracks, in the form of lines in space. Lines can be represented both as two points or as a point plus a director vector. APIs for conversion of stubs from the ROOT Tree format described in Sec. 6.3.1 have been also developed, leaving to the user only to appropriately convert their track into a suitable parametrization. Subsequent display of more complex tracks is certainly possible. The actual design leads to what's visible in Fig, 6.11, a 3D event display in which modules are displayed as squares, with different colors per side, with the FEH highlighted in green. The possibility to load directly the CAD drawings is implemented in OpenGL and is planned to be used in future developments.

Future plan is to create a direct link to the event display to a database, avoiding the process of feeding the program JSON files. This way, a web interface that scrapes information from the database can be obtained, and adding a new event would just require adding another entry in the database. This process would ensure maximum accessibility of the tool from the whole collaboration, avoiding the need to run it locally.

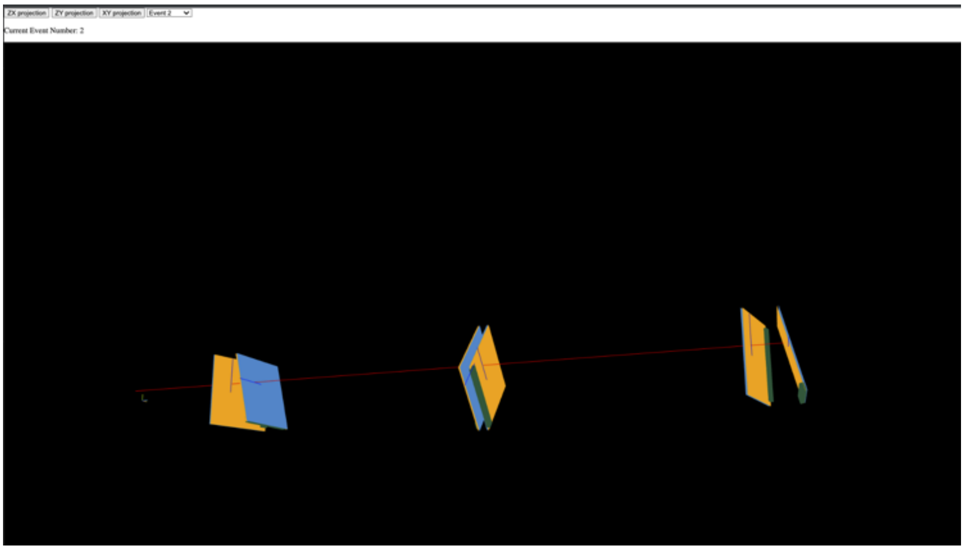

Fig. 6.11: Captured screen of the event display running on a browser session.

6.4 Data analysis

A data analysis requiring tracking in the whole system was performed. The main purpose of this work was to ensure that the whole data acquisition chain was consistently working. In order to do so, both module performances, as efficiency and resolution, and physical quantities of interest for MUonE were extrapolated. In the next paragraphs the methodology, starting from the approach to tracking up to the extraction of quantities of interest, will be shown.

6.4.1 Tracking

The tracking methodology developed herein was prompted by limitations encountered during previous beam tests. Prior to the 2023 test run, the availability of 2S modules was limited, constraining our capacity to equip more than a single full station. Additionally, there was an absence of a suitable telescope for correlating tracks with the modules under test. Consequently, a flexible tracking approach was needed, capable of utilizing any available combination of modules for track reconstruction.

The adopted strategy focuses exclusively on the reconstruction of straight-line tracks. This is achieved by treating the activated strips in each module as individual segments within a three-dimensional space. The reconstruction process then associates the track to the line that minimizes the aggregate squared distance to all these stub-segments. Initially, this minimization mirrors the pattern observed in a χ^2 (chi-squared) distribution. Subsequently, with the resolution of each module determined, the process transitions to a formal χ^2 minimization approach.

6.4.2 Alignment

An initial and crucial step in our experimental setup involves the alignment of modules. The CERN metrology team provided precise metrology measurements of the modules' positions within the station, achieving an accuracy of up to 2 μm. However, structural deformations were observed: the frames to which the modules were screwed did not align perfectly with their designated placements, casting doubts on the reliability of these precision measurements.

In response to this challenge, an iterative strategy starting from the design measurements sourced from the CAD drawings of a station (Fig 6.12) was employed. The guiding metric for these adjustments was the residuals, defined as the difference between the measured position of a stub and its expected position from the fitted track.

A specific subset of the complete dataset was employed, wherein instances were selected based on the criterion of having precisely one reconstructed stub per module. This represented approximately 20% of the total dataset, as illustrated in Fig. 6.13. The primary objective of this selection criterion was to optimize the probability of accurately reconstructing a straight muon trajectory.

The iterative process, for each Device Under Test (DUT), started by first reconstructing the muon track using all modules except the DUT. Subsequently, this reconstructed track was extrapolated to the DUT's position, and the difference between the extrapolated track and the reconstructed stub at the DUT was computed to derive the residual distribution. The modules were then adjusted in the x, y, and z directions by an amount equal to the negative mean of this distribution, to center the distribution around zero. The methodology for correcting rotational misalignments was distinct. Each iteration involved an optimization process, wherein a scan for the optimal rotation about the previous value was conducted. The optimal rotation was determined based on achieving the most favorable χ^2 fit of the residual distribution to a Gaussian function. All parameters were updated in accordance with these findings in subsequent iterations. To mitigate potential biases, the order of the DUTs was randomized in each iteration.

Post ten alignment iterations, the residual distributions for the x and y coordinates, as shown in Figs. 6.14 and 6.15 respectively, demonstrated a robust fitting with Gaussian distributions and mean within approximately 2 μm.

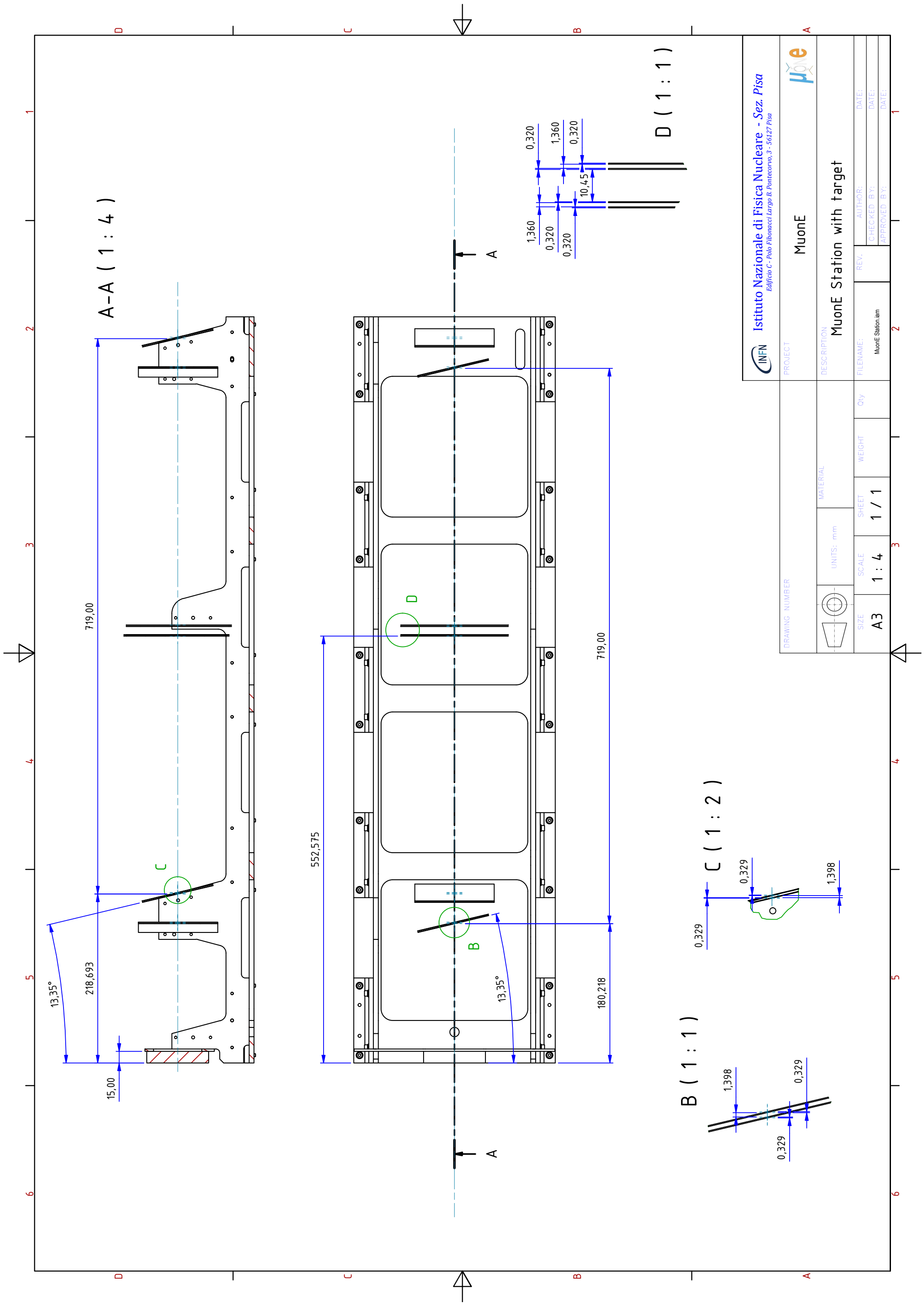

Fig. 6.12: CAD drawing of one of MUonE stations.

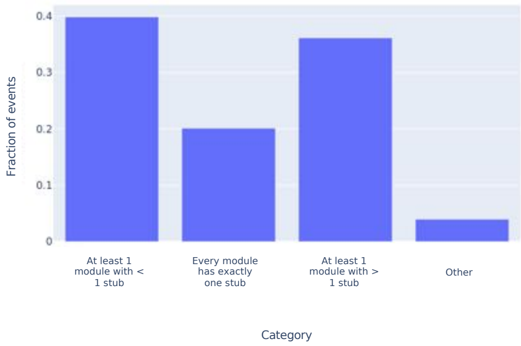

Fig. 6.13: Fraction of events per different categories of number of stubs in each module in absence of target.

Fig. 6.16 presents the deviations from the nominal position obtained after ten iterations of the alignment process. This procedure was replicated for different data samples spanning various periods, specifically including three samples each from a low-intensity muon beam without a target (Run 2) and one with a 3 cm target installed and a high-intensity muon beam (Run 7). Remarkably, the deviations observed were consistent both across different periods and runs, with translations deviating up to 2 mm from nominal values and rotations within a 0.01 radiants range. This consistency is further corroborated by Figs. 6.17 and 6.18, where the sigma values obtained from the Gaussian fit to the residual distributions for both x and y coordinates are depicted. In both cases, the obtained residual distribution for the first and last modules is broader. This is due to the higher error in the track extrapolation. These figures demonstrate that even when calculating residual distributions under varying conditions, the results remain compatible. Currently, the MUonE collaboration is exploring alternative strategies, such as global alignment, in order to find a more robust, flexible, and performing method.

Noteworthy is the fact that in this alignment approach, all modules are treated as freely positioned objects in space. This method does not account for the modules being physically affixed to the stations, which are rigid structures. A more comprehensive approach would involve initially aligning the stations relative to each other by matching reconstructed tracks, followed by aligning the modules within these stations. This enhanced methodology is still in the developmental stage.

6.4.3 2S Modules performances

Two different studies have been conducted to characterize two of the most interesting quantities related to the modules: resolution and efficiency.

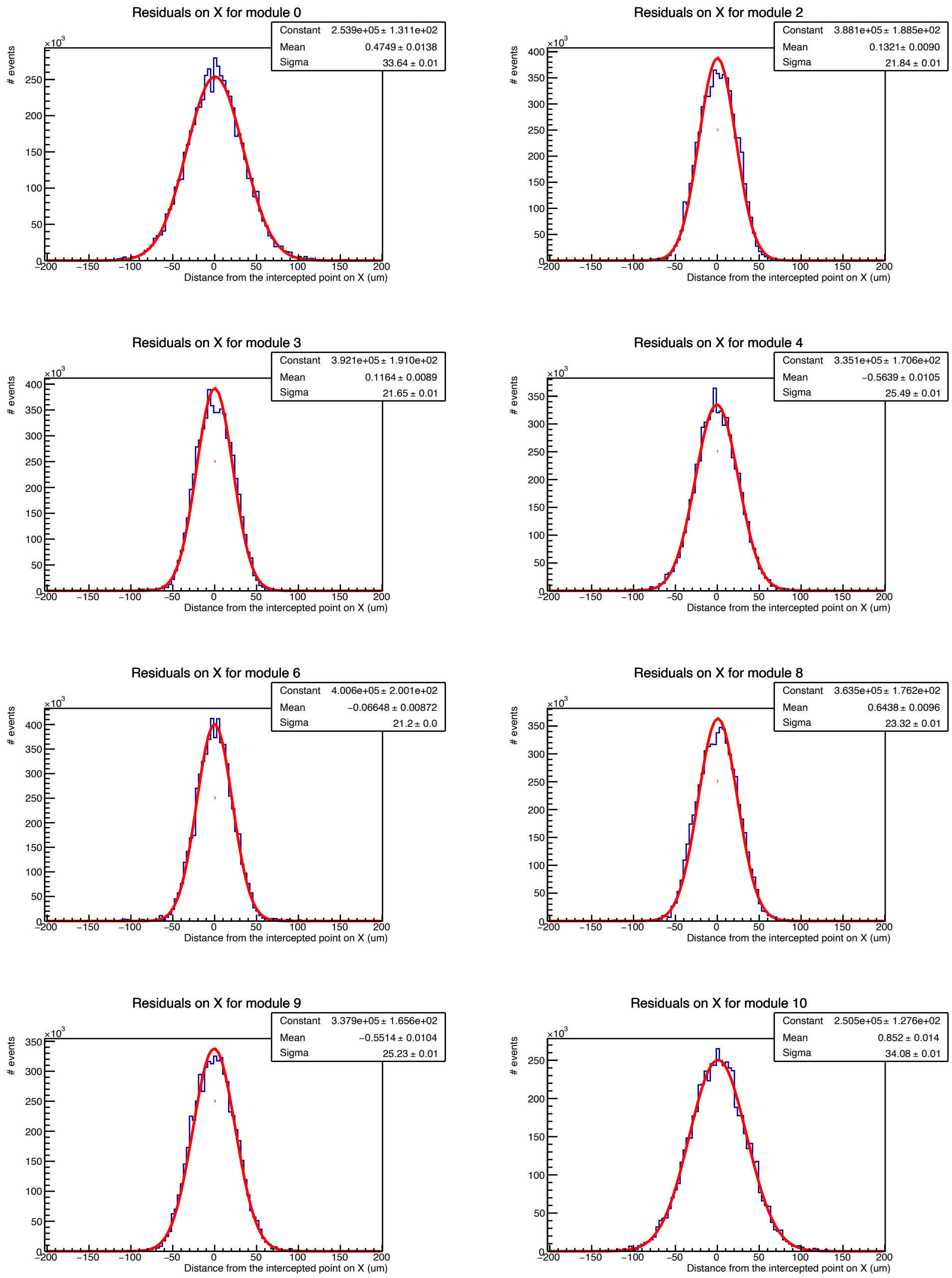

Fig. 6.14: Residuals on x coordinate for every module, calculated over 6 million tracks and fitted with a gaussian.

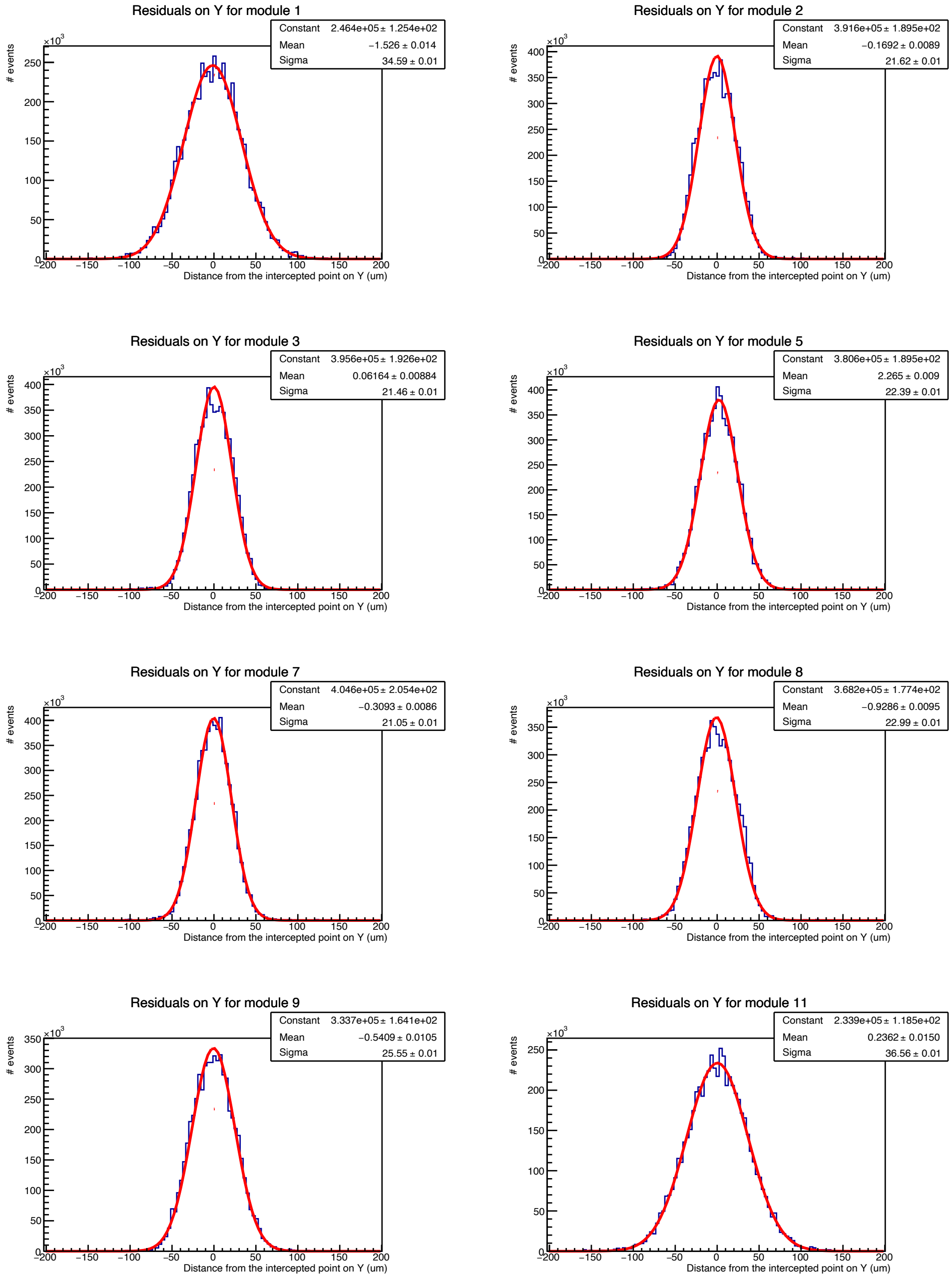

Fig. 6.15: Residuals on y coordinate for every module, calculated over 6 million tracks and fitted with a gaussian.

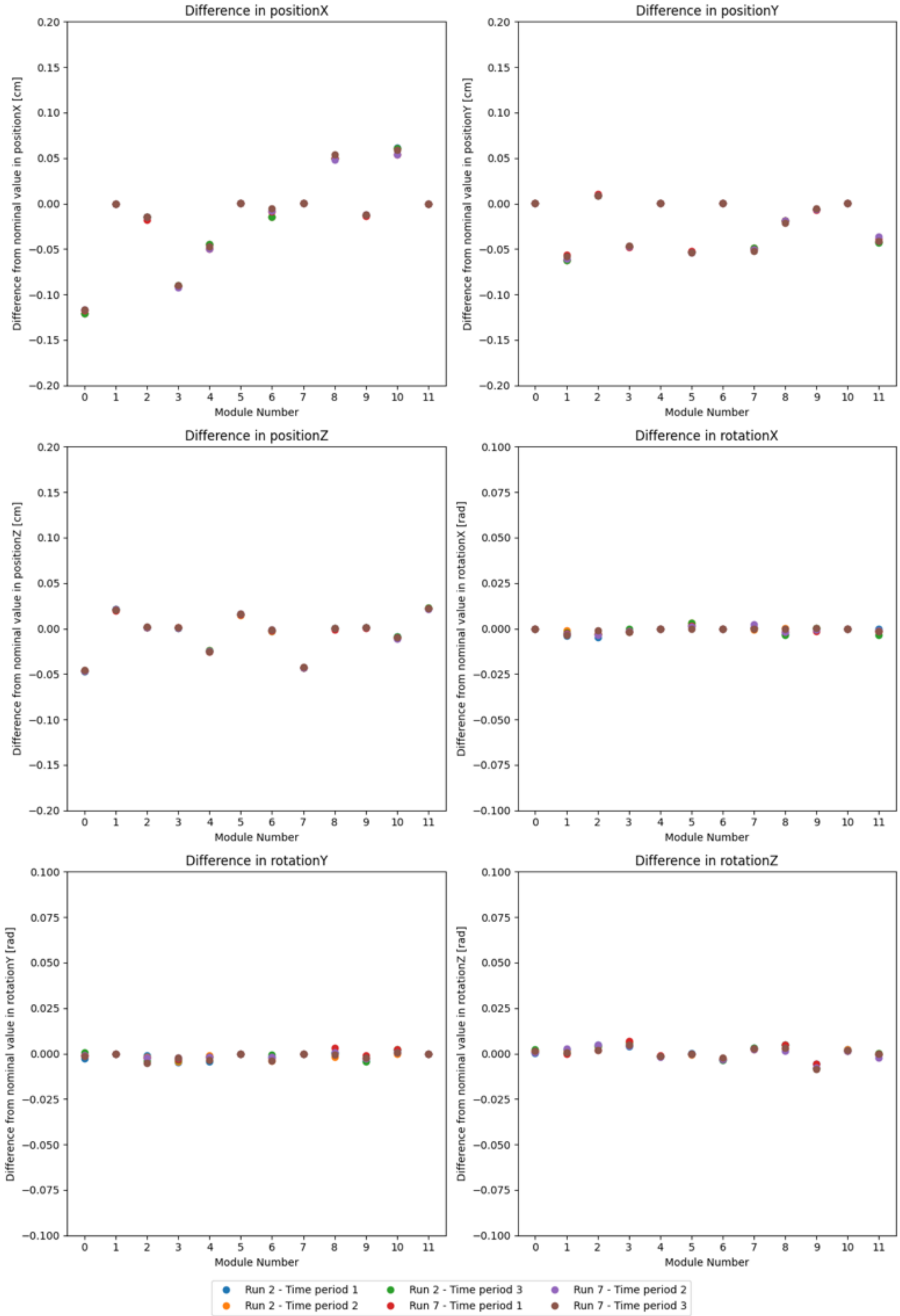

Fig. 6.16: Difference with respect to the nominal position after the alignment for every module, for three different time samples in two different runs, with and without target.

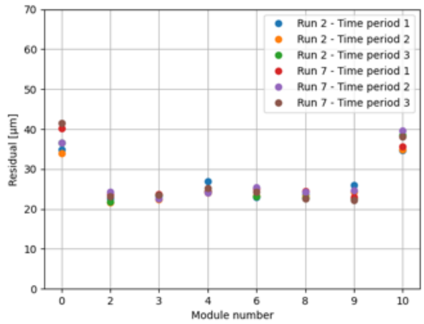

Fig. 6.17: Comparison of obtained residual on the x coordinate for each module, for different runs and time periods inside the runs.

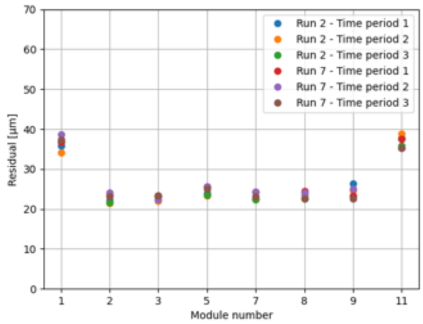

Fig. 6.18: Comparison of obtained residual on the y coordinate for each module, for different runs and time periods inside the runs.

6.4.3.1 Single hit resolution

Given the distribution of the residuals, for i-th module's residual we have:

$$r_i = x_{tk,i} - x_{Hit,i} \tag{6.1}$$

obtaining the actual resolution of the i-th module:

$$\sigma_{Hit,i} = \sqrt{\sigma^2(r_i) - \sigma^2_{tk,i}(\sigma_{Hit,j})} \tag{6.2}$$

In this equation, the error on the track reconstruction ($\sigma^2_{tk,i}$) is still dependent on the resolution of all the other modules, being:

$$\sigma^2_{\text{tk},i} = \sum_{i,j} \frac{\partial x_{\text{tk}}}{\partial p_i} \frac{\partial x_{\text{tk}}}{\partial p_j} V_{ij} \tag{6.3}$$

Being the resolution of the single module in principle unknown, an iterative approach is again used. The steps are the following:

1. Initial resolutions for all the modules are assumed equal as a parameter $\sigma^0_{Hit,i}$;
2. Track is reconstructed excluding the DUT, with a χ^2 fit, minimizing:

$$\chi^2 = \sum_{i=0}^{\text{N}_{\text{modules}}-1} \left(\frac{x_{\text{Track}}\left(z_{\text{hit},i}, \vec{p}\right) - x_{\text{Hit},i}}{\sigma^0_{\text{Hit},i}} \right)^2 \tag{6.4}$$

3. Estimate $\sigma(r_i)$ with a Gaussian fit to the core of the residuals ($\pm 2\times$Std.Dev.);
4. Update the values of $\sigma^{(1)}_{Hit,i} = \sqrt{\sigma^2(r_i) - \sigma^2_{tk,i}(\sigma_{Hit,j})}$;

5. Use $\sigma^{(1)}_{Hit,i}$ for a new tracking reconstruction;

6. Repeat iteratively until convergence.

Different initial values for the resolution of a module were explored, ranging from $10\,\mu$m to $30\,\mu$m. These variations led to consistent results, with a convergence observed within 3 to 5 iterations during the same period and run. Fig. 6.19 displays the outcomes of the iterative process, beginning at $20\,\mu$m, for six distinct datasets (three from Run 2 and three from Run 7). This comparison illustrates comparable resolution outcomes for the same module under varying conditions. Tab. 6.2 lists the resolution values for each module, calculated as the average from the different datasets examined. Upon comparing these values with the theoretical resolution for a digital readout of a $90\,\mu$m strip, calculated as $90/\sqrt{12} \approx 26\,\mu$m, and for a half-strip digital readout, $45/\sqrt{12} \approx 13\,\mu$m, it is inferred that the actual resolution lies between these two theoretical values. This suggests that the detector is responding to muons that release charge in either one or two strips.

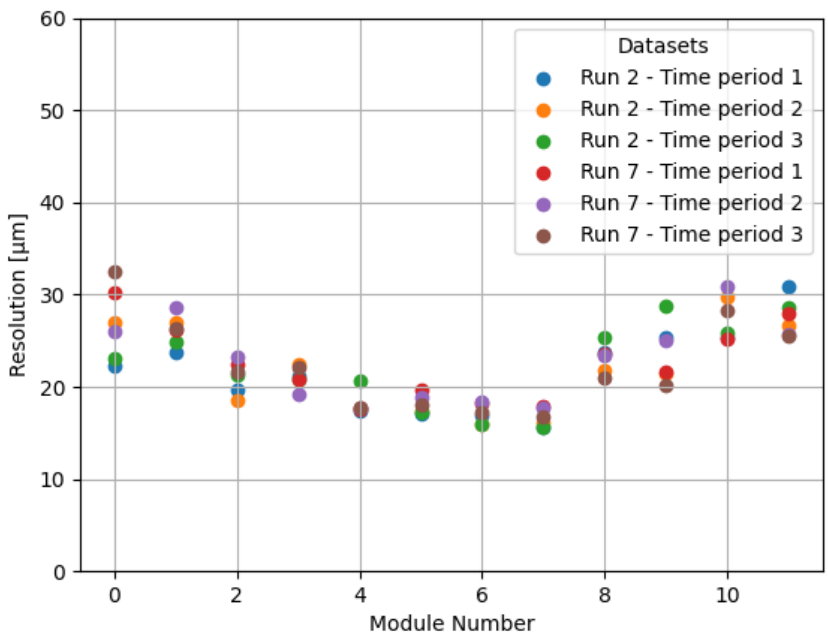

Fig. 6.19: Calculated resolution for each module, for three different time samples in two different runs, with and without target.

Module Number	Resolution [μm]
0	26.8 ± 1.6
1	26.1 ± 0.7
2	21.1 ± 0.7
3	21.1 ± 0.5
4	18.2 ± 0.5
5	18.1 ± 0.4
6	17.1 ± 0.4
7	16.6 ± 0.4
8	23.1 ± 0.6
9	23.7 ± 1.3
10	27.6 ± 1.0
11	27.5 ± 0.8

Tab. 6.2: Calculated resolution for each module, as the mean of the values obtained for different data samples.

6.4.3.2 Efficiency

Upon determining the resolution for each module, it becomes feasible to refine the tracking procedure by minimizing a χ^2 function, allowing for a hit efficiency measurement. The hit efficiency, ϵ, is defined as:

$$\epsilon = \frac{N_{\text{good}}}{N_{\text{total}}} \tag{6.5}$$

In this equation, N_{total} represents the number of reconstructed tracks that have a hit in all modules except the DUT and exhibit a $\chi^2/n_{\text{dof}=2} < 2$. Conversely, N_{good} is the subset of these events that also register a hit in the DUT within a maximum distance of $5 \times \sigma_{\text{DUT}}$ from the position extrapolated from the reconstructed track.

Initially, the efficiency as a function of time for all modules was computed. Fig. 6.21 displays the efficiency values observed during a spill, indicating consistent performance over time within the same module. Subsequently, the integrated efficiency of each module was calculated, demonstrating consistency across multiple datasets. Tab. 6.3 presents these computed values along with their errors, which were determined using a Bayesian approach with a prior assumed to be uniformly distributed in the range from 0 to 1. Fig. 6.20 illustrates these measurements. The overall efficiency is observed to be around 98%, with a notable decline to approximately 95% in module number 5, related to known setup issues related to the bias of the sensor.

The efficiencies reported here differ from the $> 99\%$ efficiency typically cited by CMS. This discrepancy primarily stems from the triggerless data acquisition system employed in this test beam, where the clock was not synchronized with the incoming

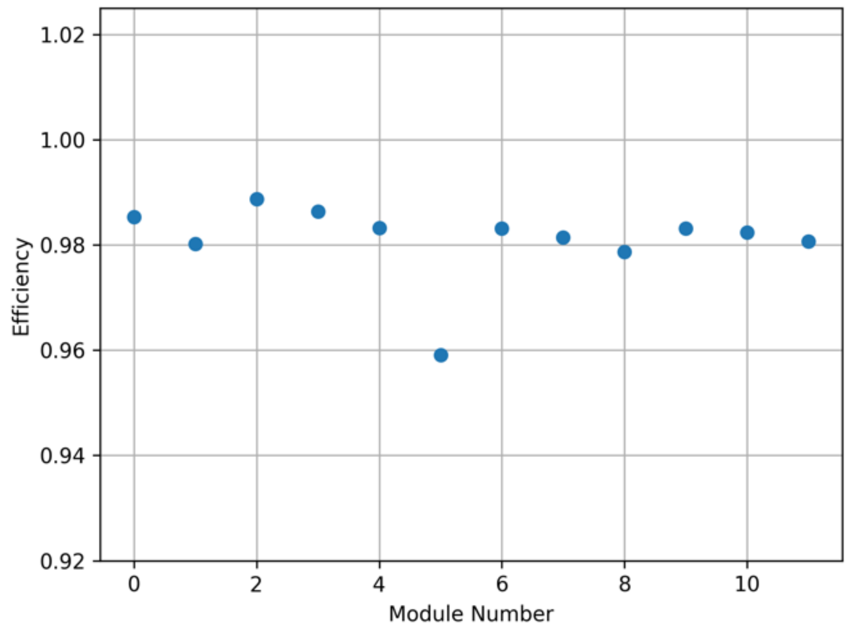

Fig. 6.20: Integrated efficiency comparison for each module.

particles. This asynchrony led to some periods of dead time, as particles could traverse the sensor at the edge of the clock cycle.

Additionally, to investigate potential inefficiencies in individual chips, the efficiency per strip was calculated. Fig. 6.22 illustrates these findings. Given that the beam was centered relative to the modules and covered an area of approximately 5×5 cm^2, this leads to limited statistics for strips near the edge of the module, as confirmed by larger error bars. Generally, the efficiency is fairly consistent across the modules, barring a few malfunctioning strips. An anomalous behavior is observed in module 11, which exhibits different efficiencies in the two halves of the sensor. The underlying cause of this discrepancy is currently being investigated.

6.4.4 Extraction of elastic scattering events

The subsequent step in the full characterization of the DAQ chain for 2S modules involves reconstructing a real physics process. The process selected for this study is of significant relevance to MUonE, namely, the muon-electron elastic scattering.

For this purpose, a data sample from a run utilizing a 3 cm carbon target (specifically, Run 7) was selected. This sample underwent a cleaning process, wherein exactly one stub per module in the first station was required, enabling the tracking of the

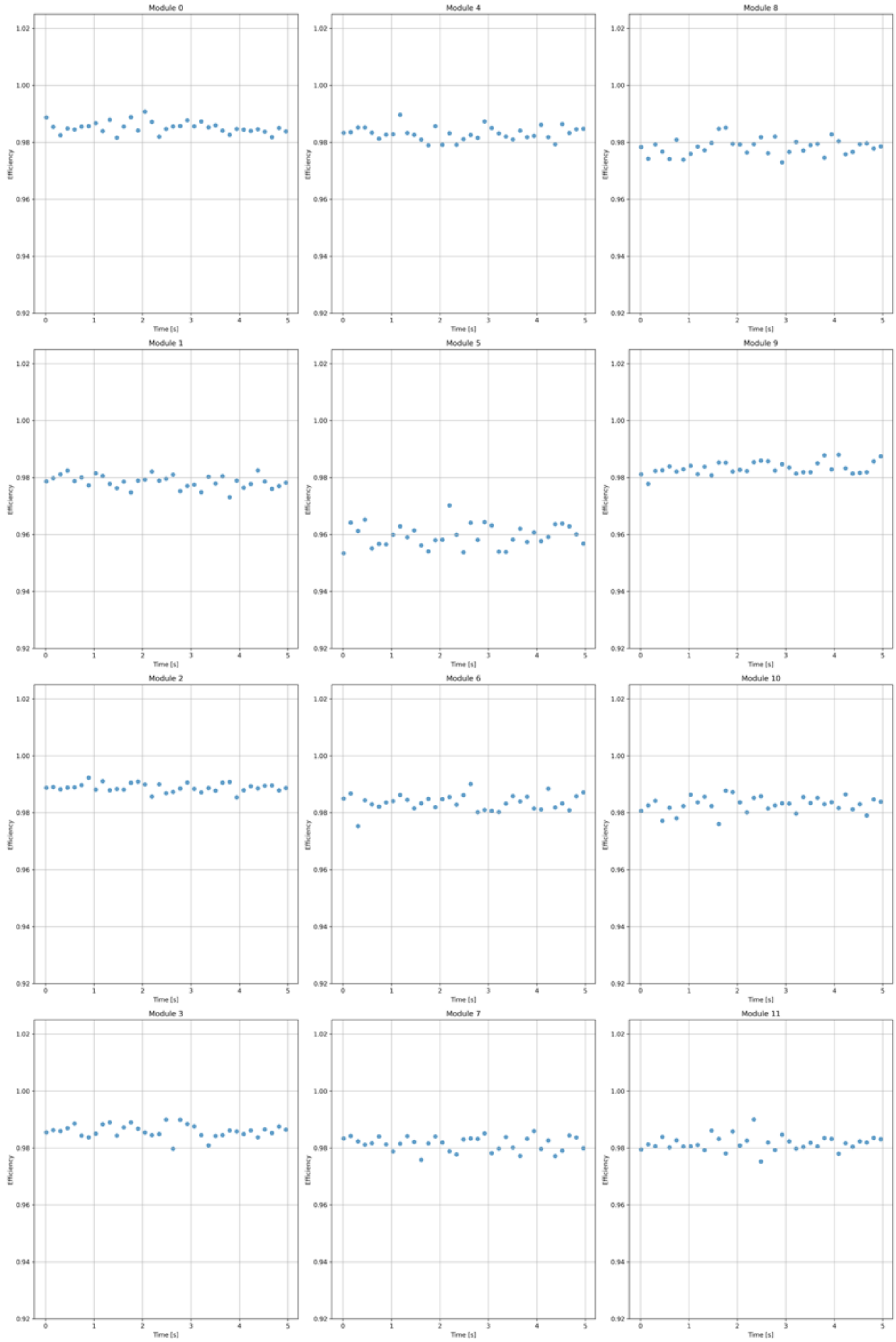

Fig. 6.21: Efficiency for each module during a spill.

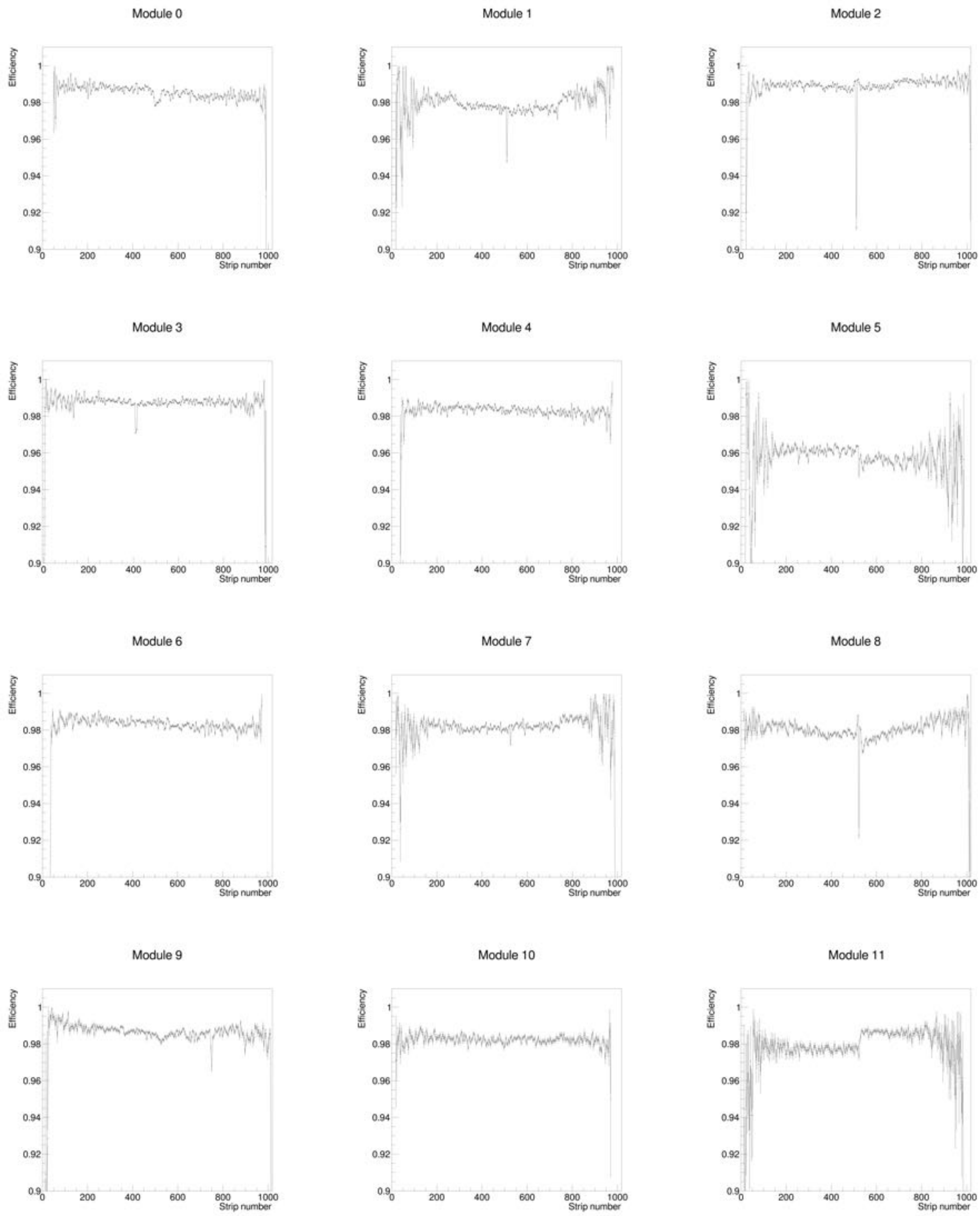

Fig. 6.22: Efficiency for each module as function of the position of the expected strip.

Module Number	Efficiency (%)
0	98.53 ± 0.01
1	98.03 ± 0.01
2	98.87 ± 0.01
3	98.64 ± 0.01
4	98.33 ± 0.01
5	95.90 ± 0.02
6	98.33 ± 0.01
7	98.17 ± 0.01
8	97.85 ± 0.01
9	98.34 ± 0.01
10	98.24 ± 0.01
11	98.09 ± 0.01

Tab. 6.3: Cumulative efficiency calculated for each module.

incoming muon's angle. In the second station, exactly two stubs per module were required, to maximize the number of events with real muon-target interaction. This selection criterion, as depicted in Fig. 6.13 and Fig. 6.23, yielded efficiencies of approximately 20% in the first station and 10% in the second.

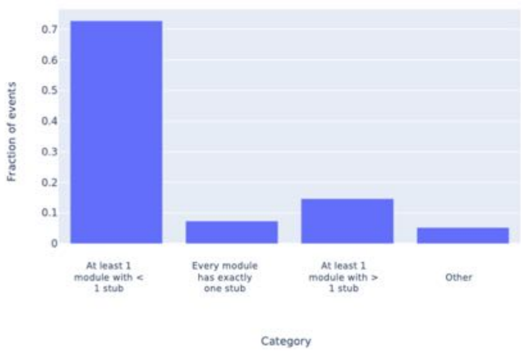

Fig. 6.23: Fraction of events per different categories of number of stubs in each module with presence of target.

In the second station, two tracks are reconstructed. Stub sharing was not permitted in this study, although future studies must consider it: particularly for small scattering angles two particles might trigger the same strip without $\sim$ 10% probability in the first two modules upstream. The first track is identified from all stub combinations as the one with the optimal χ^2 value, and the second track is then reconstructed using the remaining stubs.

The interaction vertex is subsequently determined as the closest point to the two reconstructed tracks, treated as linear trajectories in space. These tracks can be parameterized as

$$T_i = P_i + t_i V_i, \tag{6.6}$$

where T_i is a generic point on the track, P_i represents a fixed point of the track and V_i are the components of the directional vector $\vec{V_i}$.

The shortest segment connecting these tracks will be orthogonal to both. Assuming this segment originates from an arbitrary point on T_1, denoted as $P_3 = P_1 + t_1\vec{V_1}$, it can be expressed by the equation:

$$L_3 = P_1 + t_1\vec{V_1} + t_3\vec{V_3}, \tag{6.7}$$

where $\vec{V_3} = \vec{V_2} \times \vec{V_1}$, ensuring perpendicularity to both tracks. To determine the point of intersection with T_2, we solve a system of three linear equations. This solution defines the shortest segment between the two tracks, allowing for the straightforward calculation of the vertex as the midpoint of this segment.

Fig. 6.24 shows the distribution of the distance between the reconstructed vertex and the incoming track, as reconstructed from the first station. Despite the expected peak for a perfectly aligned system should be at 0 μm, the peak is observed well under 100 μm. This discrepancy arises from the alignment procedure. As outlined in Sec. 6.4.2, this procedure does not consider the two stations as rigid bodies, highlighting an area for refinement in future studies.

Furthermore, Fig. 6.25 displays the distribution of events relative to the two angles between the incoming and outgoing tracks at the target. These angles are sorted by magnitude, owing to the absence of particle identification, which precludes differentiation between the electron and the muon. The most densely populated region in this distribution evidently aligns with the expected profile of elastic scattering events, as corroborated by the comparison with Fig. 5.6.

Additional refinement of the selection is possible, beginning with the reconstructed position of the scattering vertex along the Z-axis, expected to be within the target. The distribution of this variable is presented in Fig. 6.26. As discernible from the figure, a Gaussian peak is apparent around 101 cm, aligning closely with the nominal position of the target at 101.2 cm on the Z-axis. Fitting this distribution yields an estimated mean of 101.2 cm and a standard deviation of 1.5 cm, consistent with the target's nominal position and its thickness of 3 cm. Interestingly, an additional minor peak is observed at approximately 93 cm in Fig. 6.26, coinciding with the position

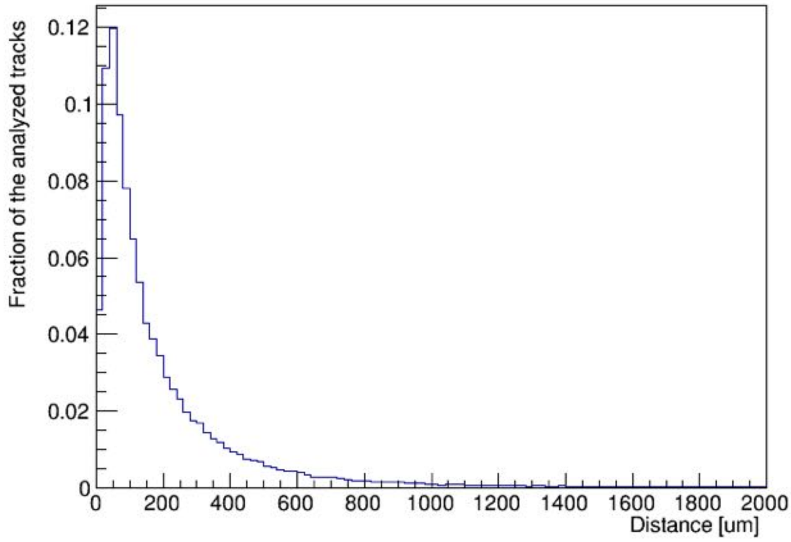

Fig. 6.24: Distance between the reconstructed vertex and the incoming track in the first station.

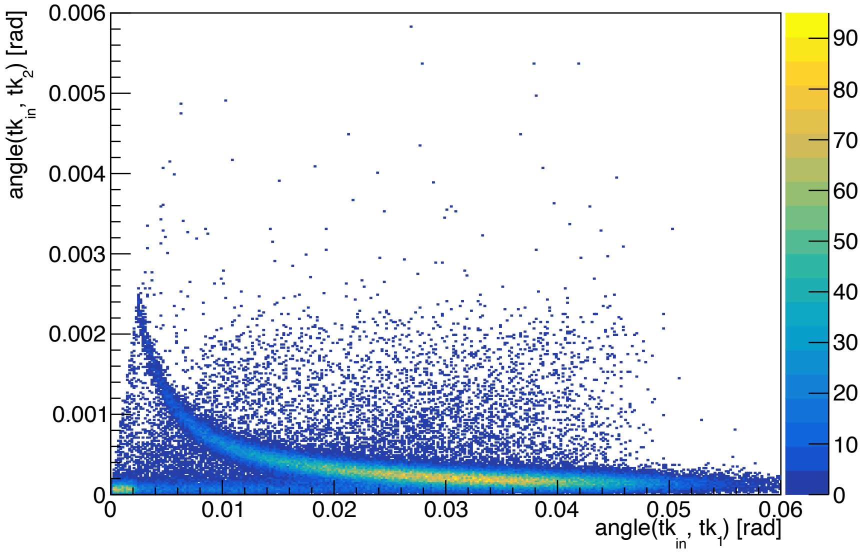

Fig. 6.25: Preliminary analysis for the angle reconstructed between the scattered muon and electron on partial statistics for 2023 Test Run, no cuts applied after the cleanup selection. On the x (y) axis, the angle between the incoming track and the outgoing track with higher (lower) angle.

of the last module in the first station. This suggests that some scattering events are occurring in the final silicon sensor of the first station.

To ensure the interaction occurs within the target, a cut is applied to the Z-coordinate of the reconstructed vertex. This cut, set at 3σ around the mean value of the fitted distribution, is depicted in Fig. 6.26 by two vertical blue lines. This cut achieves an efficiency of approximately 85%, resulting in the angular distribution shown in Fig. 6.27. Here, a distinct reduction is visible in the region with low angles ($\mathrm{tk_{in}}$, $\mathrm{tk_2}$), likely representing pair production events with an undetected electron, where the angle between outgoing particles is uncorrelated.

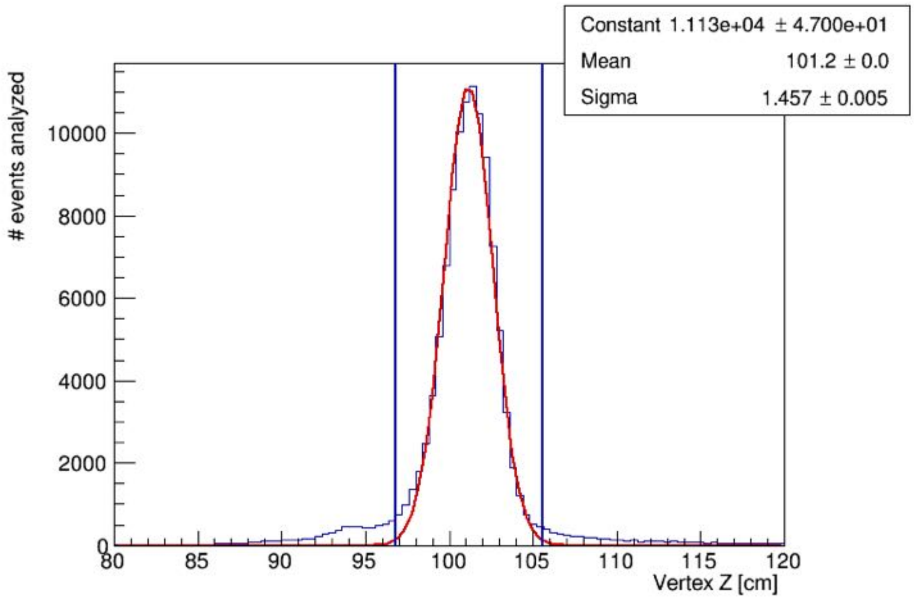

Fig. 6.26: Distribution of the Z-coordinate of the reconstructed vertex in the second station. Blue vertical indicates a window of $\pm\ 3\sigma$ around the mean, used to cut on the vertex position.

Further refinement in track reconstruction is achieved by implementing a cut on the tracks' χ^2, as depicted in Fig. 6.28. A conservative cut of $\chi^2/n_{\mathrm{dof}=2} < 10$ is applied to all tracks, leasing to a ~15% efficiency. This criterion is particularly stringent when applied to the second reconstructed track's χ^2, given the reconstruction methodology. This leads to a much cleaner selection, evident in Fig. 6.29, where primarily the region corresponding to elastic scattering remains. Additionally, events in the region with low angles ($\mathrm{tk_{in}}$, $\mathrm{tk_2}$) persist, likely representing pair production with an unobserved electron, a physical process that cannot be excluded merely through cuts on track quality.

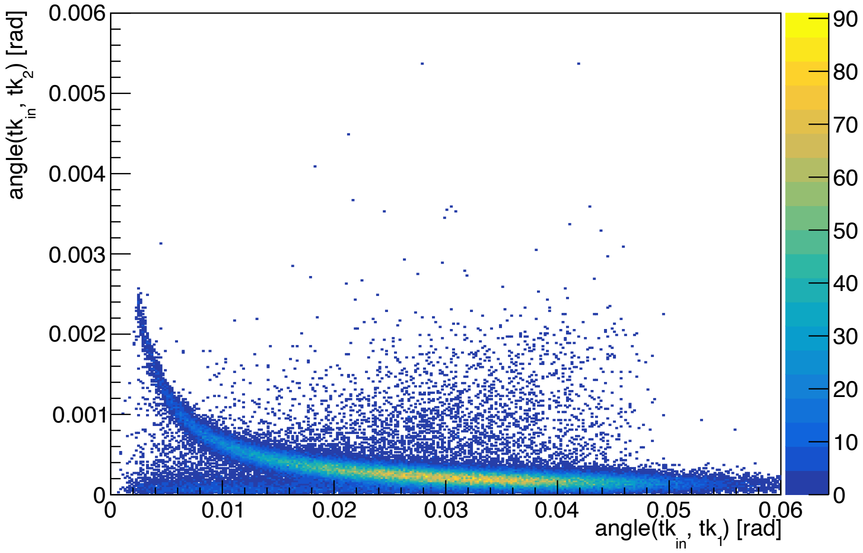

Fig. 6.27: Preliminary analysis for the angle reconstructed between the scattered muon and electron on partial statistics for 2023 Test Run. Here, a cut on the vertex position, as shown by the two vertical lines in Fig. 6.26 is applied. On the x (y) axis, the angle between the incoming track and the outgoing track with higher (lower) angle.

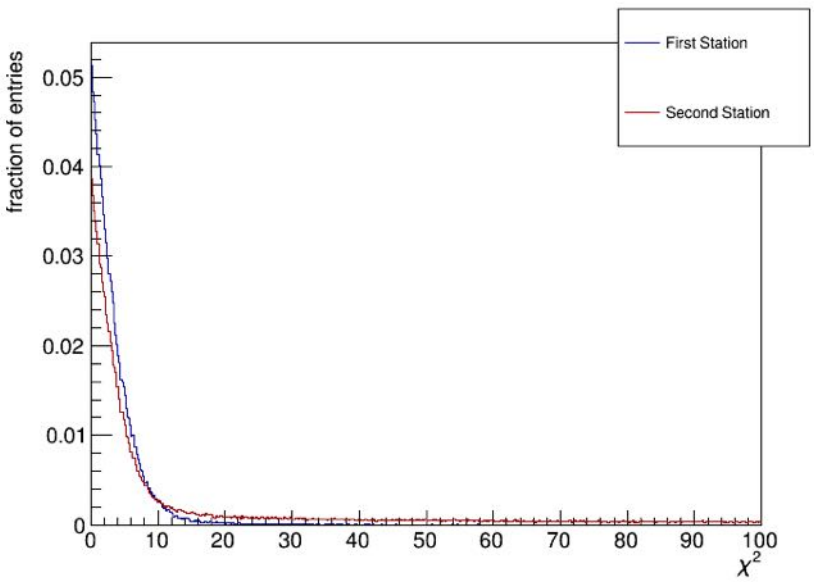

Fig. 6.28: χ^2 of the reconstructed tracks in the first (black) and second (red) station.

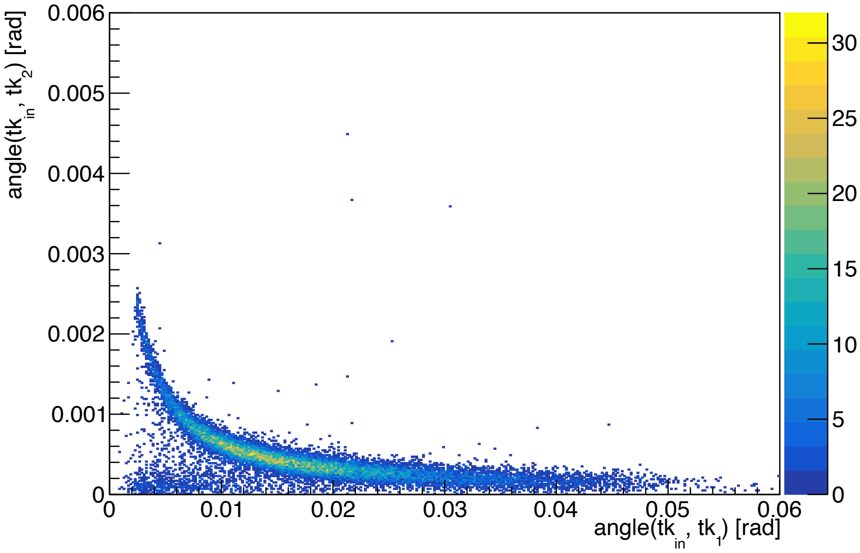

Fig. 6.29: Preliminary analysis for the angle reconstructed between the scattered muon and electron on partial statistics for 2023 Test Run. Both cuts on the vertex position and on the χ^2 of the tracks are applied. On the x (y) axis, the angle between the incoming track and the outgoing track with higher (lower) angle.

7 Conclusion

The forthcoming upgrade of the LHC to the HL-LHC, scheduled during the Long Shutdown 3 between 2025 and 2028, marks a pivotal advancement in particle physics research. This upgrade aims to significantly increase the instantaneous and integrated luminosity, enabling the LHC to gather sufficient data for precision measurements in processes with small couplings. Such enhanced capabilities are crucial for exploring new physics phenomena and conducting unprecedented measurements.

However, this increase in luminosity presents formidable challenges for the major experiments, particularly in handling the increased particle flux. The experiments, including CMS, must adapt to endure heightened radiation levels and maintain, if not surpass, the current standards of data reconstruction and analysis efficiency.

The CMS experiment, as part of its comprehensive upgrade strategy, will undergo several significant modifications. These include upgrading the front-end electronics for the muon chambers, integrating novel detectors such as HGCAL and MTD, and a complete overhaul of the tracker system. This overhaul is not merely a technical update but represents a paradigm shift in the tracker's operational strategy.

On one front, the IT will be equipped with entirely new sensors, featuring the inclusion of 3D sensors in the inner barrel. On the other front, the OT will be completely redesigned to accomplish one of the most ambitious aspects of the CMS upgrade: the incorporation of tracker data into the L1 trigger system. Integrating the OT information at the L1 stage is a revolutionary step, enhancing the ability to select events of interest more effectively amidst a vastly dense collision environment. This paradigm shift will happen mainly with the development of new p_T modules, namely PS and 2S. These modules, consisting of two closely-spaced coupled sensors read out by the same electronics, are capable of making an online selection on the particle's momentum and provide a 40 MHz data stream with coupled information from both sensors. Achieving such a rapid readout, coupled with the intricate design of the chips for managing different data streams, creating and managing stubs, and enabling crosstalk between adjacent chips, all while maintaining performance in the face of radiation damage and reducing the amount of material inside the tracker, is an extraordinary challenge.

The assembly process for the PS and 2S modules has been the subject of extensive study over several years and has undergone numerous modifications. The meticulous attention to the stringent mechanical constraints, comprehensive heat sink analyses, and the detailed characterization of the chips' behavior, as well as the electrical properties from various pre-production batches, have required considerable effort.

In tandem with the module assembly, there has been a parallel development of the entire DAQ chain. Initially, the FW and SW for the μDTC were developed. The μDTC tools, aimed at testing the modules in the assembly centers and in test-beam conditions, allow now to configure, characterize, and read out full modules consistently. A hybrid test system, relying on the same technology, was also developed, to be installed at the hybrid assembly manufacturer. Recent efforts have been made to enhance the robustness of the software and firmware used in these tests, especially regarding PS FEH. Subsequently, the firmware for the final boards was developed. Concurrently, the software for module management underwent porting from the μDTC to the DTC, taking into account the differences between the boards. While the firmware for track finding is still in the development phase, the trigger stream readout on the final boards has been successfully validated in numerous test beams. This validation was achieved through a collaborative effort between the MUonE and CMS teams.

Some technical advancements for the CMS OT upgrade find application in the MUonE experimental proposal. With its simple layout consisting of a modular 40-meter-long tracker, MUonE aims to investigate an intriguing physics process. Its primary objective is to measure a_μ^{QCD} through the process of μ on e scattering. This is of significant interest in the physics community, as it offers a promising avenue for resolving the discrepancies between theoretical predictions and experimental measurements in the g-2 calculations. MUonE collaboration selected the 2S CMS OT Phase-2 modules for tracking. This choice has fostered a productive interplay between the MUonE and CMS experiments over recent years. MUonE has benefited from the expertise of CMS DAQ specialists, while CMS has had the opportunity to test parts of its DAQ chain with reduced personnel requirements.

The test run of the MUonE experiment, conducted from August 21st to September 10th, 2023, at the M2 beamline, serves as compelling evidence of the efficacy of the 2S modules and DAQ chain. The success in characterizing 2S CMS modules within an asynchronous environment, achieving notable measurements such as efficiency and resolution beyond the usual LHC context, not only proves the modules' durability but also affirms the comprehensive design approach of the CMS upgrade in preparation for HL-LHC conditions. Moreover, the development of firmware and software tools for the test run, with an eye on scalability for the full MUonE experiment, combined with the successful measurement of the μ on e elastic scattering angle, highlights the viability of the MUonE experiment. This achievement simultaneously validates the functionality of a DAQ chain akin to that planned for CMS.

The MUonE experimental proposal is currently being drafted, focusing on extracting a_μ^{EWK} from the data gathered during the recent test run. This task is crucial as it serves as a comprehensive proof of concept for the experiment's feasibility. Upon approval, the MUonE experiment is slated to undergo another test run, this time with approximately 10 stations, before it progresses to its full-scale implementation. Such a development also presents a valuable opportunity for the CMS experiment: the pre-production phase for OT modules has recently concluded, and the transition to full-scale production is imminent. The complete installation of the new tracker is scheduled for the Long Shutdown 3 period. In this context, conducting rigorous stress tests with a high number of modules becomes imperative.

Moreover, these tests offer a unique opportunity to evaluate other significant aspects, such as the track-finding algorithm, with a direct physics application in mind. This collaboration between MUonE and CMS exemplifies a synergistic approach that could serve as a model for future high-energy physics experiments. It highlights the benefits of leveraging shared expertise and resources, thereby facilitating mutual progress in the field.

Bibliography

[1]Lyndon Evans and Philip Bryant. „LHC Machine". In: *Journal of Instrumentation* 3.08 (2008), S08001. DOI: 10.1088/1748-0221/3/08/S08001. URL: https://dx.doi.org/10.1088/1748-0221/3/08/S08001 (cit. on p. 1).

[2]The CMS Collaboration. „The CMS experiment at the CERN LHC". In: *Journal of Instrumentation* 3.08 (2008), S08004. DOI: 10.1088/1748-0221/3/08/S08004. URL: https://dx.doi.org/10.1088/1748-0221/3/08/S08004 (cit. on pp. 1, 4).

[3]*Public CMS Luminosity Information*. https://twiki.cern.ch/twiki/bin/view/CMSPublic/LumiPublicResults (cit. on p. 2).

[4]The ATLAS Collaboration. „Observation of a new particle in the search for the Standard Model Higgs boson with the ATLAS detector at the LHC". In: *Physics Letters B* 716.1 (2012), pp. 1–29. DOI: https://doi.org/10.1016/j.physletb.2012.08.020. URL: https://www.sciencedirect.com/science/article/pii/S037026931200857X (cit. on p. 1).

[5]The CMS Collaboration. „Observation of a new boson at a mass of 125 GeV with the CMS experiment at the LHC". In: *Physics Letters B* 716.1 (2012), pp. 30–61. DOI: https://doi.org/10.1016/j.physletb.2012.08.021. URL: https://www.sciencedirect.com/science/article/pii/S0370269312008581 (cit. on p. 1).

[6]Vardan Khachatryan et al. „Observation of the rare $B_s^0 \to \mu^+\mu^-$ decay from the combined analysis of CMS and LHCb data". In: *Nature* 522 (2015), pp. 68–72. DOI: 10.1038/nature14474. arXiv: 1411.4413 [hep-ex] (cit. on p. 2).

[7]Morad Aaboud et al. „Study of the rare decays of B_s^0 and B^0 into muon pairs from data collected during the LHC Run 1 with the ATLAS detector". In: *Eur. Phys. J. C* 76.9 (2016), p. 513. DOI: 10.1140/epjc/s10052-016-4338-8. arXiv: 1604.04263 [hep-ex] (cit. on p. 2).

[8]G Apollinari, I Béjar Alonso, O Brüning, M Lamont, and L Rossi. *High-Luminosity Large Hadron Collider (HL-LHC): Preliminary Design Report*. CERN Yellow Reports: Monographs. Geneva: CERN, 2015. DOI: 10.5170/CERN-2015-005. URL: http://cds.cern.ch/record/2116337 (cit. on p. 2).

[9]*Long Term LHC Schedule*. http://lhc-commissioning.web.cern.ch/schedule/LHC-long-term.htm (cit. on p. 3).

[10]D Contardo, M Klute, J Mans, L Silvestris, and J Butler. *Technical Proposal for the Phase-II Upgrade of the CMS Detector*. Tech. rep. Geneva, 2015. DOI: 10.17181/CERN.VU8I.D59J. URL: https://cds.cern.ch/record/2020886 (cit. on pp. 3, 8).

[11] „Updates on Performance of Physics Objects with the Upgraded CMS detector for High Luminosity LHC." In: (2016). URL: https://cds.cern.ch/record/2222084 (cit. on p. 3).

[12] „Updates on Projections of Physics Reach with the Upgraded CMS Detector for High Luminosity LHC". In: (2016). URL: https://cds.cern.ch/record/2221747 (cit. on p. 3).

[13] Armen Tumasyan et al. „Evidence for WW/WZ vector boson scattering in the decay channel $\ell\nu$qq produced in association with two jets in proton-proton collisions at s=13 TeV". In: *Phys. Lett. B* 834 (2022), p. 137438. DOI: 10.1016/j.physletb.2022.137438. arXiv: 2112.05259 [hep-ex] (cit. on p. 3).

[14] V. Halyo, A. Hunt, P. Jindal, P. LeGresley, and P. Lujan. „GPU Enhancement of the Trigger to Extend Physics Reach at the LHC". In: *JINST* 8 (2013), P10005. DOI: 10.1088/1748-0221/8/10/P10005. arXiv: 1305.4855 [physics.ins-det] (cit. on p. 4).

[15] W. Adam, T. Bergauer, D. Blöch, et al. „The CMS Phase-1 Pixel Detector Upgrade". In: *JINST* 16.02 (2021), P02027. DOI: 10.1088/1748-0221/16/02/P02027. arXiv: 2012.14304. URL: https://cds.cern.ch/record/2748381 (cit. on pp. 4, 8).

[16] A Colaleo, A Safonov, A Sharma, and M Tytgat. *CMS Technical Design Report for the Muon Endcap GEM Upgrade*. Tech. rep. 2015. URL: https://cds.cern.ch/record/2021453 (cit. on p. 4).

[17] CMS Collaboration. *The Phase-2 Upgrade of the CMS Barrel Calorimeters*. Tech. rep. This is the final version, approved by the LHCC. Geneva: CERN, 2017. URL: https://cds.cern.ch/record/2283187 (cit. on p. 5).

[18] *The Phase-2 Upgrade of the CMS Endcap Calorimeter*. Tech. rep. Geneva: CERN, 2017. DOI: 10.17181/CERN.IV8M.1JY2. URL: https://cds.cern.ch/record/2293646 (cit. on p. 5).

[19] Collaboration CMS. *A MIP Timing Detector for the CMS Phase-2 Upgrade*. Tech. rep. Geneva: CERN, 2019. URL: https://cds.cern.ch/record/2667167 (cit. on p. 5).

[20] Tai Sakuma. „Cutaway diagrams of CMS detector". In: (2019). URL: http://cds.cern.ch/record/2665537 (cit. on p. 6).

[21] *The Phase-2 Upgrade of the CMS Tracker*. Tech. rep. Geneva: CERN, 2017. DOI: 10.17181/CERN.QZ28.FLHW. URL: https://cds.cern.ch/record/2272264 (cit. on pp. 7, 10, 11, 14, 21, 22).

[22] L L Jones, M J French, Q R Morrissey, et al. „The APV25 deep submicron readout chip for CMS detectors". In: (1999). DOI: 10.5170/CERN-1999-009.162. URL: https://cds.cern.ch/record/432224 (cit. on p. 8).

[23] J Butler, D Contardo, M Klute, et al. *CMS Phase II Upgrade Scope Document*. Tech. rep. Geneva: CERN, 2015. URL: https://cds.cern.ch/record/2055167 (cit. on p. 8).

[24] A Ferrari, Paola R Sala, A Fassò, and Johannes Ranft. *FLUKA: A multi-particle transport code (program version 2005)*. CERN Yellow Reports: Monographs. Geneva: CERN, 2005. DOI: 10.5170/CERN-2005-010. URL: https://cds.cern.ch/record/898301 (cit. on p. 9).

[25] T.T. Böhlen, F. Cerutti, M.P.W. Chin, et al. „The FLUKA Code: Developments and Challenges for High Energy and Medical Applications“. In: *Nuclear Data Sheets* 120 (2014), pp. 211–214. DOI: https://doi.org/10.1016/j.nds.2014.07.049. URL: https://www.sciencedirect.com/science/article/pii/S0090375214005018 (cit. on p. 9).

[26] J (CERN) Chistiansen and M (LBNL) Garcia-Sciveres. *RD Collaboration Proposal: Development of pixel readout integrated circuits for extreme rate and radiation*. Tech. rep. Geneva: CERN, 2013. URL: https://cds.cern.ch/record/1553467 (cit. on pp. 12, 14).

[27] Giacomo Sguazzoni. *The CMS Pixel Detector for the High Luminosity LHC*. Tech. rep. Geneva: CERN, 2022. URL: https://cds.cern.ch/record/2846683 (cit. on p. 13).

[28] Hendrik Jansen et al. „Performance of the EUDET-type beam telescopes“. In: *EPJ Tech. Instrum.* 3.1 (2016), p. 7. DOI: 10.1140/epjti/s40485-016-0033-2. arXiv: 1603.09669 [physics.ins-det] (cit. on p. 15).

[29] Rudy Ceccarelli. „Results on 3D Pixel Sensors for the CMS Upgrade at the HL-LHC“. In: *PoS* Pixel2022 (2023), p. 046. DOI: 10.22323/1.420.0046 (cit. on p. 15).

[30] Massimiliano Antonello. „Results of Planar Pixel Sensors Qualification Campaign for the CMS Phase 2 Upgrade“. In: *2022 IEEE Nuclear Science Symposium (NSS), Medical Imaging Conference (MIC) and Room Temperature Semiconductor Detector (RTSD) Conference*. Nov. 2022. DOI: 10.1109/NSS/MIC44845.2022.10399205 (cit. on p. 15).

[31] Paulo Moreira, Sophie Baron, Stefan Biereigel, et al. *lpGBT documentation: release*. 2022. URL: http://cds.cern.ch/record/2809058 (cit. on p. 17).

[32] Jan Troska, Alexander Brandon-Bravo, Stephane Detraz, et al. „The VTRx+, an optical link module for data transmission at HL-LHC“. In: *PoS* TWEPP-17 (2017), p. 048. DOI: 10.22323/1.313.0048. URL: https://cds.cern.ch/record/2312396 (cit. on p. 17).

[33] Sebastien Viret. *CIC2 a radiation tolerant 65nm data aggregation ASIC for the future CMS tracking detector at LHC*. Tech. rep. 05. Geneva: CERN, 2022. DOI: 10.1088/1748-0221/17/05/C05016. URL: http://cds.cern.ch/record/2797676 (cit. on p. 22).

[34] CMS Outer Tracker Upgrade Collaboration. *CBC 3.1 User Manual*. https://edms.cern.ch/document/2355257/1. [Online; internal document]. 2023 (cit. on pp. 23–26).

[35] Alessandro Caratelli, Davide Ceresa, Jan Kaplon, et al. „Short-Strip ASIC (SSA): A 65nm silicon-strip readout ASIC for the Pixel-Strip (PS) module of the CMS Outer Tracker detector upgrade at HL-LHC“. In: *PoS* TWEPP-17 (2018), p. 031. DOI: 10.22323/1.313.0031 (cit. on p. 27).

[36] CMS Outer Tracker Upgrade Collaboration. *MPA2 user manual*. https://edms.cern.ch/document/2732259/0. [Online; internal document]. 2024 (cit. on p. 28).

[37] Christopher Edward Brown. *CMS Level-1 Track Finder for the Phase-2 Upgrade*. Tech. rep. Geneva: CERN, 2023. URL: https://cds.cern.ch/record/2883047 (cit. on p. 31).

[38] PICMG. *AdvancedTCA® Base Specification*. Tech. rep. Accessed: [Insert current date here]. Mar. 2008. URL: https://www.picmg.org/product/advancedtca-base-specification/ (cit. on p. 31).

[39] R. Aggleton, L.E. Ardila-Perez, F.A. Ball, et al. „An FPGA based track finder for the L1 trigger of the CMS experiment at the High Luminosity LHC“. In: *Journal of Instrumentation* 12.12 (2017), P12019. DOI: 10.1088/1748-0221/12/12/P12019. URL: https://dx.doi.org/10.1088/1748-0221/12/12/P12019 (cit. on p. 31).

[40] E. Bartz et al. „FPGA-based tracking for the CMS Level-1 trigger using the tracklet algorithm“. In: *JINST* 15.06 (2020), P06024. DOI: 10.1088/1748-0221/15/06/P06024. arXiv: 1910.09970 [physics.ins-det] (cit. on p. 31).

[41] R. Fruhwirth. „Application of Kalman filtering to track and vertex fitting“. In: *Nucl. Instrum. Meth. A* 262 (1987), pp. 444–450. DOI: 10.1016/0168-9002(87)90887-4 (cit. on p. 32).

[42] *The Phase-2 Upgrade of the CMS Level-1 Trigger*. Tech. rep. Final version. Geneva: CERN, 2020. URL: https://cds.cern.ch/record/2714892 (cit. on p. 32).

[43] David Gabriel Monk. „Research and Development for the Data, Trigger and Control Card in Preparation for Hi-Lumi LHC“. Imperial Coll., London, 2023. URL: http://cds.cern.ch/record/2860209 (cit. on pp. 32, 67–69).

[44] Mark Istvan Kovacs, Georges Blanchot, Tomasz Gadek, et al. *Front-end hybrid designs for the CMS Phase-2 upgrade towards the production phase*. Tech. rep. Geneva: CERN, 2022. DOI: 10.1088/1748-0221/17/04/C04018. URL: https://cds.cern.ch/record/2797690 (cit. on p. 34).

[45] Angelos Zografos, Georges Blanchot, Irene Mateos Dominguez, et al. *Power, Readout and Service Hybrids for the CMS Phase-2 Upgrade*. Tech. rep. 03. Geneva: CERN, 2022. DOI: 10.1088/1748-0221/17/03/C03034. URL: https://cds.cern.ch/record/2797682 (cit. on p. 34).

[46] Konstantinos Damanakis. „Silicon sensors for the Phase-2 upgrade of the CMS Outer Tracker; status and early results from the production phase“. In: *Nucl. Instrum. Meth. A* 1040 (2022), p. 167034. DOI: 10.1016/j.nima.2022.167034 (cit. on p. 34).

[47] Dow. *Sylgard 186 Datasheet*. https://edms.cern.ch/document/2638759 (cit. on p. 39).

[48] *Documentation of the μDTC Project*. https://espace.cern.ch/project-FC7/SitePages/Home.aspx (cit. on p. 55).

[49] M. Pesaresi, M. Barros Marin, G. Hall, et al. „The FC7 AMC for generic DAQ & control applications in CMS“. In: *JINST* 10.03 (2015), p. C03036. DOI: 10.1088/1748-0221/10/03/C03036 (cit. on pp. 55, 56).

[50] V. Bobillier, S. Haas, M. Joos, et al. „MicroTCA and AdvancedTCA equipment evaluation and developments for LHC experiments“. In: *JINST* 11.02 (2016), p. C02022. DOI: 10.1088/1748-0221/11/02/C02022 (cit. on p. 55).

[51] Mykyta Haranko. „Development of a test DAQ system for the CMS Phase-2 outer tracker upgrade“. Presented 09 Jan 2020. Hamburg U., 2019. URL: https://cds.cern.ch/record/2711873 (cit. on p. 56).

[52] Andrew Rose et al. „Serenity: An ATCA prototyping platform for CMS Phase-2“. In: *PoS* TWEPP2018 (2019), p. 115. DOI: 10.22323/1.343.0115 (cit. on p. 60).

[53] *IDTM Lisbon, Presentation from Alessandro Rossi*. https://indico.lip.pt/event/1491/contributions/5086/attachments/4111/6436/CMSTrackerUpgrade_IDTM23_RossiA_v1.pdf (cit. on p. 64).

[54] A. Albert et al. „The Apollo ATCA Platform“. In: *PoS* TWEPP2019 (2020), p. 120. DOI: 10.22323/1.370.0120. arXiv: 1911.06452 [physics.ins-det] (cit. on p. 64).

[55] Samtec. *FireFlyTM Application Design Guide*. Tech. rep. Accessed: [Insert current date here]. May 2021. URL: http://suddendocs.samtec.com/ebrochures/firefly-brochure.pdf (cit. on p. 66).

[56] AMD Xilinx. *UltraScaleTM Architecture and Product Data Sheet: Overview*. Tech. rep. Accessed: [Insert current date here]. Nov. 2022. URL: https://docs.xilinx.com/v/u/en-US/ds890-ultrascale-overview (cit. on p. 66).

[57] Bergamin, Caponetto, Caratelli, and Ceresa et al. https://edms.cern.ch/document/2797497/1. [Online; internal document]. 2021 (cit. on p. 70).

[58] Guido Magazzú and Paolo Prosperi. „The DAQPATH readout system of the Serenity boards for the CMS Phase-II Upgrade“. In: *Nucl. Instrum. Meth. A* 1047 (2023), p. 167803. DOI: 10.1016/j.nima.2022.167803 (cit. on pp. 71, 72).

[59] G Abbiendi. *Letter of Intent: the MUonE project*. Tech. rep. The collaboration has not yet a structure, therefore the names above are for the moment an indication of contacts. Geneva: CERN, 2019. URL: https://cds.cern.ch/record/2677471 (cit. on pp. 73, 80, 81).

[60] D. P. Aguillard et al. „Measurement of the Positive Muon Anomalous Magnetic Moment to 0.20 ppm“. In: *Phys. Rev. Lett.* 131.16 (2023), p. 161802. DOI: 10.1103/PhysRevLett.131.161802. arXiv: 2308.06230 [hep-ex] (cit. on pp. 73, 79).

[61] C. M. Carloni Calame, M. Passera, L. Trentadue, and G. Venanzoni. „A new approach to evaluate the leading hadronic corrections to the muon g-2“. In: *Phys. Lett. B* 746 (2015), pp. 325–329. DOI: 10.1016/j.physletb.2015.05.020. arXiv: 1504.02228 [hep-ph] (cit. on pp. 73, 80).

[62] G. Abbiendi et al. „Measuring the leading hadronic contribution to the muon g-2 via μe scattering“. In: *Eur. Phys. J. C* 77.3 (2017), p. 139. DOI: 10.1140/epjc/s10052-017-4633-z. arXiv: 1609.08987 [hep-ex] (cit. on pp. 73, 80, 82).

[63] P. Kusch and H. M. Foley. „The Magnetic Moment of the Electron“. In: *Phys. Rev.* 74.3 (1948), p. 250. DOI: 10.1103/PhysRev.74.250 (cit. on p. 74).

[64] Julian S. Schwinger. „On Quantum electrodynamics and the magnetic moment of the electron“. In: *Phys. Rev.* 73 (1948), pp. 416–417. DOI: 10.1103/PhysRev.73.416 (cit. on p. 74).

[65] X. Fan, T. G. Myers, B. A. D. Sukra, and G. Gabrielse. „Measurement of the Electron Magnetic Moment“. In: *Phys. Rev. Lett.* 130.7 (2023), p. 071801. DOI: 10.1103/PhysRevLett.130.071801. arXiv: 2209.13084 [physics.atom-ph] (cit. on p. 74).

[66] Richard H. Parker, Chenghui Yu, Weicheng Zhong, Brian Estey, and Holger Müller. „Measurement of the fine-structure constant as a test of the Standard Model“. In: *Science* 360 (2018), p. 191. DOI: 10.1126/science.aap7706. arXiv: 1812.04130 [physics.atom-ph] (cit. on pp. 74, 75).

[67] Léo Morel, Zhibin Yao, Pierre Cladé, and Saïda Guellati-Khélifa. „Determination of the fine-structure constant with an accuracy of 81 parts per trillion“. In: *Nature* 588.7836 (2020), pp. 61–65. DOI: 10.1038/s41586-020-2964-7 (cit. on p. 74).

[68] Fred Jegerlehner. „The Muon g-2 in Progress“. In: *Acta Phys. Polon. B* 49 (2018). Ed. by Marek Jeżabek, p. 1157. DOI: 10.5506/APhysPolB.49.1157. arXiv: 1804.07409 [hep-ph] (cit. on p. 75).

[69] T. Aoyama et al. „The anomalous magnetic moment of the muon in the Standard Model“. In: *Phys. Rept.* 887 (2020), pp. 1–166. DOI: 10.1016/j.physrep.2020.07.006. arXiv: 2006.04822 [hep-ph] (cit. on p. 75).

[70] Tatsumi Aoyama, Masashi Hayakawa, Toichiro Kinoshita, and Makiko Nio. „Complete Tenth-Order QED Contribution to the Muon g-2“. In: *Phys. Rev. Lett.* 109 (2012), p. 111808. DOI: 10.1103/PhysRevLett.109.111808. arXiv: 1205.5370 [hep-ph] (cit. on p. 75).

[71] Friedrich Jegerlehner. *The Anomalous Magnetic Moment of the Muon*. Vol. 274. Cham: Springer, 2017. DOI: 10.1007/978-3-319-63577-4 (cit. on p. 76).

[72] Sz. Borsanyi et al. „Leading hadronic contribution to the muon magnetic moment from lattice QCD“. In: *Nature* 593.7857 (2021), pp. 51–55. DOI: 10.1038/s41586-021-03418-1. arXiv: 2002.12347 [hep-lat] (cit. on p. 77).

[73] G. Colangelo et al. „Prospects for precise predictions of a_μ in the Standard Model“. In: (Mar. 2022). arXiv: 2203.15810 [hep-ph] (cit. on p. 78).

[74] J. Bailey et al. „The Anomalous Magnetic Moment of Positive and Negative Muons“. In: *Phys. Lett. B* 67 (1977), p. 225. DOI: 10.1016/0370-2693(77)90199-X (cit. on p. 79).

[75] Georges Charpak, F. J. M. Farley, R. L. Garwin, et al. „Measurement of the anomalous magnetic moment of the muon“. In: *Phys. Rev. Lett.* 6 (1961). Ed. by N. Cabibbo, pp. 128–132. DOI: 10.1103/PhysRevLett.6.128 (cit. on p. 79).

[76] G. W. Bennett et al. „Final Report of the Muon E821 Anomalous Magnetic Moment Measurement at BNL“. In: *Phys. Rev. D* 73 (2006), p. 072003. DOI: 10.1103/PhysRevD.73.072003. arXiv: hep-ex/0602035 (cit. on p. 79).

[77] B. Abi et al. „Measurement of the Positive Muon Anomalous Magnetic Moment to 0.46 ppm“. In: *Phys. Rev. Lett.* 126.14 (2021), p. 141801. DOI: 10.1103/PhysRevLett.126.141801. arXiv: 2104.03281 [hep-ex] (cit. on p. 79).

[78] Friedrich Jegerlehner. *The anomalous magnetic moment of the muon*. Vol. 226. 2008. DOI: 10.1007/978-3-540-72634-0 (cit. on p. 80).

[79] B. e. Lautrup, A. Peterman, and E. de Rafael. „Recent developments in the comparison between theory and experiments in quantum electrodynamics“. In: *Phys. Rept.* 3 (1972), pp. 193–259. DOI: 10.1016/0370-1573(72)90011-7 (cit. on p. 80).

[80] V. Bunakov and Y. Novikov. „P violation and T violation tests with polarized resonance neutrons“. In: *Phys. Lett. B* 429 (1998), p. 7. DOI: 10.1016/S0370-2693(98)00462-6. arXiv: nucl-th/9811059 (cit. on p. 81).

[81] P. A. Baikov, K. G. Chetyrkin, J. H. Kuhn, and C. Sturm. „The relation between the QED charge renormalized in MSbar and on-shell schemes at four loops, the QED on-shell beta-function at five loops and asymptotic contributions to the muon anomaly at five and six loops“. In: *Nucl. Phys. B* 867 (2013), pp. 182–202. DOI: 10.1016/j.nuclphysb.2012.09.018. arXiv: 1207.2199 [hep-ph] (cit. on p. 81).

[82] Christian Sturm. „Leptonic contributions to the effective electromagnetic coupling at four-loop order in QED“. In: *Nucl. Phys. B* 874 (2013), pp. 698–719. DOI: 10.1016/j.nuclphysb.2013.06.009. arXiv: 1305.0581 [hep-ph] (cit. on p. 81).

[83] P. A. Baikov, A. Maier, and P. Marquard. „The QED vacuum polarization function at four loops and the anomalous magnetic moment at five loops“. In: *Nucl. Phys. B* 877 (2013), pp. 647–661. DOI: 10.1016/j.nuclphysb.2013.10.020. arXiv: 1307.6105 [hep-ph] (cit. on p. 81).

[84] Fedor Ignatov, Riccardo Nunzio Pilato, Thomas Teubner, and Graziano Venanzoni. „An alternative evaluation of the leading-order hadronic contribution to the muon g-2 with MUonE“. In: *Phys. Lett. B* 848 (2024), p. 138344. DOI: 10.1016/j.physletb.2023.138344. arXiv: 2309.14205 [hep-ph] (cit. on p. 81).

[85] Dipanwita Banerjee et al. „M2 Experimental Beamline Optics Studies for Next Generation Muon Beam Experiments at CERN“. In: *JACoW* IPAC2021 (2021), pp. 4041–4044. DOI: 10.18429/JACoW-IPAC2021-THPAB143 (cit. on p. 81).

[86] *HLS4ML*. https://fastmachinelearning.org/hls4ml/ (cit. on p. 84).

[87] Matteo Magherini. „The MUonE DAQ: online track-finding and event selection in hardware at 40 MHz“. In: *JINST* 19.03 (2024), p. C03054. DOI: 10.1088/1748-0221/19/03/C03054 (cit. on pp. 84, 90, 93).

[88] Aram Hayrapetyan et al. „Performance of the CMS electromagnetic calorimeter in pp collisions at $\sqrt{s} = 13$ TeV“. In: (Mar. 2024). arXiv: 2403.15518 [physics.ins-det] (cit. on p. 85).

[89] *CAEN SY 4527*. https://www.caen.it/products/sy4527/ (cit. on p. 88).

[90] *CAEN A7435*. https://www.caen.it/products/a7435/ (cit. on p. 88).

[91] *CAEN A2519*. https://www.caen.it/download/?filter=A2519 (cit. on p. 88).

[92] *Prometheus*. https://prometheus.io/ (cit. on p. 96).

[93] *Grafana*. https://grafana.com/ (cit. on p. 96).

[94] *WebGL*. https://www.khronos.org/api/webgl (cit. on p. 98).

[95] *OpenGL*. https://www.opengl.org/ (cit. on p. 98).

List of Figures

List of Tables

Glossary

μDTC Micro Data, Trigger, and Control. 55, 56, 61, 120, 134

μTCA Micro Telecommunications Computing Architecture. 55, 56, 58, 63

AlCF Aluminium Carbon Fiber. 35, 47, 48, 133

ALICE A Large Ion Collider Experiment. 1

AMC Advanced Mezzanine Card. 55–57, 134

API Application Programming Interface. 88, 93, 98

ASIC Application-Specific Integrated Circuit. 20, 21, 23, 24, 29, 55

ATCA Advanced Telecommunications Computing Architecture. 31, 63, 65, 66, 134

ATLAS A Toroidal LHC ApparatuS. 1, 2, 12

BSM Beyond Standard Model. 3, 74

Bx Bunch Crossing. 23, 64, 67, 68, 93

CBC CMS Binary Chip. 22–25, 30, 53, 59, 60, 71, 132, 134

CERN European Organization for Nuclear Research. 62, 67, 79, 94, 100, 134

CIC Concentrator Integrated Circuit. 22, 27, 29, 30, 62, 63, 68, 70, 71, 94, 132, 135

CMOS Complementary Metal-Oxide Semiconductor. 14, 23

CMS Compact Muon Solenoid. v, viii, 1–4, 6–10, 12, 14, 15, 17, 18, 21–23, 63, 65, 72, 73, 82, 83, 85, 87, 88, 90–94, 96, 98, 100, 102, 104, 106, 108, 110, 112, 114, 116, 119–121, 131, 134

CROC CMS flavour of RD53. 15, 132

DAQ Data Acquisition. v, vi, viii, 55, 60, 63, 65, 67, 71–73, 83, 87, 89–91, 109, 120, 121, 134

DDR3 Double Data Rate 3. 57

DLL Delay Locked Loop. 23, 24

DQM Data Quality Monitoring. 96, 97, 136

DTC Data, Trigger, and Control. 17, 19, 31, 55, 64–72, 120, 132, 134, 135

DTH DAQ and TCDS Hub. 71

DUT Device Under Test. 100, 106, 108

e-link External Link. 68, 69, 71

ECAL Electromagnetic Calorimeter. viii, 5, 82, 85, 88

EMP Extensible, Modular data Processor. 66–68, 135

EWK Electroweak. 3, 75, 76

FCI Fast Control Interface. 23, 24, 26

FE Front End. 15, 29, 30, 64, 71

FEH Front End Hybrid. 47, 53, 98, 120, 133, 134

FF Flip-Flop. 57

FIFO First In First Out. 70, 72, 91, 135

FMC FPGA Mezzanine Card. 57

FPGA Field Programmable Gate Arrays. v, 31, 55, 57, 63, 66, 67, 69–71

FSM Finite State Machine. 71

HCAL Hadronic Calorimeter. 5

HGCAL High Granularity Calorimeter. 5, 119

HIP Highly Ionizing Particle. 25, 27–29

HL-LHC high Luminosity LHC. 1–3, 5, 7, 9, 17, 119, 120

HLT High-Level Trigger. 4, 9, 67, 71, 131

HV High Voltage. 15

IT Inner Tracker. 7–9, 11, 12, 15–18, 55, 58, 119, 131, 132, 134

L1A Level 1 Accept. 71

LHC Large Hadron Collider. v, 1–3, 119, 120, 131

LHCb Large Hadron Collider beauty. 1, 2

lpGbt Low Power Gigabit Transceiver. 17, 22, 30, 63, 67, 71, 88, 96

LS Long Shutdown. 2, 3, 5

LUT Look Up Table. 27, 57

MCH MicroTCA Control Hub. 55

MIP Minimum Ionizing Particle. 5, 27, 29

MPA Macro Pixel ASIC. 22, 27–30, 47, 60, 62, 71, 72, 132, 133

MTD Minimum Ionizing Particle Timing Detector. 5, 119

MUX Multiplexer. 57

OT Outer Tracker. v, 4, 7, 9, 11, 19–21, 31, 55, 57, 58, 64, 73, 83, 88, 119–121, 131, 132, 134

PCB Printed Circuit Board. 66

PID Particle Identification. 85

POH Power Out Hybrid. 47, 133

PU pile-up. 5, 12

QCD Quantum Chromodynamics. 73, 75–77, 80

QED Quantum Electrodynamics. 74–76, 81

ROC Read Out Chip. 14, 15

ROH Read Out Hybrid. 47, 133

SEH Service End Hybrid. 53, 94, 134

SEU Single Event Upset. 14

SFL Stub Finding Logic. 26

shunt-LDO shunt-Low-Dropout. 14, 17

SiPM Silicon PhotoMultiplier. 5

SM Standard Model. 3, 73

SRAM Static RAM. 28, 29

SSA Short Strip ASIC. 22, 27–29, 47, 60–63, 132–134

TB2S Tracker Barrel 2S. 19–21, 132

TBPS Tracker Barrel PS. 19–21, 132

TBPX Tracker Barrel Pixel Detector. 12, 15, 16

TEC Tracker EndCap. 8

TEDD Tracker Endcap Double Discs. 20, 132

TEPX Tracker Endcap Pixel Detector. 12, 16

TFP Track Finding Process. 64–68, 134

TFPX Tracker Forward Pixel Detector. 12, 16

TIB Tracker Inner Barrel. 8

TID Tracker Inner Disk. 8

TOB Tracker Outer Barrel. 8

ToT Time-Over-Threshold. 14